# Coherent Light Transport in Randomly Assembled, Highly Multiple Scattering Media

---

**Dissertation**

**zur**

**Erlangung der naturwissenschaftlichen Doktorwürde (Dr. sc. nat.)**

vorgelegt der

**Mathematisch-naturwissenschaftlichen Fakultät**

der

## Universität Zürich

von

**Lukas Schertel**

aus

Deutschland

**Promotionskomission**

**Prof. Dr. Christof M. Aegerter** (Vorsitz, Leitung der Dissertation)

**Prof. Dr. Georg Maret**

**Prof. Dr. Johan Chang**

**Dr. Geoffroy J. Aubry**

Zürich, 2018

**Abstract**

In this thesis I describe my work on coherent light transport in strongly multiple scattering media. Inspired by the experimental search for light localization in three-dimensional media, a coherent wave phenomenon in multiple scattering, the conceptual and experimental difficulties in the observation of this wave phenomenon are discussed. I show time of flight measurements that question earlier observed deviations from classical (diffusive) light transport. Moreover, I reveal that clear signs of light localization in 3D media have never been achieved experimentally and explain earlier claims in the Konstanz group by an extended diffusion model accounting for a weak fluorescence in the commercial white paint samples. To build optimized self-made samples, a quantitative transport model for resonant light transport in photonic glasses (size and shape controlled "white paints") is developed and tested in simulations and experimentally on low and high index materials. Resonant transport behavior is studied further in high index photonic glasses to gain a complete understanding of light scattering in such "white paints". Additionally, an experimental method in which the magneto-optical Faraday effect is used to influence one contribution to light localization, namely the constructive interference on reciprocal scattering paths, is developed for 3D samples. With this, deviations from diffusion can be tested to come from localization if they are found. Lower dimensional experiments are performed to observe light localization and to test such a method, since localization should inherently exist in these lower dimensions. Therefore, the static transmission and its fluctuations through a stack of Faraday active glass slides is studied and compared to transfer matrix simulations. Experimental data show the competition of signs of localization with a dimensional crossover from a 1D to a quasi 1D geometry.

The results obtained in this thesis lead to a more complete understanding of coherent light transport in highly multiple scattering, densely packed media such as photonic glasses. With this I explain why light localization in 3D has not been observed in the previously used materials. An experimental method using the magneto-optical Faraday effect is established to test potentially localizing signals by their sensitivity to high magnetic fields.

## Deutsche Zusammenfassung

Diese Arbeit beschäftigt sich mit der kohärenten Wellenausbreitung elektromagnetischer Lichtwellen durch ungeordnete, stark streuende, dicht gepackte Medien. In solchen Medien ist ein Phasenübergang von einer diffusiven Wellenausbreitung zur sogenannten Lokalisierung mit steigendem Maße an Unordnung theoretisch vorhergesagt worden. In dem ersten Teil meiner Arbeit beschäftige ich mich mit den experimentellen und den konzeptionellen Schwierigkeiten eines Nachweises des Zustandes der Lokalisierung für Lichtwellen. Es werden Flugzeitmessungen von Photonen durch kommerzielle Titandioxidpulver gezeigt, welche die Dateninterpretation bezüglich (Anderson) Lokalisierung in vorherigen Messungen an denselben Proben infrage stellen. Ich zeige, dass Anderson Lokalisierung von Licht in 3D bisher nicht eindeutig nachgewiesen wurde und erkläre frühere Datensätze durch ein erweitertes Diffusionsmodell, welches schwache Fluoreszenzen in diesen weißen Farbpulvern beachtet. Um die Streuung in solchen Proben zu optimieren und sich somit dem Zustand der Lokalisierung anzunähern, wird im nächsten Teil der Arbeit ein Transportmodell für resonante Wellenausbreitung in photonischen Gläsern (größen- und formkontrollierte weiße Farben) entwickelt. Dieses wird anhand von Simulationen und Experimenten in niedrig- und hochindex photonischen Gläsern getestet, um so die Allgemeingültigkeit des Streumodells zu zeigen. Die Ursache der Anderson Lokalisierung ist stark verknüpft mit der Interferenz von Lichtwellen auf reziproken Pfaden. Im nächsten Teil der Arbeit wird eine experimentelle Methode entwickelt, die mit Hilfe des magneto-optischen Faraday Effektes diese Interferenz beeinflusst und somit genutzt werden kann, um experimentelle Anzeichen für Lokalisierung auf deren Ursprung zu testen. Da Lokalisierung in 3D bisher nicht nachgewiesen werden konnte, werden anschließend Experimente und Simulationen in niedrigeren Dimensionen durchgeführt, in welchen Lokalisierung bei großer Systemgröße stets existieren sollte. Konkreter wird der Wellentransport durch einen Glasplattenstapel aus Faraday aktivem Material experimentell studiert und mit Transfermatrixsimulationen verglichen. Damit wird der Einfluss des Faraday Effektes auf die Lokalisierung studiert.

Mit den in dieser Arbeit gewonnen Erkenntnissen lässt sich das bisherige Fehlen eines Nachweises der Anderson Lokalisierung von Licht in 3D verstehen. Weiterhin wird hier ein ganzheitliches Verständnis von Wellentransport in photonischen Gläsern entwickelt. Zudem konnte ein experimenteller Test zum Nachweis von Lokalisierung mit Hilfe des Faraday Effekts gezeigt werden, welcher bei potenziell lokalisierenden Proben angewendet werden kann.

**Acknowledgements**

First of all I want to thank my referees Prof. Christof Aegerter and Prof. Aristide Dogariu for writing a report on my thesis. This thesis was carried out between the group of Prof. Georg Maret from the University of Konstanz and the group of Prof. Christof Aegerter from the University of Zurich as a part of the doctoral program in physics at the University of Zurich. I want to thank Prof. Christof Aegerter for giving me the opportunity to do my research on the fascinating topic of transport of coherent waves in multiple scattering media. He was always very helpful in plenty discussions and his straightforward way of thinking inspired me in many problem solving situations. Although a lot of my laboratory work was located in Konstanz he was any time available. I want to thank Prof. Dr. Georg Maret for offering me to continue my work on this project in Konstanz after my master studies. His way of leading his group in a very open atmosphere, personal- and job-wise, makes this group unique. Especially I thank him for all the discussions about my experimental results and for helping me out understanding the theory of my research in more depth at any time. His office door was always open. Moreover, I would like to thank my research collaborator Geoffroy Aubry, who has also become a friend during our shared time in Konstanz. I remember (loud) discussions, joint achievements, long evenings and fun conferences that made my daily work life a better one. Without him everything would have been much more complicated! I further thank my collaborators Mirco, Mengdi, Henrik, Oliver, Ilona, and Patricia. Most research can only be realized with the help of others. I also thank my colleagues in the Konstanz group and in the Zurich group. I would like to thank all of them for the warm and kind working atmosphere and the fun times we had during work, the breaks, excursions, the winter hut and unofficial group meetings. I met so many inspiring people that made my life in Konstanz and Zurich unforgettable. Finally, I thank my friends and my girlfriend who made my whole physics studies to a part of my life I do not want to miss. There was and is a life beside physics. Last but not least, I thank my family. I am very thankful to have such a great family that helps me out wherever I go and whatever happens. Enjoying to spent time with you means there is more than just the same genes.

# Contents

# Chapter 1

# Introduction

Transport phenomena are constantly present in daily life. They govern many processes in chemistry, biology, physics and engineering. Wave transport in disordered structures describe very diverse systems, all sharing the same physical principles [1, 2]. Examples are electron transport in a copper wire, leading to its electric resistance [3] or ultrasonic waves [4, 5] in condensed matter, mechanical waves in the earth [6], cold atoms in an optical trap [7], or light in disordered photonic materials [8, 9, 10]. Especially light transport is an omnipresent phenomenon ranging from the milky appearance of clouds to structured colors or whiteness in animals [11]. Moreover, optical transport experiments have reached an unprecedented accuracy thanks to the great technological development of sources (e.g., lasers), detectors (e.g., CCDs) and time resolution. In this thesis the focus is on transport of light waves in randomly assembled, densely packed, highly multiple scattering media. Visible light is an ideal testing tool for wave transport phenomena. Beside its technical relevance of optical experiments, relatively high refractive index scattering media in combination with low absorption such as "white paints" and photonic glasses exist in this frequency range. Moreover photons have the advantage not to show additional particle/particle interactions in the multiple scattering regime that can complicate transport theories unlike for example in electronic systems (which show Coulomb interaction).

The earlier mentioned milky appearance of the clouds is a multiple scattering phenomenon arising from the loss of the information about the initial direction of the light. Neglecting that light is a coherent wave that can interfere, the photon transport can be described as a random walk through the medium. Otherwise new phenomena, such as speckle, coherent backscattering [8, 9], universal conductance fluctuations [12] or Anderson localization [13] may arise from interference. The latter was predicted first by P. W. Anderson in 1958 [14] for electronic systems. He predicted a phase transition in 3D from a diffusive to localized state for waves in a disordered medium [3, 13], in which the scattering

strength plays the role of the control parameter. For electronic systems this transition changes the system from a conducting metal to an insulator. Sixty years later, this transition was observed for various kinds of waves such as ultrasonic waves [15] or particle waves [16, 17]. For light waves, Störzer *et al.* [18] and Sperling *et al.* [19] measured deviations from diffusion in 3D samples made of titanium dioxide ($TiO_2$) powders using a time of flight (ToF) and a transmission profile (TP) method and interpreted them as 3D Anderson localization of light.

In this thesis I will show experimental studies of the long time tail of ToF distributions and the long time behavior of the TP width for very thin samples and different turbidities that question this interpretation. Weak fluorescent signals in these powders explain earlier observations consistent with an extended diffusion model. A conceptual discussion of the reasons of the experimental problems in observing Anderson localization of light in 3D follows. One solution could be to increase the scattering strength to currently unreached high values. This might be achieved by lowering the polydispersity and then tuning the scattering to multiple scattering Mie-resonances in monodisperse random assemblies of spheres (so called photonic glasses).

A more quantitative understanding of light transport in densely packed media is required to optimize such advanced "white paint" materials. An appropriate multiple scattering model needs to include the single particle scattering properties as well as interferences arising from particle position correlations and near field coupling. Combing a well know scattering model [20, 21] and the so called Energy Coherent Potential Approximation for an effective refractive index [22] allows me to predict the scattering in densely packed media. This model is tested experimentally on relatively low index (polystyrene) photonic glasses and compared with simulations and models from literature [23, 24].

In a next step the model is used to predict scattering in high index ($TiO_2$) photonic glasses. Spectral transport measurements in newly synthesized high index glasses are performed and compared to the transport model and spectral measurements of commercial "white paints" to develop a full understanding of resonant light transport in photonic glasses and "white paints".

The constructive interference on reciprocal scattering paths in backscattering direction was shown to be the origin of coherent backscattering by Lenke *et al.* [25]. As the coherent backscattering cone is seen to be a manifestation of weak localization and therefore a precursor of Anderson localization, manipulation of reciprocity might also influence signs of Anderson localization. Since the magneto-optical Faraday effect can manipulate reciprocity, it can be used to manipulate the interference at the origin of the coherent wave transport phenomena. In chapter four the interference nature of Anderson localization

is studied, by implementing a method to manipulate signs of Anderson localization in a magnetic field via the magneto-optical Faraday rotation of light. Therefore, the samples need to fulfill two conditions: firstly, the samples need to show signs of localization. In 3D this is connected to the strong scattering regime in which the wavelength of the light $\lambda$ is in the same order of magnitude as the transport mean free path $\ell^\star$ ($\lambda \approx \ell^\star$). This property might be achieved in high index photonic glasses or other advanced structural materials [11]. Secondly, the samples need to show a high magneto-optical Faraday rotation to be able to destroy the reciprocity of the light paths in the experimentally available magnetic fields.

A good candidate for this is cerium fluoride ($CeF_3$), whose Faraday rotation strength strongly increases with decreasing temperature. This material is characterized in this thesis regarding its Faraday rotation at low temperature ($T < 10$ K) and in high magnetic fields ($B = 18$ T). Finally, the manipulation of reciprocity in reflection and transmission geometry is shown in new experiments on coherent backscattering and speckle correlations in strongly scattering samples containing Faraday active material. A proof of principle experiment shows that the destruction of the signs of Anderson localization in 3D in external magnetic fields might be possible if localized samples are found.

Anderson localization is strongly connected to the probability of a random walker to return to its origin, which is finite in one and two dimensions. Thus, for large enough system sizes Anderson localization always exists in lower dimensions. Since 3D samples bear to show Anderson localization of light yet, lower dimensional samples might act as a good testing tool for the above described method. Using a stack of Faraday active glass slides a quasi one dimensional system is realized to test the manipulation of Anderson localization in high magnetic fields. Static transport measurements, namely the mean transmission over various realizations of disorder, and its fluctuations are measured in dependence of the magnetic field and the system size and compared to transfer matrix simulations. With this the influence of magneto-optical Faraday rotation on light transport as well as the transition from a 1D to a quasi 1D system is studied.

# Chapter 2

# Coherent multiple light scattering

In this chapter I first introduce the theoretical background needed to understand coherent wave transport in multiple scattering media. Based on the underlying single scattering processes, multiple scattering can be seen as a series of such scattering events. The classical wave transport description, which can be described as a diffusion process of the energy density, breaks down as soon as coherent waves lead to interference. New phenomena, such as speckle, but also coherent backscattering and, in certain conditions, Anderson localization, arise. Giving an introduction to these phenomena brings us to the experimental methods used to observe Anderson localization of light in 3D. Earlier experimental data are put in question with new experimental measurements. All data are explained consistently by accounting for weak fluorescent signals in the used samples. A conceptual discussion about experimental problems in observing Anderson localization of light follows and a possible pathways to observe Anderson localization in 3D in future experiments is proposed.

## Contents

## 2.1 Random walk model and diffusion approximation

In order to describe the multiple scattering mechanism of photons in random media, a numerical approach can be used: the random walk model. All microscopic details about the single scattering mechanism, which will be discussed in detail in the next chapter, can be put in the transport mean free path $\ell^\star$. This quantity describes the path length on which the orientational correlation is lost in multiple scattering. The transport mean free path takes the role of the characteristic length scale of the discrete step-length distribution. As we will see later, the inverse of $\ell^\star$ multiplied by the wavelength $\lambda$ holds information about the scattering strength of a sample. It is a measurable quantity that describes the static scattering properties of a multiple scattering sample. One can explain incoherent light transport by a diffusion process of the energy density of the electromagnetic wave to learn about dynamics in light transport. This is published detailed in ref. [26] and summarized in ref. [27, 28].[1]

### 2.1.1 Dynamic and static scattering properties

For simplicity let us describe the propagation of a photon in a multiple scattering sample in one dimension. The propagation starts at $x = 0$ at time $t_0 = 0$. The photon can move one step $\Delta x$ (in positive or in negative direction) during

[1] The presented description of the random walk and the diffusion follows ref. [27] and is taken partly from my master thesis [29].

$\Delta t$. Due to the symmetry of the random movement the mean step is $\langle \Delta x \rangle = 0$, such that the mean position of $N$ such photons stays centered around $x = 0$ with a Gaussian distribution. The spread of the photons is described by the mean squared displacement

$$\langle x^2(t) \rangle = \frac{t}{\Delta t} \Delta x^2 = 2Dt \ , \tag{2.1}$$

where $D = \frac{\Delta x^2}{2\Delta t}$ is the Boltzmann diffusion coefficient, which connects the random walk model to the diffusion theory of the photon energy density. In 3D one adds up the independent mean squared displacements of each spatial direction and ends up with

$$\langle r^2 \rangle = \langle x^2 \rangle + \langle y^2 \rangle + \langle z^2 \rangle = 6Dt \ . \tag{2.2}$$

Assuming energy conservation, the temporal change of the energy density distribution $\rho$ in a volume element equals the spacial change of the energy flux $\mathbf{j}$

$$\partial_t \rho = -\nabla \mathbf{j} \ . \tag{2.3}$$

This is the equation of continuity. Introducing Fick's law for the energy flux $\mathbf{j} = -D\nabla\rho$ equation (2.3) can be rewritten to

$$\partial_t \rho = D\nabla^2 \rho \ . \tag{2.4}$$

Absorption, as present in experiments, lowers the temporal change of the energy density. It can be inserted via the term $1/\tau_a \rho$, that is related to an exponential decay in energy density $\rho$ with a time constant $\tau_a$. Thus, equation (2.4) becomes

$$\partial_t \rho = D\nabla^2 \rho - \frac{1}{\tau_a} \rho \ . \tag{2.5}$$

Here $\tau_a$ is the absorption time corresponding to the microscopic absorption length $l_a = c\tau_a / n_{\text{eff}}$, with $c$ the speed of light and $n_{\text{eff}}$ the effective refractive index of the multiple scattering sample. $l_a$ is the path length on which the intensity is attenuated by $1/e$. The macroscopic absorption length is defined as $L_a = \sqrt{D\tau_a}$. The different length scales are illustrated in fig. 2.1.

Solving the diffusion approximation (eq. (2.5)) in 1D starting with a delta peak shaped energy density at $t_0 = 0$ in an infinite medium, leads to a Gaussian

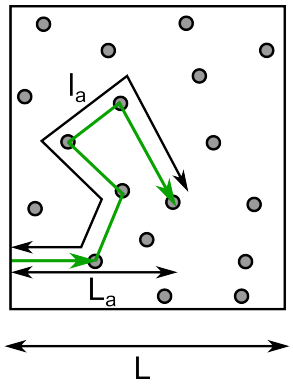


**Figure 2.1:** The microscopic absorption length $\ell_a$ and the macroscopic absorption length $L_a$ in multiple scattering are illustrated. $L$ is the sample size.

distribution of the energy density at position $x$ and time $t$ [28]:

$$\rho(x,t) = \frac{1}{\sqrt{4\pi Dt}} \exp\left(-\frac{x^2}{4Dt} - \frac{t}{\tau_a}\right) . \tag{2.6}$$

The variance $\langle x^2 \rangle$ of this distribution recovers the mean squared displacement of the random walk model:

$$\langle x^2 \rangle = \int x^2 \rho(x,t) dx = 2Dt . \tag{2.7}$$

As mentioned above in the random walk model, the transport mean free path $\ell^\star$ takes the role of the characteristic length scale of the path-length distribution. The exponential path-length distribution $p(\Delta x) = \frac{1}{2\ell^\star} \exp(-\frac{|\Delta x|}{\ell^\star})$, that is the solution of the differential equation for the photon scattering probability, recovers the mean step length $\langle |\Delta x| \rangle = \ell^\star$ and shows a variance of $\langle \Delta x^2 \rangle = 2(\ell^\star)^2$. It leads to a mean squared displacement of

$$\langle x^2 \rangle = \frac{2s\ell^\star}{d} , \tag{2.8}$$

with $s = m\ell^\star$ a photon path of $m$ steps and $d$ the dimension of the system. Combining eq. (2.7) and eq. (2.8) and using the energy transport velocity $v_E = \frac{s}{t}$ of the propagating electromagnetic wave gives a relation between the

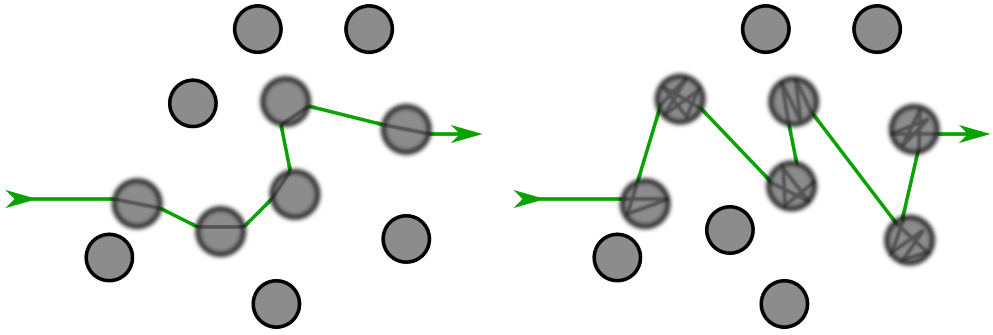


**Figure 2.2:** Sketch of a random walk through a multiple scattering sample (a) without and (b) with resonant scattering inside the scatterers. Resonant scattering can strongly increase the times photons travel in a sample and change the mean free path significantly.

diffusion coefficient D and the transport mean free path $\ell^\star$:

$$D = \frac{v_E \ell^\star}{d} \ . \tag{2.9}$$

Equation (2.9) shows the differences between the main measurable quantities $D$ and $\ell^\star$ to characterize the transport of light in multiple scattering media. While $\ell^\star$ is a pure static property, $D$ carries information about time scales of the scattering in the sample via the energy transport velocity $v_E$. It is not trivial how resonant scattering (see fig. 2.2) acts on the mean free path and the energy velocity. Both quantities can significantly be lowered by resonant scattering. Thus, only a parallel measure of $\ell^\star$ and $D$ gives insides about the dynamic scattering behavior.

In time of flight experiments, as performed in this thesis, the measured property is the time-resolved intensity $I(t)$. This property is connected via Fick's law to the photon density $\rho$ as follows:

$$I(t) = -D\frac{\partial \rho}{\partial z} \ , \tag{2.10}$$

with $z$ along the propagation direction of the incoming light. Equation (2.6) is the solution of the diffusion approximation for a spread of a delta peak in an infinite medium. Experimentally the geometry of the multiple scattering samples used for transmission experiments are slabs with a much larger (approxima-

tely infinite) size in $x$ and $y$ direction (vertical to the propagation direction of the incoming light) than in $z$ direction. This slab geometry with the photons entering the sample from one side can be solved analytically. Therefore, M. Störzer [27] calculated the probability for a photon to travel from a point A to a point B in a slab with boundaries using an image point method, as described by Lenke *et al.* [26]:

$$\rho(z_A, z_B, t) = \frac{2}{L} \exp(-\frac{t}{\tau_a}) \sum_{n=1}^{\infty} \exp\left(-\frac{n^2\pi^2}{L^2} Dt\right) \sin\left(\frac{n\pi}{L} z_A\right) \sin\left(\frac{n\pi}{L} z_B\right) \ . \tag{2.11}$$

Now the transmitted intensity of a point source through a slab of thickness $L$ can be found with eq. (2.10):

$$I(t) = -2D \exp\left(-\frac{t}{\tau_\mathrm{a}}\right) \sum_{n=1}^{\infty} (-1)^n \exp\left(-\frac{n^2\pi^2 D}{L^2} t\right) \frac{\ell^\star}{L} \left(\frac{n\pi}{L}\right)^2 \ . \tag{2.12}$$

This transmission formula is illustrated in fig. 2.3. The long time tail is governed by

$$I(t) \propto \exp\left[-\left(\frac{1}{\tau_\mathrm{a}} + \frac{\pi^2 D}{L^2}\right) t\right] \ . \tag{2.13}$$

Fitting eq. (2.12) to time of flight measurements as discussed in the experimental section allows to extract the absorption time $\tau_\mathrm{a}$ and the diffusion constant $D$ of a specific sample.

Moreover, the path-length distribution function $P(s)$ of a slab of length $L$, with $s$ a specific path, can be calculated from eq. (2.11) using $D = v_E \ell^\star/3$, $t = s/v_\mathrm{E}$ and $\tau_\mathrm{a} = L_\mathrm{a}^2/D$:

$$P(s, L) = \frac{2}{L} \exp\left[-\frac{s\ell^\star}{3L_\mathrm{a}^2}\right] \sum_{n=1}^{\infty} \exp\left[-\frac{n^2\pi^2 s\ell^\star}{3L^2}\right] \sin\left[\frac{n\pi\tilde{\gamma}\ell^\star}{L}\right] \sin\left[\frac{n\pi(L - \tilde{\gamma}\ell^\star)}{L}\right] \ . \tag{2.14}$$

Here $L_\mathrm{a}$ acts as an exponential cut of length for long photon paths. The factor $\tilde{\gamma} = 1 + \gamma$ arises from the boundary conditions, which state that the diffusion starts after distance $z_1 = \tilde{\gamma}\ell^\star$ to the surface inside the sample and ends at $z_2 = L - \tilde{\gamma}\ell^\star$. Here $\gamma \approx 2/3$ [30] is the Milne parameter, which gives information about up to which distance from the boundary the diffusion approximation does not hold. Note that the exact value is not so relevant in transmission since

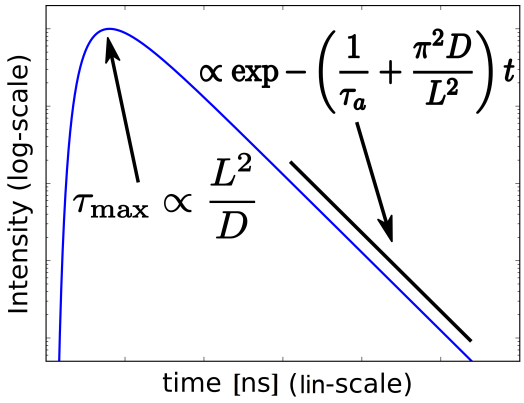


**Figure 2.3:** Transmitted intensity $I(t)$ of a multiple scattering sample in slab geometry calculated from eq. (2.12).

$\tilde{\gamma}\ell^\star$ is small compared to the mean path length $\langle s \rangle$. Equation (2.14) can be used to calculate the field-field-correlation function for transmission speckle, which will be discussed in sec. 4.3.1 about correlation functions.

## 2.2 Coherent wave transport

Coherence is a key concept in the field of wave transport in random media, such as sound wave propagation [31, 4] or matter wave scattering [7, 32]. As seen in the latter section, one can describe the propagation of waves in multiple scattering media as a diffusion process. This holds as long as the coherent contribution of the wave is neglected, but fails to explain phenomena ranging from the celebrated Aharonov-Bohm effect for matter waves to ordinary speckle patterns of light waves (see for example [1]) where interferences play a major role.

### 2.2.1 The speckle pattern

For light the coherent part becomes important when the coherence length $l_c$ is longer than the difference in path lengths of the photons traveling through a multiple scattering sample. When coherent light waves are leaving a multiple scattering sample this leads to angular dependent fluctuations of the transmitted/reflected intensity, arising from the constructive and destructive interference of the waves. This granular pattern is called speckle pattern. In the case of an uncorrelated multiple scattering random walk process speckle

show an exponential intensity distribution. Changing the scatterer positions by moving scatterers (e.g., in a solution), changes the relative phase of the photons and thus changes the observed speckle pattern. Beside a movement of the scatterers, the magneto-optical Faraday rotation can cause such a phase change. Later in this thesis transmission speckle will be used to study the phase change on photon paths in magneto-optical media.

### 2.2.2 Coherent backscattering

Averaging over an ensemble of speckle patterns leads to a mean intensity. But even when the speckles are smeared out an intensity enhancement in backscattering direction, the so called coherent backscattering cone, can be observed. This effect has its origin in the interference of photons traveling on the same path but in opposite direction. Photons from the same incident plane wave propagating on such time reversed paths collect the same phase on their way through the sample (see fig. 2.4(a)). These photon pairs form a specific angular dependent oscillating interference pattern with constructive interference in exact backscattering direction, similar to the interference pattern of a double slit experiment. For a plane wave illuminating the sample surface, there are different possible time reversed pairs of paths, which differ in their distance vector $\mathbf{r}$ parallel to the sample surface. Each interference intensity is then given by $1 + \cos(\mathbf{qr})$, with $\mathbf{q} = \mathbf{k}|\sin(\theta)|$ (see dashed lines in fig. 2.4(b)). Averaging over all these fringe spacings and weighting them with their occurrence probability leads to the so called coherent backscattering cone (CBC, see red line in fig. 2.4(b)). Since all patterns interfere constructively in exact backscattering direction, this leads to a two-fold enhancement in backscattering decaying with an angular scale of $1/(k\ell^\star)$ for an incoming spatially and temporally infinitely extended plane wave [33]. At larger angles, the minima and maxima of the different patterns superimpose and average to a background of unity.

The dependency of the cone width on the transport mean free path $\ell^\star$ can be used in experiments to measure $\ell^\star$. The exact theory (in the diffusion approximation) of coherent backscattering is described in ref. [1, 26, 34]. One can calculate the photon density in the backscattering geometry $\rho_{back}$ for a semi-infinite medium, as done for transmission in eq. (2.11) (see e.g. ref. [35]). Assuming a non-absorbing, multiple scattering sample and a plane, uniform wave impinging perpendicular to the sample surface and having an infinite spatial and temporal coherence, the coherent part $\alpha_\mathrm{c}$ and the incoherent part $\alpha_\mathrm{d}$ of the photon flux backscattered from the sample can be evaluated. The

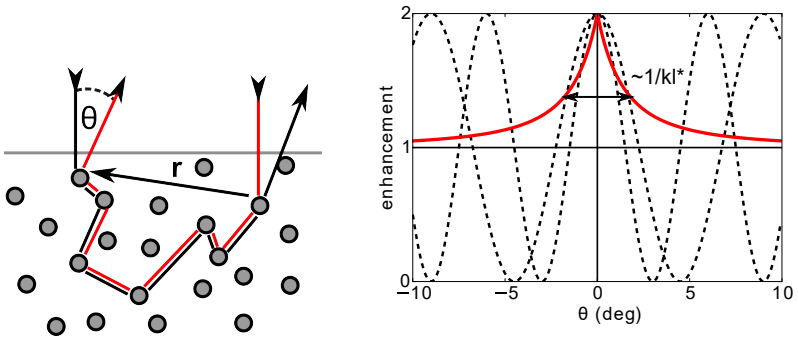


(a) CBC scheme (b) CBC theory

**Figure 2.4:** (a) Scheme of time reversed paths: The photon traveling on the black and the red paths collect the same phase, such that they interfere constructively in exact backscattering geometry. (b) Schematic of the self-averaging process over all interference patterns from different time reversed paths. The black dashed curves show the angular dependent oscillations of the interference pattern for two paths with different distance vectors **r**. The red curve is the so called Coherent Backscattering Cone (CBC) originated from the average over all possible paths with an enhancement of two in the backscattering direction.

incoherent part is called the *Diffuson* and can be written as follows [36, 1]:

$$\alpha_{\mathrm{d}}(\theta) = \frac{3}{4\pi}\mu\left(\frac{z_0}{\ell^\star} + \frac{\mu}{\mu+1}\right) \ , \tag{2.15}$$

with $\mu = \cos(\theta)$ and $z_0$ the average penetration depth of the photon density, that is assumed to be $z_0 = \gamma\ell^\star \approx \frac{2}{3}\ell^\star$ [1]. The coherent part is called the *Cooperon* and states:

$$\alpha_{\mathrm{c}}(\theta) = \frac{3}{8\pi}\frac{\frac{1-\exp(-2qz_0)}{q\ell^\star} + \frac{2\mu}{\mu+1}}{\left(q\ell^\star + \frac{\mu+1}{2\mu}\right)^2} \ , \tag{2.16}$$

where $q = k|\sin(\theta)|$. In this expression the cone tip (around $\theta = 0$) has a triangular shape. These small angles correspond to long scattering paths. These paths can be cut off in experiments by absorption or by a limited coherence length. This leads to a rounding of the cone tip. To account for absorption, the wave vector $q$ can be substituted by $q \to q_{\mathrm{a}} = \sqrt{q^2 + (D\tau_{\mathrm{a}})^{-1}}$ with $\tau_{\mathrm{a}}$ the absorption time. For samples with high refractive index, a large fraction of the light going to leave the sample is reflected back into the sample because

of the large refractive index difference. This artificially extends the diffusive paths and narrows the cone. The correction of the cone shape for internal reflections was calculated by Zhu *et al.* [37] and can be taken into account in the penetration length:

$$z_0 = \gamma \left( \frac{1+R}{1-R} \right) \ell^\star \ , \tag{2.17}$$

with $R$ the reflectivity of the sample. In the calculation of the reflectivity as shown in ref. [37] a fixed value for the refractive index of the sample needs to be given. For the samples used in this thesis the Maxwell Garnett effective refractive index as explained in sec. 3.2.2 was used if not stated differently.

The energy enhancement of the coherent backscattering cone seems to violate energy conservation. Fiebig *et al.* [38] calculated a correction term $\alpha_\mathrm{e}$ to preserve it. They validated their model on experimental data. The angular integral over the corrected cone needs to vanish to account for it:

$$\int_0^{\pi/2} (\alpha_\mathrm{c} + \alpha_\mathrm{e}) \sin(\theta) d\theta \equiv 0 \tag{2.18}$$

This leads to an approximate correction term of [38]:

$$\alpha_\mathrm{e} = -\frac{a}{(k\ell^\star)^2} \frac{\mu}{\mu+1} \ . \tag{2.19}$$

As can be seen from the scaling with $k\ell^\star$ this term becomes relevant for strongly scattering samples. The normalization parameter can be calculated with [36]:

$$a = \frac{\int_0^{\pi/2} \alpha_\mathrm{c} \sin(\theta) d\theta}{\int_0^{\pi/2} \frac{1}{(k\ell^\star)^2} \frac{\mu}{\mu+1} \sin(\theta) d\theta} \ . \tag{2.20}$$

Reference [38] gives an approximated value of $a = 1.15$ for the correction term. Equation (2.16) together with eq. (2.19) can then be used in the experiments to measure the transport mean free path $\ell^\star$ by fitting the coherent backscattering data, using the absorption and the diffusion constant of the sample as obtained by ToF measurements as well as accounting for internal reflections (eq. (2.17).

The coherent backscattering effect was the first evidence for the interference of light waves on time reversed paths in multiple scattering samples [8, 9] and is a manifestation of weak localization. It is therefore often seen as a precursor of Anderson localization or strong localization, described in the next section.

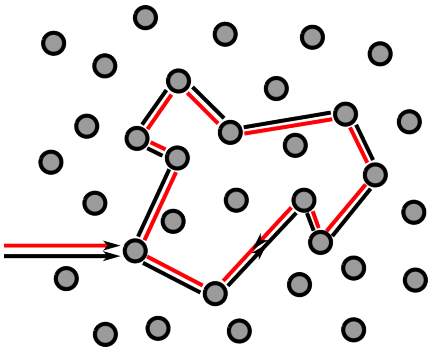

**Figure 2.5:** Schematic of the reciprocal paths in a multiple scattering sample as a simplified picture of the mechanism behind (Anderson) localization. The photon traveling on the black and the red path collect the same phase, such that they interfere constructively in exact backscattering direction.

### 2.2.3 Anderson localization

Anderson localization describes a wave transport phenomenon in a random scattering potential. One contribution to Anderson localization comes from the constructive interference on reciprocal paths, as already introduced in the latter section for waves at a boundary of the sample. These interferences can lead to a halt of diffusion in a bulk when the disorder is strong enough. Historically it was first predicted by P.W. Anderson in 1958 for electronic systems [14]. For electrons this is connected to a disorder induced metal insulator transition [39], scaling with the disorder as the control parameter. As an interference phenomenon, Anderson localization can be generalized for all kind of waves [40] such as matter waves [16, 17, 41, 42], ultrasonic waves [15] or electromagnetic waves [13].

Here I start with a very simplified picture to describe the contribution of interferences on transport behavior[2]. Figure 2.5 shows a random scattering path and the same path traveled in the opposite direction in the bulk of a sample. The constructive interference of these reversed paths leads to an enhanced backscattering probability, known as weak localization. This enhanced return probability can slow down transport if every scatterer is seen as a starting point of time reversed scattering paths (widely studied in the so called *self-consistent theory*).

Increasing the scatterers density (and accordingly the scattering strength) increases the return probability. This and more complex interference contribu-

[2]For a detailed summary of the theories behind Anderson localization see for example ref. [2].

tions can lead to a halt of diffusion. The transition from a diffusive to a localized state, also called the mobility edge, scales with the scattering strength $1/k\ell^\star$ and was predicted by Ioffe and Regel for electronic systems [43]. Their criterion is believed to be also valid for light and predicts the transition to take place at $k\ell^\star \approx 1$. This criterion implies that a wave is scattered several times within one wavelength which shows that the mentioned picture is a rough simplification of the real transport process since the concept of wave propagation breaks down in this limit.

As mentioned in ref. [2], rather than thinking of propagating extended plane waves one should think of standing waves confined in space with long lifetimes in the localized regime.

### The dimension of the system

The above-mentioned phase transition only exists for three (or higher) dimensional systems. This can be understood in terms of the return probability of a random walker as stated in Pólya's random walk theorem [44]. This mathematical treatment of a random walker on an integer lattice concludes that for infinite system the return probability $p(d)$ of dimension $d$ is unity for one or two dimensional systems ($p(1) = p(2) = 1$). For three dimensional systems Pólya showed that the return probability is smaller than one and more precisely $p(3) \approx 0.34$ [45]. This means for large enough systems, there is always a finite probability for the photons to return to their origin in 1D and 2D. Diffusion may come to a halt because of interference, so these systems are always localized for $L \to \infty$ even for low disorder with $k\ell^\star \gg 1$. More precisely the role of the dimension of the system is theoretically described in the *scaling theory* of localization [46, 3].

Finite system size can influence transport in all dimensions, even in 3D systems with high enough disorder to show localization. The microscopic localization length $\ell_{\mathrm{loc}}$ describes the mean path length of localized modes. With this quantity one can define a macroscopic localization length

$$\xi = \sqrt{\frac{\ell^\star \ell_{\mathrm{loc}}}{3}} \tag{2.21}$$

that is associated with the mean spatial extend of the localized modes in the sample. When the sample size is in the order of that length scale $L \approx \xi$ localized modes leak out of the sample and may become diffusive.

### Time dependent diffusion

The concept of slowed down diffusion in the localized regime already introduced in the latter section is recovered in the so called *self-consistent theory*. By including interference effects in the diffusion ansatz Vollhardt and Wölfe developed a diffusion theory for 2D infinite media [47, 48] that predicts a position and time dependent diffusion coefficient. Van Tiggelen *et al.* [49] generalized this theory for finite size systems. For infinite size a renormalized diffusion coefficient is found

$$D = D_0 \left(1 - \frac{1}{(k\ell^\star)^2}\right) \ , \tag{2.22}$$

which recovers the Ioffe-Regel criterion and shows a scaling of the coherent part of the wave with $1/(kl^*)^2$. $D_0$ is the diffusion constant of the normal diffusion approximation. Later Skipetrov and van Tiggelen [50] expanded this theory to 3D systems in slab geometry. They allow a position dependent diffusion coefficient to account for boundaries of the sample where the localized modes leak out of the system. In their paper they show analytically a time dependency of the diffusion coefficient in the localized regime

$$D(t) \propto \frac{1}{t} \ . \tag{2.23}$$

The halt of the diffusion in the localized regime is recovered in this time dependency of the diffusion coefficient:

$$\langle r^2 \rangle = D(t)t = \text{const.} \tag{2.24}$$

A time dependency of the diffusion coefficient was already noticed by Berkovits and Kaveh [51]. They calculated the time dependent transmitted intensity $I(t)$ of a delta peak shaped pulse through a slab of a multiple scattering sample in the localizing regime using the rescaled diffusion coefficient $D(t)$ as done in sec. 2.1.1 for the diffusive regime (see eq. (2.12)):

$$I(t) = -2\frac{l^*}{L}\left(\frac{n\pi}{L}\right)^2 \exp\left(-\frac{t}{\tau_a}\right) \sum_{n=1}^{\infty} (-1)^{n+1} \left(\frac{D(t)}{D_0}\right)^2 \exp\left(-\frac{n^2\pi^2 D(t)}{L^2}t\right) \ . \tag{2.25}$$

From this we already note that the time resolved transmitted intensity is a measurable quantity to look for signs of localization in experiments.

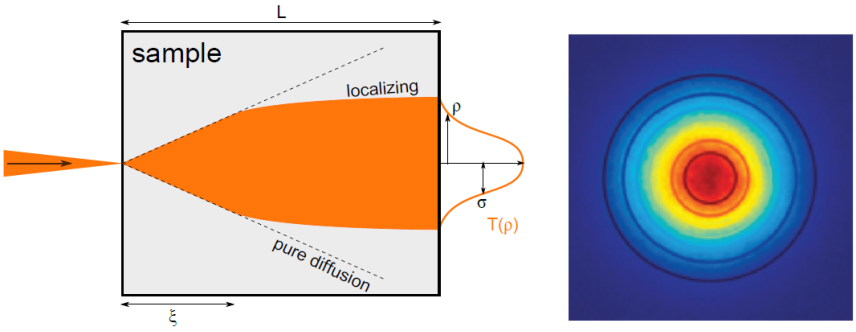


(a) (b)

**Figure 2.6:** Sketch of the transmission profile measurement method: (a) In case of localization the photon cloud (orange) is confined while it expands linear with the sample size $L$ (see dashed lines) in case of diffusion. $\xi$ is the localization length. Figure taken from ref. [28]. (b) A raw image of a measured transmission profile of R104 ($L \approx 1$ mm) 4 ns after the initial laser pulse is shown. The contour plot shows the corresponding fit. Figure taken from ref.[19].

### Time and spatial resolved transmission

Measuring the time resolved transmission through a multiple scattering sample gives insights into the multiple scattering processes. Properties such as the diffusion constant $D$ and the absorption time $\tau_a$ of the samples can be accessed as described in sec. 2.1.1 and by comparing the photon flight times to the diffusive behavior, one can search for signs of localization.

The long time tail of time of flight measurements is still strongly influenced by the absorption of a material. Moreover, to my knowledge there is no widely accepted and experimental verified *analytic* description of the time dependent diffusion in the localized regime. Cherorret *et al.* [52] suggested to measure the time and spatially resolved transmission (the so called transmission profile, TP) through multiple scattering slabs. They use the self consistent theory to calculate the width $\sigma$ of the spread of the photon cloud through a slab shaped multiple scattering sample when illuminated with a pulsed, focused beam on one side and imaged on the opposite side in the diffusive and the localizing regime (see fig. 2.6(a)).

In the diffusive case the width grows linear in space ($\sigma^2_{\text{diff}} \approx 2L^2/3$) and the the mean squared width grow linear in time [53]:

$$\sigma^2_{\text{diff}}(t) = \frac{\int \rho T(\rho,t) d^2\rho}{\int T(\rho,t) d^2} = 4D_0 \left[1 - \frac{1}{(k\ell^\star)^2}\right] t \ , \tag{2.26}$$

where $T(\rho, t)$ is the time and space dependent transmission. In this equation the absorption cancels out as it appears in the denominator and in the numerator as an exponential term $\exp(-t/\tau_a)$. This independence of absorption is an advantage above earlier developed measurement tools. Nevertheless, the measured transmission is still lowered by absorption.

In the localized regime $\ell^\star \ll \xi \ll L$ the mean squared width is predicted to be time-independent in the long time limit when the photon cloud expanded on scales larger than the localization length [53]:

$$\sigma^2_{\text{loc}} = 2\xi L = \text{const.} \tag{2.27}$$

## 2.3 Experimental setups and samples

In this section I first introduce the experimental setups to measure the time (and space) resolved transmission in a multiple scattering sample, namely the time of flight (ToF) and the transmission profile (TP). Moreover, I present one of our coherent backscattering cone (CBC) setups, which is used to characterize the scattering strength of the multiple scattering samples.

As the *Ioffe-Regel* criterium states, Anderson localization of light in a 3D sample can only be reached in strongly scattering materials. The scattering cross section strongly increases with the refractive index contrast between the scatterer and the surrounding medium. Thus, the materials used to observe light localization should have a high refractive index. Another requirement for light localization experiments is that the photons should be able to travel long times in the sample. Otherwise they will get absorbed before they can be observed experimentally. The absorption length acts as a cutoff length for long scattering paths. Therefore, the used materials should also have a low absorption in the preferred wavelength range. In the second part of this section, I will describe materials that fulfill these properties and were used in this thesis.

### 2.3.1 Time of flight and transmission profile

The time resolved transmission is measured by illuminating a multiple scattering sample with a pulsed laser whose pulse length is much shorter than the time of flight of the photons in the sample (which is in the nanosecond range in the performed experiments). Using a detector with time resolution in the picosecond range, such as a photomultiplier (PM) or an ultrafast gateable camera, single photons can be resolved. The setups used for the ToF and the TP width measurements are described with all details in ref. [36]. In this thesis I

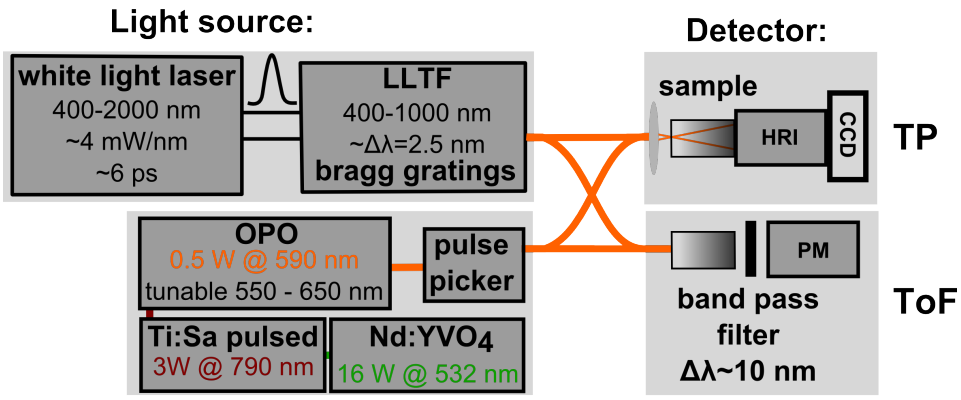


**Figure 2.7:** Sketch of the Time of flight (ToF) and Transmission Profile (TP) setup with either a Ti:Sa laser (pumped by a Nd:$YVO_4$ laser) followed by an OPO or a white light laser (Fianium WL-SC-400) followed by a laser line tunable filter (LLTF) as a light source. For the TP measurement the laser beam is focused on the sample surface and a high rate intensifier (HRI) followed by a CCD camera is used as detector while for the ToF setup the sample is placed in front of a photomultiplier (PM). A bandpass filter can be added in front of the detector for spectral measurements.

used minor modified versions of these setups.

As shown schematically in fig. 2.7 two different pulsed laser systems were used as light source. Most of the time a titanium sapphire (Ti:$Al_2O_3$) laser (Coherent HP Mira) pumped by a frequency doubled, diode pumped Nd:$YVO_4$ cw-laser (Laser Quantum, finesse pure) with an output of $P = 16$ W at $\lambda = 532$ nm was used. The titanium sapphire oscillator was mode locked to obtain pulses with a width of $\approx 250$ fs at a central wavelength of 790 nm. It is tunable between 700-1000 nm. These pulses are coupled into an optical-parametric-oscillator (OPO) from APE where the light is frequency converted (output tunable between 550-650 nm via the input wavelengths). This is done by performing a nonlinear three photon process followed by a second harmonic generation process down conversion in the visible via two nonlinear crystals. The cw output power of this system is $P \approx 0.5$ W at 590 nm with a spectral width of $\Delta\lambda \approx 1$ nm. The pulses generated in the HP Mira have a repetition rate of 76 MHz, which corresponds to measurement windows of 13.2 ns between two pulses. To extend this time a pulse picker can be used that picks every 15th pulse with a contrast ratio of 500:1 using an acousto-optical modulator. The laser intensity is regulated using absorbing OD filters before the sample is illuminated.

The advantage of this laser system is the relatively high output power which

allows for measurements of relatively thick and/or strongly scattering samples. I replaced this light source by another pulsed laser, to extend the accessible wavelength range. A white light laser (Fianium, WL-SC-400-8) with a total output power of $P \approx 8$ W in a wavelength range of 400-2500 nm was used. The pulses are in the picosecond range (strongly depending on the wavelength) and the system has a repetition rate of 80 MHz. The white light pulses are coupled in a spectral tunable filter (Fianium, LLTF VIS) that uses two spectral overlapping Bragg gratings to tune the wavelength between 400-1000 nm with a spectral width of 2.5 nm and an average output of 4 mW/nm.

The detection is made by a single photon counting method with time resolution in the picosecond range. This is realized with a photo multiplier (HPM-100-40, Becker & Hickel GmbH) for the ToF measurements. The acquisition card has 1024 time channels which leads to a time resolution of 19.5 ps for a measurement window of 20 ns. Thus, the laser pulses should be as delta shaped, but are broadened by the electrical response of the system. This response is then convoluted with eq. (2.12) to fit the data. A detailed description of the analysis can be found in ref. [36]. A bandpass filter (FWHM= 10 nm) is placed between the sample and the detector for spectral measurements.

The photons have to be measured time and space resolved to measure the TP width. In this setup the laser beam is focused with a lens (typically $f = 200$ mm) on the sample surface as sketched in fig. 2.6(a). An ultra fast gateable camera system is used as a detector. It consists of a high rate intensifier (La Vision, PicoStar, HRI) and a 16 bit monochromatic CCD (Andor Ikon, $512 \times 512$ pixels). The HRI can have an amplification of 360000 and the gate opens in 1 ns with time steps of 0.25 ns. The samples' surface is imaged with a lens ($f = 25$ mm, Schneider Kreuznach) on the HRI. The magnification is calibrated by using a mm grated paper in place of the sample. The exposure of the camera was chosen to be 600 ms. For each time step twenty images were averaged. A background defined close to the edge of the image was substracted before the transmission profile width was fitted by a Gaussian:

$$I(x,y) = I_{\max} \exp\left(\frac{(x_0 - x)/\sigma_x^2 + (y_0 - y)/\sigma_y^2}{2}\right) , \tag{2.28}$$

with $I_{\max}$ the maximum intensity of the Gaussian profile at the center position $(x_0, y_0)$. An image of a measured TP with its fit (contour) is shown in fig. 2.6(b). The square of the obtained width $\sigma_{\text{fit}} = \frac{\sigma_x + \sigma_y}{2}$ is then plotted against the observational time and corrected by an offset which accounts for a finite spot size of the incoming focused beam on the sample surface. More details can be found in ref. [54].

### 2.3.2 Large angle coherent backscattering cone

The width of the CBC is proportional to $1/k\ell^\star$. Thus, the width of the cone becomes very wide for strongly scattering samples such as $TiO_2$ powders. A large backscattered angular range should be measured to measure $\ell^\star$ of such highly scattering samples. I therefore used a coherent backscattering cone setup recording angles from $-60°$ to $60°$ as described in ref. [55, 35, 28, 54]. The setup is shown schematically in fig. 2.8(a).

The spectral tunable white light laser system was used as a light source. The beam is focused through an entrance hole in the half circle mount (1.2 m in diameter) of the 256 photodiodes which are the detectors. The beam is focused with the focal point at the diodes position to minimize the non-measurable angles in the backscattering direction. At small angles ($< 9.75°$) photodiode arrays (Hamamatsu, S5668) are used for a higher resolution of $0.15°$ at the cone tip while at larger angles ($< 19.55°$) single photodiodes (Hamamatsu, S4011) are used with a resolution of $0.7°$. For even larger angles ($< 60°$) the same diodes are positioned with a resolution of $\approx 1°$. The illuminating beam passes a circular polarizer before inciding on the sample. The filter wavelength range (380-780 nm) limits the spectral measurements. Another circular polarizer foil in front of the photo diodes filters single scattering events. The sample is mounted on a rotating motor to average out the static speckle pattern during the measurement.

Before entering the measurement arc, the parallel beam is led through an optical density (OD) filter wheel which is used for calibration of the photodiodes at different incident intensities. I implemented the filter wheel to automatize the calibration procedure as it has to be performed in spectral measurements for every used wavelength. The filter wheel changes the intensities from the minimal detectable intensity up to the diodes saturation value (using filters with OD 2.0 to OD 0.0). The reflecting OD filters are varied automatically by rotating the filter wheel via a motor controlled by the calibration program. A reference intensity is measured by splitting a part of the beam with a glass slide and leading it on a power meter via a lens. All diodes have a different response function and are thus calibrated before each measurement for each wavelength. A teflon sample is used for calibration as it has such a narrow cone that only the incoherent background (eq. (2.15)) is detected by the diodes. The incoherent background is then subtracted from the data as described in ref. [36]. Accounting for all mentioned calibrations, the CBC of a sample can be extracted as the one shown in fig. 2.8(b) for a commercial $TiO_2$ powder (R700, DuPont) measured at a wavelength of $\lambda = 670$ nm. The data can then be fitted (red solid line) by eq.(2.16) accounting for energy conservation

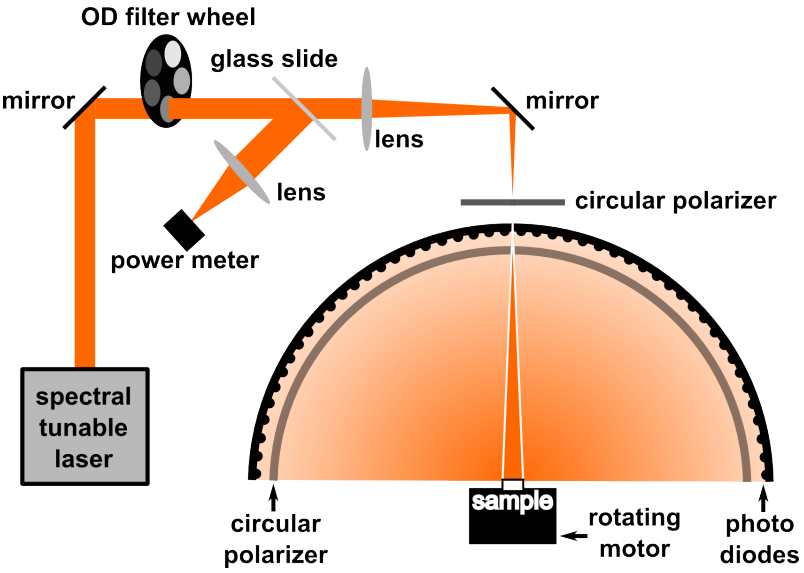


(a) large angle CBC setup

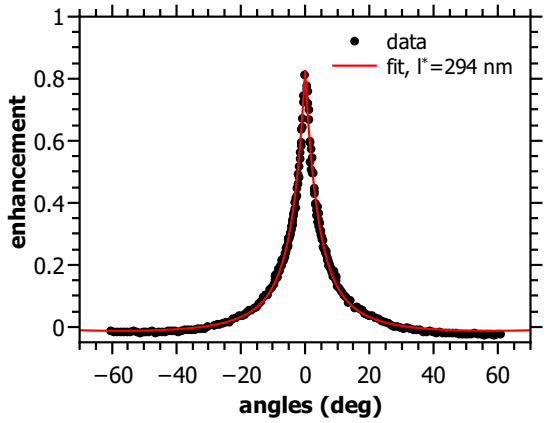


(b) CBC of R700

**Figure 2.8:** (a) Sketch of the large angle coherent backscattering cone setup: A beam from a spectral tunable laser passes an OD filter wheel and a glass slide that splits parts of the beam for calibration. The beam is then focused trough a small entrance in a half circle mount for photodiodes, which records the backscattered light of a sample illuminated by the light beam. The beam passes a circular polarizer before inciding on the sample. Another polarizer is mounted in front of the photodiodes. The sample is mounted on a rotating motor. (b) The cone data (black dots) of a $TiO_2$ powder sample R700 from DuPont measured at $\lambda = 670$ nm and the corresponding fit (red solid line) are shown.

(eq.(2.19)) and internal reflections (see eq.(2.17)). In this case, a transport mean free path of $\ell^\star \approx 294$ nm was obtained.

### 2.3.3 Commercial titanium dioxide

Most setups used in this thesis work in the visible part of the spectrum of light due to well developed optical sources and detectors in this wavelength region. This fact, as well as the interest in technological applications in this frequency regime, implies that we use a material with a high refractive index combined with a low absorption in the visible region for the preparation of strongly scattering samples.

A good candidate is titanium dioxide ($TiO_2$) which is, beside the aforementioned properties, commercially easily available and widely studied in material science. The high band gap $E_{\mathrm{bg}} \approx 3.05$ eV of titanium dioxide [56], which corresponds to a wavelength of $\lambda \approx 400$ nm makes it an ideal material for multiple scattering experiments in the visible.

There are three main polymorphs of titanium dioxide in nature (brookite, anatase and rutile) with anatase and rutile the most stable phases. Anatase has a refractive index of $n \approx 2.5$ at $\lambda = 589$ nm and a density of $\rho = 3.89$ g/cm$^3$ [57]. Rutile has a density of $\rho = 4.26$ g/cm$^3$ and is strongly birefringent with a refractive index of $n_{\mathrm{o}} = 2.6$ and $n_{\mathrm{e}} = 2.9$ at $\lambda = 589$ nm [57]. Synthesizing leads to an amorphous phase of $TiO_2$ with a density varying between $3.2-3.65$ g/cm$^3$ and a refractive index varying between $n = 2.0-2.5$ [58]. Near the band gap the refractive index is strongly wavelength dependent. Amorphous $TiO_2$ changes irreversibly to the anatase phase when heating above 400°C. The formation of the rutile phase sets in around $600 - 700$°C.

Mie scatterers with a size in the order of the wavelength are preferred to obtain strong scattering behavior as will be argued in sec. 3.1. In the Konstanz group, we have been working for a long time with multiple scattering samples made of commercially available powders of titanium dioxide from DuPont and Sigma-Aldrich. They have high polydispersities in the range between 25-47% with a mean diameter varying from 170 to 283 nm. The powders are characterized in detail in refs [27, 35, 28, 36]. To obtain densely packed powders in slab geometry, the powders are pressed to tablets in sample holders as shown in fig. 2.9. This leads to filling fractions of approximately $f \approx 0.5$. The powders are pressed between two glass plates to perform transmission experiments. One glass plate can be removed from the holder for CBC experiments to guarantee for a flat sample/air surface (see (3) in fig. 2.10(a)) to avoid additional reflections by the glass.

Deviations from classical diffusion have been observed for three powders from

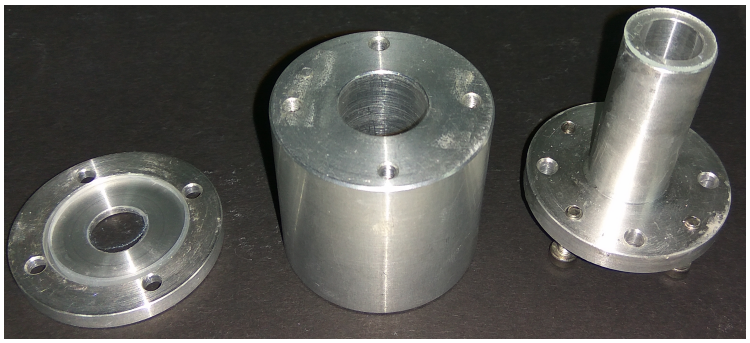

**Figure 2.9:** Image of the three main parts of the sample holders used to press the commercial $TiO_2$ powders. The lid (left) can be screwed on the cylindrical holder (middle) before the powder is filled in the holder and pressed with the stamp (right).

DuPont in the rutile phase (R700, R902 and R104)[19]. These white powders have an inverse turbidity $kl^*$ of 2.8, 3.4 and 3.7 at 590 nm[36]. Anatase as well as rutile powders from Sigma-Aldrich (respectively abbreviated AA and AR) with $kl^* = 6.4$ and 5.2 did not show any deviation from the diffusive behavior in ToF measurements [51, 59]. AA has a mean particle size of 170 nm with 47% polydispersity and AR has a mean particle size of 540 nm with 37% polydispersity [36].

In the experiments especially R700 was investigated due to its low $kl^* \approx 2.8$ value (at $\lambda = 590$ nm) and its strong deviations from diffusion [19]. Its mean particle diameter $d = 283$ nm with a polydispersity of 30% was reevaluated by measuring the size of 200 particles from scanning electron microscope (SEM) images (see fig. 2.10(b)).

## 2.4 Earlier experiments on 3D Anderson localization of light

Experimental verification of Anderson localization in 3D systems has been a challenging task for more than 50 years. There are several experimental reports ranging from ultrasound [15] to ultra cold atoms [16, 17, 41, 42] and most importantly for this thesis: light [60, 61, 18, 19]. But doubts have been raised concerning the interpretation of some of these results in terms of localization of light waves ([62, 63, 64] and [65, 66]) and for ultra cold atoms [67, 68]. In the following section I want to point out some experimental methods used to observe light localization and show some earlier results that were interpreted as

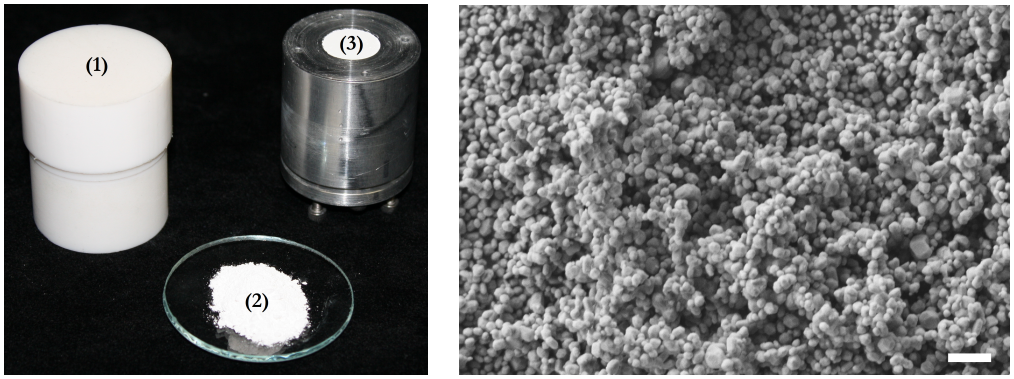


(a) sample holder (b) SEM image R700

**Figure 2.10:** (a) Image of the teflon sample used for calibration of the large angle CBC (1), a R700 powder from DuPont (2), and a pressed $TiO_2$ powder in the sample holder (3). (b) Scanning electron microscope image of R700. Scale bar: 1 $\mu$m.

Anderson localization of light in 3D and questioned after or will be questioned in this thesis.

### Static transmission

Early claims of light localization were based on the measurement of the static transmission through slabs of strongly scattering semiconductor powders [60]. In diffusive ($k\ell^\star \gg 1$) sufficiently thick ($L \gg \ell^\star$) and absorbing slabs, the transmission scales with $\exp(-L/L_\mathrm{a})$, with $L_\mathrm{a}$ the macroscopic absorption length. In contrast, in the localization regime the total transmission is dominated by the localization length and is proportional to $\exp(-L/\xi)$ on top of absorption [62]. Wiersma *et al.* [60] interpreted an experimentally observed exponential decay of the static transmission as light localization ignoring absorption in their grinded gallium arsenide powders. The same data was explained later by absorption only [62, 63, 64], such that localization effects can be excluded in these measurements.

### Time resolved transmission

As mentioned earlier, the time resolved transmitted intensity is an experimental measurement tool to look for time delayed photons as signs of light localization. Störzer and coworkers [18, 59, 69, 70] observed deviations from diffusive behavior for the long time tail in time of flight measurements through

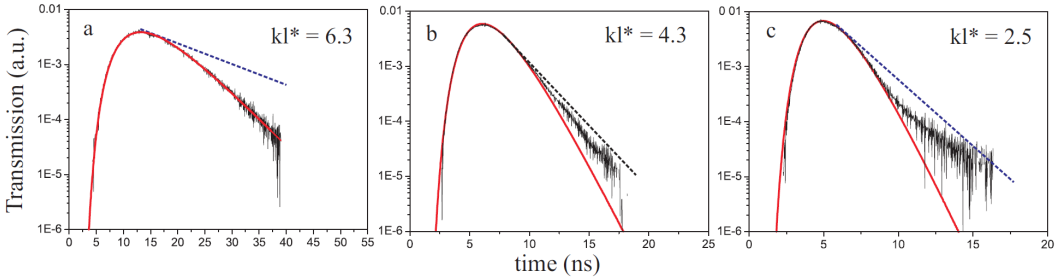


**Figure 2.11:** Time of flight measurements of three $TiO_2$ (Ti-Pure (a), R902 (b) and R700 (c)) powder samples fitted by diffusion theory (red lines). The corresponding values of $k\ell^\star$ are given in the figures. The respective values of the absorption length are indicated by the slope of the blue dashed lines. The figure is taken from ref. [18] and modified.

disordered, highly scattering powders of titanium dioxide ($TiO_2$) and interpreted them as signs of localization. They increased the scattering strength (decreasing $kl^*$ by using different commercial $TiO_2$ powders) from $kl^* = 6.3$, where pure diffusive behavior was observed, to $kl^* = 2.5$, where clear deviations from diffusion occur (see fig.2.11). They fit their data with eq. (2.25) using an empiric time dependent diffusion coefficient [59]

$$D(t) = D_0 \frac{\tau_{\text{loc}}^a}{(\tau_{\text{loc}}^m + t^m)^{\frac{a}{m}}} \ , \tag{2.29}$$

with $\tau_{\text{loc}}$ the localization time (the time the photons travel before localization effects set in), $a$ the localization exponent, and $m$ a crossover exponent that describes the scaling from diffusion to localization. Their data were interpreted as a first observation of a transition from a diffusive to a localizing state for light waves in a multiple scattering sample. Let us note here that this interpretation will be questioned later in this thesis as published elsewhere [54, 71].

### Spatial and time resolved transmission

In the same $TiO_2$ samples Sperling *et al.* [19] observed a plateau in the transmission profile width for long times as expected from localization. Figure 2.12 shows measurements of the transmission profile (TP) for a lower scattering sample with $k\ell^\star = 6.4$ (a) that behaves purely diffusive and a stronger scattering sample with $k\ell^\star = 2.7$ (b) that shows clear deviations from classical diffusion. Equation (2.27) shows that the width $\sigma^2$ gives a direct measurement of the localization length $\xi$. Sperling *et al.* [19] obtained a localization length

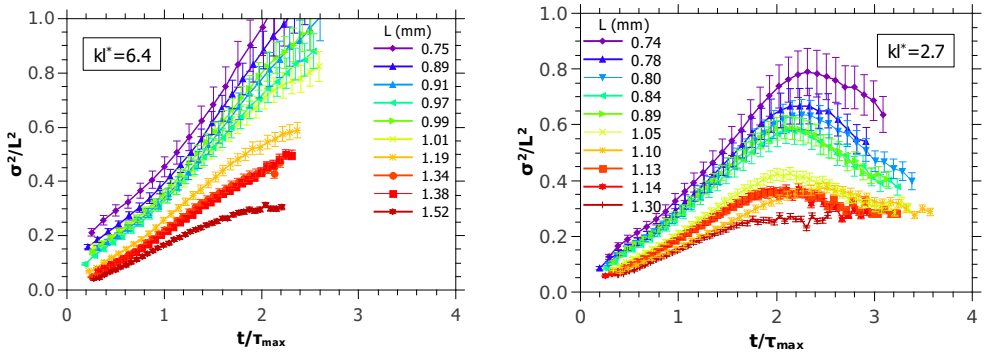


(a) Aldrich Anatase (b) DuPont, R700

**Figure 2.12:** Time dependent measurements of the mean squared width $\sigma^2$ of the transmission profile for different $TiO_2$ powder samples: (a) Aldrich Anatase with $k\ell^\star = 6.4$ shows a linear increase in time as predicted for diffusive samples. (b) DuPont R700 with $k\ell^\star = 2.7$ shows a plateau for long times as predicted for the localized regime. Figure taken from ref. [19].

of $\xi = 670$ $\mu$m in the long time limit for the sample measured in fig. 2.12(b).

The data set on transmission profile measurements shown here, the time of flight distributions shown above, as well as the static transmission measurements published in several articles [18, 59, 69, 70, 19, 66, 72] led to a consistent interpretation of light localization in 3D samples made of titanium dioxide. This will be questioned in the next section by new careful experimental tests.[3]

## 2.5 Questioning the localization interpretation

In this section I will show sensitive experimental tests on light scattering using the same $TiO_2$ powders as Störzer *et al.* [18] and Sperling *et al.* [19] that question their data interpretation of light localization. I performed these experiments at the beginning of my doctoral studies.[4]

[3]Doubts have also been raised earlier [65], but no experimental tests to proof these concerns were performed at this time.

[4]This section on experimental tests in commercial "white paints" is taken in large parts literally from a publication of my own and coworkers [54].

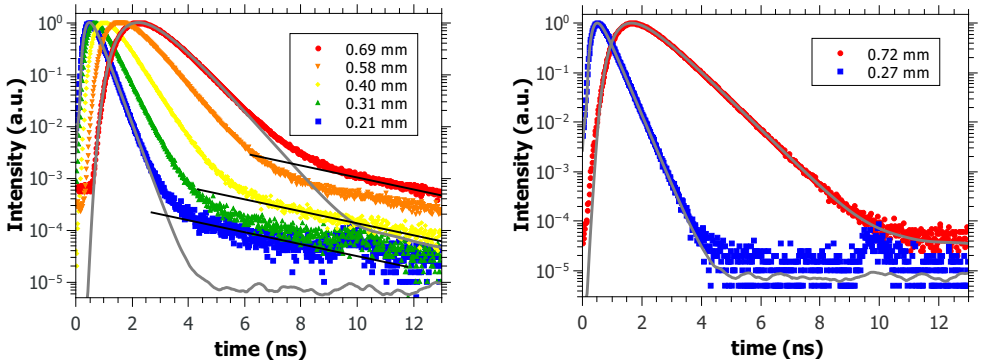


(a) R700 (b) Aldrich anatase

**Figure 2.13:** (a) Size dependent ToF distributions for R700 starting from a small sample size ($L = 0.69\,\text{mm}$) going down to very thin sample sizes ($L = 0.21\,\text{mm}$). The diffusive fit (solid gray line) does not match at long times. Black lines (guide to the eye) are shown to emphasize the exponential behavior. (b) ToF distributions for a thick ($L = 0.72\,\text{mm}$) and a very thin ($L = 0.27\,\text{mm}$) AA sample are shown. The diffusion fit (solid gray lines) matches perfectly. The incident wavelength is 590 nm for all measurements. Figure same as in ref. [54].

### 2.5.1 Samples thinner than the previously inferred localization length

In the localized transport regime, the theory of Anderson localization predicts the waves to be confined within a certain length scale, the localization length $\xi$. In previous experiments, this length was obtained from TP measurements, finding $\xi_{\text{R700}} = 670\,\mu\text{m}$ for R700 [19]. It is expected that decreasing the thickness of the slab-shaped samples well below the localization length will lead to a reduction of the localization signatures since large spatial localizing modes should be significantly disturbed by boundary effects as described in sec. 2.2.3. Figure 2.13 shows ToF distributions of AA and R700 for various thicknesses $L$. A series of R700 samples, where the largest sample is just as thick as the earlier evaluated localization length, can be seen in fig. 2.13(a). For comparison, fig. 2.13(b) shows two AA samples. A diffusive fit using eq. (2.12) for the thinnest and the thickest sample of each material is shown (gray lines).[5] For all R700 samples, even those in the $L < \xi$ regime, a clear deviation from the diffusion theory is present at long times. The photons in the long time tail seem to occur as a second exponential (black lines in fig. 2.13(a)) with

[5]The noise in the fit-curves is due to the convolution of the theory-function with a measured laser reference pulse[72].

a larger time constant. In contrast, all AA closely follow the diffusion theory predictions. These experimental observations are a first sign that the previous observed deviations from diffusion [18, 19] cannot consistently be explained by light localization.

### 2.5.2 Lowering the turbidity

As introduced in sec. 2.2.3 Anderson localization in 3D occurs as a disorder driven phase transition. The disorder is quantified by the turbidity $(k\ell^\star)^{-1}$ as obtained from the width of coherent backscattering cone. A sensitive test to check whether the long time tail originates from a second process different from localization is to strongly decrease the disorder (increase $k\ell^\star$). In previous experiments the turbidity was varied by using different powders [18] (see fig. 2.11) and by changing the incident wavelength [19, 72]. Here the accessible range of $k\ell^\star$ is expanded by lowering the refractive index contrast between the particles (refractive index of $n \approx 2.7$ [57]) and the surrounding medium, increasing thus the transport mean free path $\ell^\star$, by replacing the surrounding medium air ($n = 1$) by $H_2O$, agarose gel ($n \approx 1.33$) or glycerol ($n = 1.47$ at $\lambda = 589$ nm [73]) as a surrounding medium. The optical thickness $\ell^\star/L$ was kept constant by increasing the sample thickness to obtain similar flight times in time of flight experiments.

Figure 2.14(a) shows a ToF distribution (black curve) of R700 surrounded by agarose gel. Coherent backscattering [38, 55] was used to quantify $k\ell^\star \approx 10$. Measuring the same sample with a 590 nm bandpass filter (10 nm FWHM; BP590, orange squares in fig. 2.14(a)) in front of the detector, as described in ref. [72], allows us to probe the light transmitted at the incident wavelength. Diffusive fits for both measurements are plotted in gray. The ToF with filter follows the expected distribution for diffusive transport better than the non filtered one which shows a much more pronounced upturn for the long-time tail. This long-time tail must thus have been wavelength shifted, and is unlikely to be caused by localization since $k\ell^\star \approx 10$ should be far in the diffusive regime. The same measurement was also performed with water or glycerol as surrounding medium, leading to the same results. Using agarose as matrix led to solid samples and avoids experimental difficulties with sedimantation of the $TiO_2$ particles in the matrix medium.

Similarly, signs of localization are tested with the TP method [19] by suspending R700 in water and evaluating the transmission profile width with and without the 590 nm bandpass filter (see fig. 2.14(b)). The width of the transmitted profile should show a linear increase for a diffusive sample [52]. The data without filter (black dots) show a deviation from the linear diffusive increase

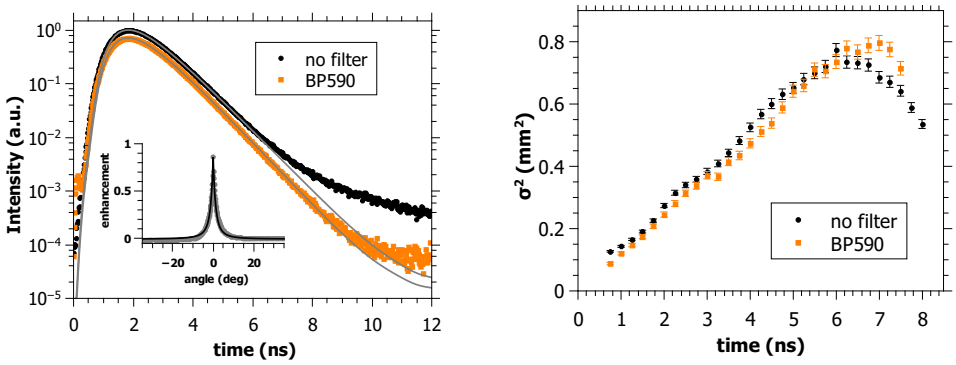


(a) Time of flight: R700 in agarose

(b) Transmission profile width: R700 in $H_2O$

**Figure 2.14:** ToF distributions (a) and TP widths (b) for a fixed incident wavelength $\lambda_{\text{inc}} = 590$ nm with (orange squares) and without (black dots) bandpass filter set to the incident wavelength (FWHM 10 nm). In (a) a sample ($L = 2.3 \pm 0.1$ mm) of R700 solved in agarose gel was used. The gray lines show diffusion fits for both curves. Inset: backscattering cone used to determine the mean free path ($\ell^\star = 1.0 \pm 0.1\,\mu$m)[55]. In (b) R700 powder was solved in $H_2O$ (ratio 1 : 1). The profile width was determined following ref.[19]. Figure same as in ref. [54].

of the width at long times. This deviation occurs similar to the one observed in ref. [19], but in a higher $k\ell^\star$ regime. The same results were obtained for the TP with glycerol as surrounding medium. Note that for both measurement methods (ToF and TP) the data with a bandpass filter show deviations from classical diffusion [72]. However, the filter has a FWHM bandwidth of 10 nm and thus some wavelength shifted light can still pass to the detector.

In conclusion, measuring ToF's and TP's, wavelength shifted photons leading to kinks at long times are observed, which were earlier interpreted as localization signatures. These observations are now present in a regime of low turbidity where no localization effects are expected.

### 2.5.3 Refitting static transmission data

In early experiments in the Konstanz group, indications of localization were found in static transmission measurements in an exponential scaling $\exp(-L/\xi)$ on top of absorption $\exp(-L/L_\mathrm{a})$ performed on slabs of R700 [59, 69]. Deviations from diffusion were found to be consistent with the inferred localization length extracted from localization fits ([51], eq. 2 in ref. [59]). The static transmission data could not be explained by absorption only in contrast to earlier experiments by Wiersma *et al.* [60] which were explained by simply absorption [62, 64].

At this time the absorption length was obtained as a result of the mentioned localization fit on the ToF distributions, and gave a result of $L_\mathrm{a} = 157\,\mu$m ( [59], see black line in fig. 2.15). Extracting the absorption length by fitting only the diffusive part of R700 ToF distributions by diffusion theory yields a smaller average absorption length of $L_\mathrm{a} = 106.5 \pm 8.8\,\mu$m than the one obtained by the localization fit[6]. This new absorption length value allows us to re-interpret the static transmission data of ref. [59, 69]. The exponential decay is now explainable by absorption alone (gray dashed line in fig. 2.15).

### 2.5.4 Transmission profile of Aldrich Rutile

The same exponential signatures of localized light and absorbed light in static transmission data make it very difficult to distinguish these effects and should be handled with care. A clear data analysis can only be guaranteed by an absorption-independent time-resolved method such as the transmission profile

[6]Despite better data evaluation, a diffusion fit instead of a localization fit was used nowadays. It turned out that the diffusion fit results in reliable absorption times for all samples of one powder, whereas the localization fit did match the data poorly and produced scattered (and quite different) absorption times.

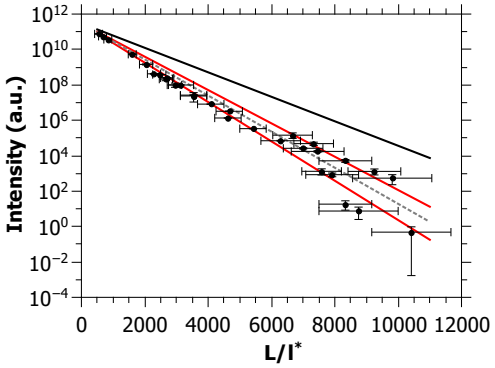


**Figure 2.15:** Total transmission of a R700 sample as a function of sample thickness $L$ normalized to $l^*$. Same data as in ref.[69]. The gray dashed line shows an exponential according to the absorption length $L_a = 106.5\,\mu$m with an error of $\pm 8.8\,\mu$m (red lines) obtained by new diffusion fits to the ToF data that will be shown in fig. 2.22(a). The absorption decay can explain the data, without assuming localization effects. The black line shows an exponential according to $L_a = 157\,\mu$m, as obtained in ref.[59]. Figure same as in ref. [54].

width measurements from Sperling *et al.* [19]. In the following I will show that also in this method, data analysis has to be handled with care and earlier observed deviations from diffusion in the TP of AR can be explained without localization effects.

While all measured $TiO_2$ powders from DuPont (e.g. R700) have similar absorption times ($\tau_a \approx 1$ ns), Aldrich Rutile shows less absorption (and thus longer absorption times $\tau_a \approx 5 - 6$ ns). This leads to very long flight times in the ToF measurements with times well above the time window between the laser pulse and its afterpuls(es) ($\Delta t \approx 13.2$ ns for a repetition rate of 76 MHz). Using a pulse picker which weakens the afterpulses intensity up to three orders of magnitude, a ToF of Aldrich Rutile can still be measured (see fig. 2.16(a), black dots).

Aldrich Rutile shows a diffusive ToF which is disturbed only by the second afterpulse. No deviations from diffusion are observed and a measurement with a BP590 filter on the incident wavelength $\lambda_{inc} = 590$ nm shows the same ToF behavior (see fig.2.16(a), orange squares). But, as mentioned in ref. [36], Aldrich Rutile shows a plateau in the TP width measurement. In fig.2.16(b) a TP measurement of Aldrich Rutile solved in water is shown (black dots). With a filter on the incident wavelength the same plateau is observed. In this low scattering regime this plateau cannot be interpreted as localization, but a wavelength dependent effect such as in the DuPont powders can also be

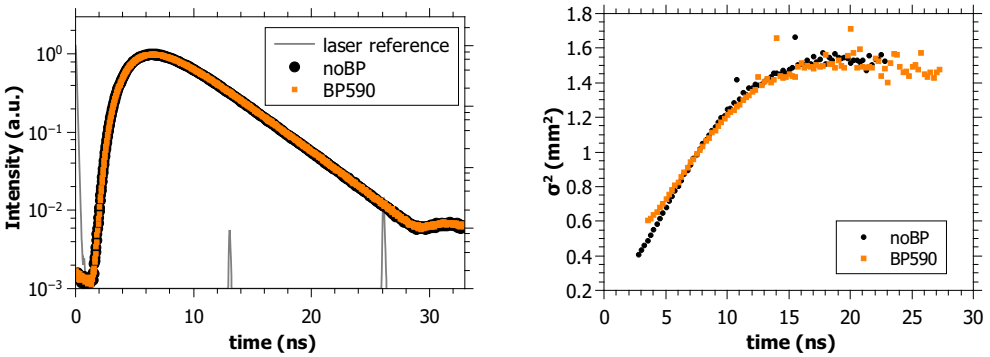


(a) Time of flight: Aldrich Rutile

(b) Transmission profile width: Aldrich Rutile in $H_2O$

**Figure 2.16:** ToF distributions (a) and TP widths (b) for a fixed incident wavelength $\lambda_{inc} = 590$ nm with (orange squares) and without (black dots) bandpass filter set to the incident wavelength (FWHM 10 nm). In (a) a sample ($L = 1.2 \pm 0.1$ mm) of Aldrich rutile was used. The gray line shows the measured laser reference. In (b) Aldrich rutile powder was solved in $H_2O$ (ratio 1 : 1). The profile width was determined following ref.[19].

excluded. Reference [36] mentioned problems in the evaluation of the TP data due to afterpuls effects. A detailed image analysis showed that the afterpulse (note that even with pulse picker an afterpulse with a contrast of 500:1 is present, see sec. 2.3.1) will be shifted in space (due to the optical setup inside the pulse picker) and thus enters the sample slightly at a different position. This leads to a shifted TP of the afterpulse overlapping with the TP of the initial laser pulse at large times. The measured width of the TP will be influenced by this shift for Aldrich Rutile where long flight times, longer than $\Delta t$, are measured. While characterizing this data analysis problem, another evaluation problem was noticed. An image background is subtracted in the data analysis before the TP width is fitted. The background was taken from the edge of the images up to a certain distance to the TP center. This distance was fixed in the evaluation process to values appropriate for the DuPont powders. Due to the long flight times and thus wide profiles of Aldrich rutile the background needs to be evaluated very close to the edge of the images for the Aldrich Rutile powder. Evaluating the background closer to the edge of the images leads to different profile results for Aldrich Rutile (see fig. 2.17(b)), but did not influence the result of the DuPont powders (see fig. 2.17(a)). The red squares show the old data analysis while the black circles show the new data analysis.

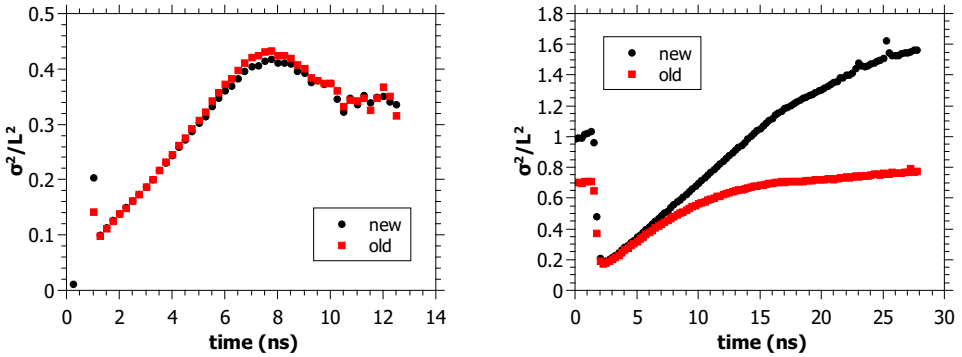


(a) TP width: R700 (b) TP width: Aldrich Rutile

**Figure 2.17:** Refitting TP width data using a different background analysis (see text): In (a) a sample ($L = 1.0 \pm 0.1$ mm) of R700 was measured at $\lambda_{inc} = 580$ nm. The profile width was determined with an old data evaluation approach following ref.[19] (red squared) and a new approach described in sec. 2.5.4 (black diamonds). In (b) a sample ($L = 1.1 \pm 0.1$ mm) of Aldrich rutile was evaluated the same way at $\lambda_{inc} = 580$ nm.

For Aldrich Rutile a linear increase of the profile width can be observed now as expected from diffusion. Still a kink is observed at the time where the afterpulse disturbs the image analysis. For the DuPont powders and Aldrich Anatase the new analysis does not alter the results of the TP width due to the shorter photon flight times.

### 2.5.5 Weak fluorescence signals

A first crude spectral analysis of the ToF distribution for a sample consisting of R700 embedded in agarose was shown in fig. 2.14(a). This measurement indicates that the deviation in the long-time tail originates from wavelength shifted photons with respect to the incident value $\lambda_{inc} = 590$ nm. In figure 2.18 I further investigate the spectral shift of the photons in the long-time tail.

ToF's of a pure R700 sample were measured using different filters, similarly to measurements performed in ref. [72]. The distribution with no filter between the sample and the detector (black dots) shows a strong upturn of the long-time tail. A measurement with a bandpass filter around 590 nm reveals that the non wavelength shifted light propagates through the sample diffusively[7] (orange

[7]Up to the small effect in the late time due to the finite width of the BP590 which was already discussed in sec. 2.5.2.

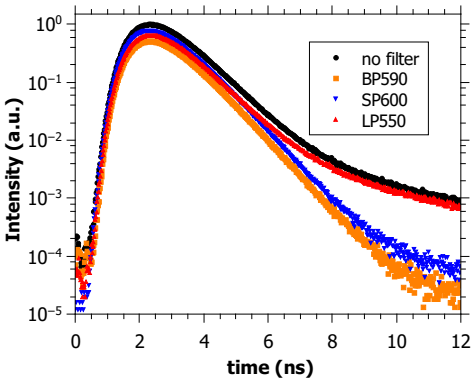


**Figure 2.18:** ToF distribution of a R700 sample ($L = 0.83\,\mathrm{mm}$) measured without filter (no filter), a bandpass filter around 590 nm (BP590), a shortpass filter 600 nm (SP600) and a longpass filter above 550 nm (LP550) with an incident wavelength $\lambda_{\mathrm{inc}} = 590\,\mathrm{nm}$. The red-shifted photons show a long-time tail, indicating a fluorescence while the blue shifted and non-shifted light behaves purely diffusively. Figure same as in ref. [54].

squares). A measurement with a shortpass filter blocking all photons above 600 nm (blue down triangle) highlights that the long time tail is dominated by red-shifted light: the long-time tail is blocked by the SP600 filter. The ToF using a longpass filter for wavelengths above 550 nm (red up triangle) nearly matches the measurement with no filter, strengthening the observation of a signal in the red-shifted region.[8]

In the spectral study shown in fig. 2.18, all the photons in the long-time tail occur as red-shifted light. In fig. 2.14(a) the long-time tail occurs for wavelength shifted photons in a low scattering regime. An exponential behavior of the long-time tail in ToF distributions for very thin samples is observed in fig. 2.13(a). All together, these observations suggest that localization claims do not hold anymore and that a lifetime process, such as fluorescence, is most likely the source of these photons.

Thus, in order to quantify the origin of the long-time tail in the ToF and the kink in the TP measurements I searched for a fluorescent signal in the visible region. The white paint powders were therefore spectrally analyzed in a sensitive micro-luminescence microscope setup, further described in ref. [74]. The light source is a widely tunable pulsed ps-laser system and the detector is an EMCCD[9] placed behind a monochromator grating. In all samples that were

[8]These observations are in contrast to earlier observations published in ref. [69], in which a problem with the used filter cannot be excluded.
[9]Electron multiplying charge-coupled device

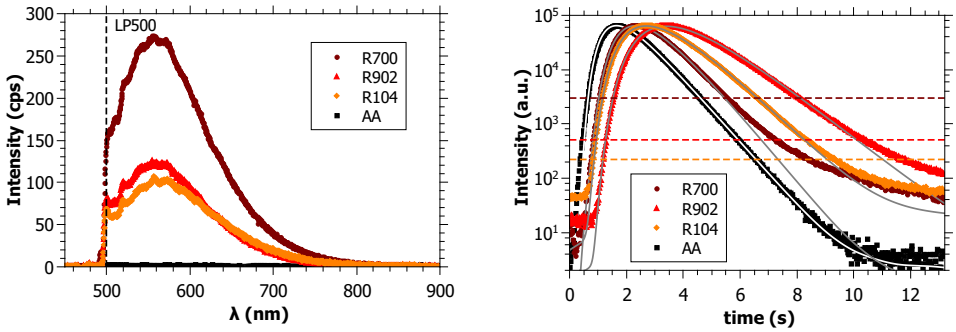


(a) Emission spectra (b) ToF

**Figure 2.19:** (a) Emission spectra of R700 (dark red dots), R902 (red triangles), R104 (orange diamonds) and AA (black squares) with $\lambda_{\text{inc}} = 485\,\text{nm}$ using a long pass 500 nm filter (LP500) and a laser power of $P = 50\,\mu\text{W}$. (b) ToF measurements of the same powders. Vertical lines indicate the deviation of the data from the purely diffusive behavior as shown by diffusion fits (grey and white lines). The thickness of the samples differ with R700 ($L = 0.83$ mm), R902 ($L = 1.12$ mm), R104 ($L = 0.92$ mm) and AA ($L = 0.72$ mm).

previously claimed to localize (R700, R902, R104) a weak fluorescent signal is observed with a broad emission in the visible range. The photo luminescence (PL) spectra of R700, R902, R104 and AA are shown in fig. 2.19(a). All samples are excited at $\lambda_{\text{inc}} = 485\,\text{nm}$ with a laser power of $P = 50\,\mu\text{W}$. A longpass filter 500 nm was used to filter the scattered laser light. R700 shows the strongest signal followed by R902 and R104. For AA no fluorescent signal within the sensitivity of the setup is observed. This relative intensity dependency follows the material dependent $kl^*$-scaling of the observed deviations from diffusion in ref. [27, 18, 28, 19, 36]. Figure 2.19(b) shows ToF measurements for these powders. The start of the deviations from the diffusive fit (grey and white lines) are highlighted with vertical dashed lines. The same scaling is observed as in the PL spectra. R700 shows the strongest deviations followed by R902 and R104 while AA shows no deviations.[10] No fluorescent signal was detected for a rutile phase powder from Aldrich (data not shown) consistent with the observation in sec. 2.5.4, excluding the rutile phase to be the origin of the deviations from diffusion.

Measurements of the fluorescent lifetime of the samples were possible with a Hanbury-Brown-Twiss experiment followed by an avalanche photodiode (see ref.[74]). An average lifetime of $\tau_{\text{L}} = 3.85 \pm 0.07\,\text{ns}$ was extracted from exponen-

[10]The absolute flight times vary due to the different thicknesses $L$ of the prepared samples.

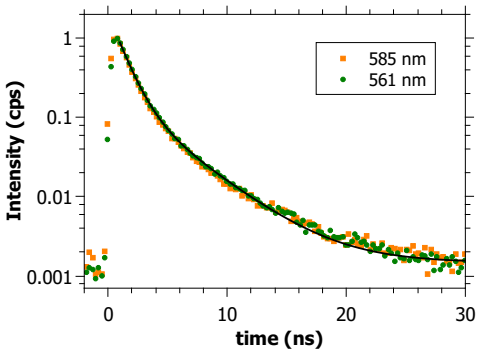


**Figure 2.20:** Lifetime measurements in a R700 sample for two different incident wavelengths (585 nm (orange squares) and 561 nm (green dots)). The corresponding bi-exponential fit is shown as a black line. The first exponent corresponds to the electronic setup response and can be neglected. Figure same as in ref. [54].

tial fits to lifetime measurements for two incident wavelengths $\lambda_{\text{inc}} = 585\,\text{nm}$ and $\lambda_{\text{inc}} = 561\,\text{nm}$ (see fig. 2.20).

In ref. [72] an increase of the long-time tail for shorter wavelength was observed, explained by the wavelength dependency of $kl^*$. Figure 2.21(a) shows PL spectra of R700 for three different incident wavelengths. For shorter wavelength, the PL spectra increases as can be seen in the inset of fig. 2.21(a) in a range from 540 nm to 590 nm. This measurement explains the increase of the long-time tail in ToF distributions and stronger deviations for TP's with decreasing wavelength without assuming localization effects.

The power dependent study of the fluorescence of R700 in fig. 2.21(b) shows an increase with increasing incident power. The inset of fig. 2.21(b) shows the power dependent integrated intensity. A slight saturation is observed as expected from fluorescence. This is in contrast to the nonlinear power dependent increase of the long-time tail in ToF distributions in ref. [28, 72, 36], which have found an increase in the long-time transmitted intensity with higher power. This might be due to the fact that the ToF was measured in transmission, while the fluorescence spectra were recorded in reflection. A volume of saturation for the fluorescence excitation located near the incident surface, growing with incident intensity, would explain such geometrical difference.

The occurrence of this fluorescence only in powders from DuPont led to the search of impurities in these white paint materials. An elementary analysis showed 0.2% of carbon in R700, which could originate from organic material. In AA and AR no carbon was found, consistent with the absence of a fluorescent

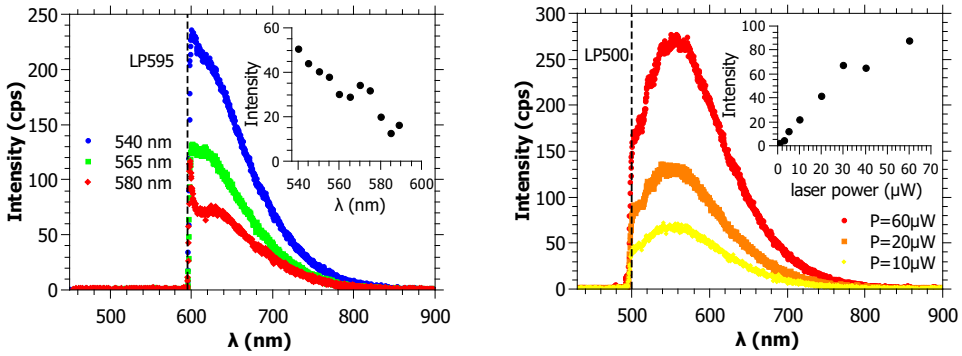


(a) Wavelength dependency (b) Power dependency

**Figure 2.21:** (a) PL spectra for three incident wavelengths (540 nm (blue dots), 565 nm (green squares) and 580 nm (red diamonds)) are shown using a longpass 595 nm filter (LP595). Inset: integrated PLE spectra for $\lambda_{\text{inc}}$ between 540 and 590 nm (arbitrary unit). (b) PL spectra for three laser powers (60 $\mu$W (red dots) 20 $\mu$W (orange squares) and 10 $\mu$W (yellow diamonds)) with $\lambda_{\text{inc}} = 485$ nm using a longpass 500 nm filter. Inset: integrated PLE spectrum for laser power between 1 $\mu$W and 60 $\mu$W. Figure same as in ref. [54].

signal.

### 2.5.6 A time delaying fluorescent diffusion model

In this section I am going to study how inelastic effects other then absorption can alter the functional form of the time of flight (eq. (2.12)). I consider here a fluorescent process, where photons are absorbed with a certain probability and are then reemitted on a red-shifted wavelength after some fluorescent decay time. This changes the temporal expand of the diffusive cloud if the measured photons are not spectrally resolved. In a very simplified picture one can think of a fluorescent process as of an excitation of an electron via photon absorption in a three level system from the electrons ground state to an excited state. This is followed by a non-radiative decay to a more stable excited state (e.g. via vibrational relaxation). Afterwards there is a spontaneous emission back to the ground state. The spontaneous emitted photon has a lower energy than the absorbed photon and is thus red-shifted in wavelength. Moreover, the decay time of the spontaneous emission is typically longer (in the nanosecond range) than the non-radiative decay (in the picosecond range). The following model has already been published by myself and coworkers in ref. [54] and was developed in collaboration with Mirco Ackermann.

To account for such inelastic scattering in experiments the time of flight (ToF) intensity distribution $I(t)$ and the time dependent width of the transmission profile (which is a time and spatially resolved transmission measurement), both known from the diffusion theory [51, 59, 52], are extended by including a fluorescence decay. Let us assume that there is an absorption rate $r_{\mathrm{fl}}$ by which photons traveling through the sample are absorbed. Those photons are re-emitted after a time $t_{\mathrm{d}}$ with a probability density proportional to $\exp(-t_{\mathrm{d}}/\tau_{\mathrm{fl}})$, $\tau_{\mathrm{fl}}$ being the fluorescence lifetime. For a photon that, without fluorescence, takes a time $t_{\mathrm{sc}}$ to travel through the sample, this gives a probability density of being delayed by an additional time $t_{\mathrm{d}}$ due to fluorescence of

$$p(t_{\mathrm{sc}}, t_{\mathrm{d}}) = (1 - r_{\mathrm{fl}}\, t_{\mathrm{sc}})\delta(t_{\mathrm{d}}) + r_{\mathrm{fl}}\, t_{\mathrm{sc}}\, \frac{\exp(-t_{\mathrm{d}}/\tau_{\mathrm{fl}})}{\int_0^\infty \exp(-t'/\tau_{\mathrm{fl}})\, \mathrm{d}t'} \ . \tag{2.30}$$

The first term of the sum takes into account the photons that were not delayed ($t_{\mathrm{d}} = 0$), while the second describes those which participated in a fluorescence event. Here it is assumed that the absorption rate $r_{\mathrm{fl}}$ is sufficiently small such that re-absorption of fluorescent photons can be neglected.

Let us recall that $I(t_{\mathrm{sc}})$ is the intensity of photons that arrive at time $t_{\mathrm{sc}}$ without fluorescence. The intensity $I_{\mathrm{fl}}(t)$ of a sample showing fluorescence can now be calculated by integrating $I(t_{\mathrm{sc}} = t - t_{\mathrm{d}})$ over all delay times, weighted by the delay probability density $p(t-t_{\mathrm{d}}, t_{\mathrm{d}})$ that the photons take an additional time $t_{\mathrm{d}}$ due to fluorescence. This gives a ToF distribution of

$$I_{\mathrm{fl}}(t) = \int_0^t I(t - t_{\mathrm{d}}) p(t - t_{\mathrm{d}}, t_{\mathrm{d}})\, \mathrm{d}t_{\mathrm{d}} \ . \tag{2.31}$$

For the transmission profile width, $I(t)$ in eq. (2.31) needs to be replaced by a position dependent intensity distribution $I(r, t)$ to give a 2D profile $I_{\mathrm{fl}}(r, t)$ from which the width can be calculated according to ref.[52]. For fitting experimental ToF and the TP width data, the curves calculated with eq. (2.31) can be convoluted with the time dependent detector response function.

This model can now be used to test whether the measured fluorescent signal suffices to explain old and new data of ToF and TP width measurements in $TiO_2$ samples. In figure 2.22 ToF and TP measurements of R700 for different sample thickness are shown and fitted (black lines) with the extended diffusion equations that include fluorescence (eq. 2.31). The corresponding ToF distribution and TP width are always fitted *together* with the same set of parameters. Each dataset was fitted with only four free parameters: the fluorescence rate $r_{\mathrm{fl}}$, the (usual) absorption time $\tau_{\mathrm{a}}$, the diffusion constant $D$ and an offset to

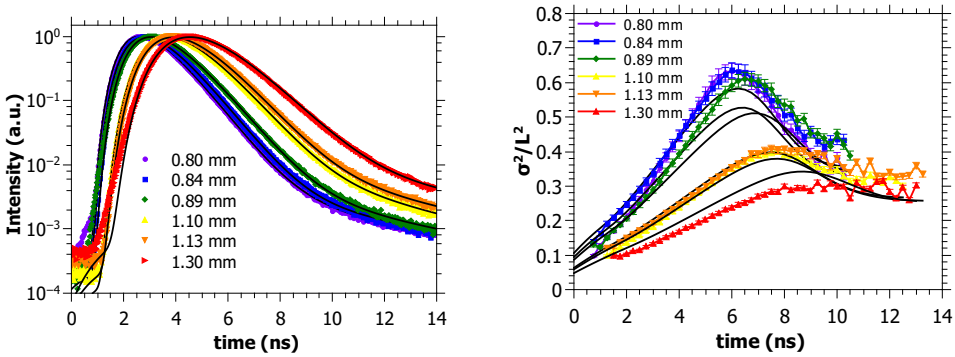


(a) ToF (b) TP

**Figure 2.22:** Measured ToF distributions (a) and TP widths (b) of R700 for different sample sizes $L$. ToF data taken from ref.[36]. TP data taken from ref.[19]. Diffusion fits including fluorescence from eq. 2.31 with fixed $\tau_{\text{fl}} = 3.85\,\text{ns}$ are shown as black lines. For each sample size, the corresponding ToF and TP are fitted together, the ToF in log space and the TP in real space. The ToF depends only on three fit parameters ($r_{\text{fl}}$, $\tau_{\text{a}}$ and $D$), so does the TP ($r_{\text{fl}}$, $D$ and an offset to compensate the finite size of the illuminating beam).

compensate the spot size enlargement caused by the finite size of the illuminating beam in the TP measurements. Note that the fluorescence lifetime is not fitted, but set to $\tau_{\text{fl}} = 3.85\,\text{ns}$ as obtained from lifetime measurements shown in fig. 2.20. The second exponential in the ToF's is recovered very well by this decay time. In general, a remarkable good agreement with the data is observed. The upturn of the long-time tail in the ToF distributions can be explained by the extended theory. Furthermore, all features of the TP width measurements can be explained with this extended diffusion model, in particular the thickness dependent saturation and narrowing at long times, without invoking localization effects (contrary to ref. [19]). The latter appears essentially because photons on relatively short diffusion paths (arriving at the backside of the slab at times $t < \tau_{\text{max}}$) contribute mostly to the central part of the TP and thus, their fluorescence signal, which is delayed by the fluorescence lifetime, appears mostly in the central part of the TP. This effect gives rise to the peak in the TP width. The fits give an average fluorescence absorption rate of $r_{\text{fl}} = 0.0044 \pm 0.0006\,\text{ns}^{-1}$, an average diffusion constant of $D = 11.9 \pm 0.7\,\text{m}^2/\text{s}$ and an average absorption time of $\tau_{\text{a}} = 0.92 \pm 0.03\,\text{ns}$.

## 2.6 Conceptual and experimental difficulties in observing Anderson localization of light in 3D

In the last section I presented new measurements that show features previously interpreted as signs of Anderson localization [18, 59, 69, 70, 19, 66, 72], but in regimes where no localization should occur. ToF measurements of very thin samples ($L < \xi$) still show deviations from diffusion, contrary to an expected transition to pure diffusion in the Anderson localization picture. Furthermore, lowering the turbidity $(kl^*)^{-1}$ by changing the surrounding medium of the scattering particles does not affect the long-time tail. This is also unexpected for Anderson localization since $k\ell^\star$ is well above the expected transition value for these samples. It was also shown that the static transmission data of ref. [59, 69], previously interpreted as a localization signature, can be actually described with absorption only, further weakening the interpretation of localization. All deviations from diffusion in an Aldrich Rutile $TiO_2$ powder are explained by a data evaluation problem.

Besides the aforementioned observed inconsistencies, the deviations from diffusion occurred as a red-shifted signal in ToF distributions. Thus, PL spectra are measured for all mentioned powders in a fluorescence microscope setup, with the result that all powders earlier claimed to localize (R104, R700, R902) show a weak fluorescence signal in the visible. Probably by chance, the samples with low $kl^*$ (reached either by using different samples or by changing the incident wavelengths) are those where the fluorescence signal is the strongest.

Finally, the modified diffusion theory including a lifetime process (introduced in sec. 2.5.6) is able to fit all data, both ToF's and TP's, with excellent agreement. A measured lifetime of the fluorescence is used in the fits as a fixed parameter and explains the second exponential decay very well.

These results strongly suggest that all deviations from pure diffusion in the commercial "white paint" powders are caused by a weak fluorescence and do not originate from Anderson localization. Chemical analysis of the powders showed that they additionally contain carbon, implying the fluorescence to originate from organic impurities. However, the exact origin of the fluorescence is still unknown due to the low concentration of the impurities and the commercial origin of the powders.

In summary, Anderson localization of light in 3D has still not been observed yet, neither in the infrared (reported in[60], questioned in ref.[62] and refuted in ref.[64]) nor in the visible (reported in[18, 19], questioned in ref.[65] and refuted in this thesis and ref. [54]). This conclusion is also summarized in ref. [71] and conceptual problems in observing light localization are further discussed.

I will now give some insights in conceptual and experimental difficulties with no claim for completeness. Although attempts have been made with higher refractive index materials (macroporous GaP – bulk refractive index of 3.3 – [61], Ge powder – bulk refractive index of 4 – [75]), they all failed to reach the localization transition. Theoretical predictions suggest that near field effects could suppress Anderson localization of light in 3D in densely packed samples, but only the case of point scatters was considered [76]. Also, numerical simulations and experimental data explored these effects further, but so far in the diffusive regime only and neglecting positional correlations of the scatterers [24]. In a recent experimental study Naraghi and Dogariu [77] show that evanescent-field coupling might hinder wave localization via measurements of the path length distributions in strongly scattering $TiO_2$ samples varying the particle packing fraction.

Moreover, the simple picture of Anderson localization introduced in sec. 2.2.3 neglects that light is a vector wave. The effect of the polarization and the role of the transverse as well as the longitudinal component of the electromagnetic field in Anderson localization is not fully understood yet [78]. The difference between scalar and vector waves is the polarization of the light, which is scrambled in multiple scattering and thus the return probability of the photons with the same phase (and consequently the transition to Anderson localization) might be influenced.

Altogether, with the experimental observations in the latter chapter one can raise the question if this is the end of 3D Anderson localization of light? The present reasonable answer is no: it has just not been observed yet. The quest should continue with advanced high index "white paint" samples, getting rid of any fluorescent signal (or at least careful data analysis), and by increasing the scattering strength to currently unreached low $k\ell^\star$ values (either in the visible or in the IR). This might be achieved in a controlled way by tuning the scattering to resonances in photonic glass materials or as suggested by ref. [78] in hollow or coated spheres. The latter is realized by Jimenez-Villard *et al.* [79] in coated but random shaped particles solved in ethanol. But their data interpretation (claim of Anderson localization in 3D) should be handled with care due to their low scattering caused by the low refractive index contrast solution. Moreover, their data analysis uses nonphysical effective refractive index values (higher than that of the pure material index value). A detailed study of resonant light transport in photonic glasses will follow in the next chapter.

Furthermore, the role of disorder in, e.g., hyperuniform structures as studied by ref. [80] numerically, might be investigated in lower dimensional experimental systems where Anderson localization can be reached. The same systems

might be suitable for studying the role of the vector character of electromagnetic waves.

The experiments designed for observing Anderson localization in 3D mainly used static or dynamic transmission properties such as photon flight times to search for this phenomenon. Influencing one contribution of Anderson localization of light, namely constructive interference on reciprocal scattering paths, via the magneto-optical Faraday effect as discussed by myself and coworkers [81], might be a more advanced testing tool for Anderson localization in 3D. This idea will be investigated further in chapter 4 and chapter 5.

# Chapter 3

# Light transport in photonic glasses

As I showed in sec. 2.1 multiple scattering can be described as a random walk with a mean step length $\ell^\star$. In this chapter I describe a model that calculates this quantity via the single scattering cross section and by taking into account structural correlations and near field coupling in densely packed samples. First, a closer look on single scattering processes is given. Then, a possible pathway to observe Anderson localization of light in 3D in future experiments is studied by engineering the transport mean free path $\ell^\star$. Therefore, light transport in densely packed (low and high index) photonic glasses is modeled and studied experimentally to tune the scattering behavior and learn about light propagation in resonant "white paint" materials.

## Contents

# 3.1 Scattering of electromagnetic waves

Macroscopically, light scattering occurs if there is a spatial change in the index of refraction $n$. This can be due to a boundary between two materials, impurities or inhomogeneities in the medium. Depending on the size ratio of the scattering region (e.g. for a spherical scatterer, the radius $r$ divided by the wavelength $\lambda$ of the light), different single scattering regimes can be distinguished. I first introduce a simple picture of the refractive index of "dielectrics" following ref. [82, 83] before discussing the different scattering regimes.

### Refractive index

When an electromagnetic wave propagates in a medium other than vacuum, the electric field $\mathbf{E}$ disturbes the charges of the atoms. The incoming oscillating wave induces dipole oscillations of the atomic charge cloud with the same frequency $\omega$. The charges will radiate their own electromagnetic field but with a phase delay. These radiated fields will superimpose with the incoming electromagnetic wave and the superposition will be the wave propagating in the medium. This phase delay leads to a slowing down of the wave in materials with $n > 1$. The induced dipole oscillations depend on the polarizability $\alpha(\omega)$ of the specific material. The Clausius Mosotti equation gives a relation between the microscopic polarizability $\alpha(\omega)$ and the macroscopic permittivity $\epsilon$:

$$\epsilon(\omega) = 1 + \frac{3N\alpha(\omega)}{3\epsilon_0 - N\alpha(\omega)} \ , \tag{3.1}$$

with $N$ the particle number density and $\epsilon_0$ the vacuum permittivity. This simple equation illustrates already that the refractive index, which is the square root of $\epsilon$, will increase for materials with higher particle densities as for anatase and rutile phase $TiO_2$ compared to amorphous $TiO_2$.

In the next two paragraphs, I describe the two scattering processes studied in this thesis.

### Geometrical optics

Geometrical optics is the regime in which the spatial region of index variation is much larger than the wavelength of the scattered light ($r \gg \lambda$). Here the refraction is described by *Snell's Law*. For a plane incoming wave propagating in a medium with index $n_1$ and being refracted at the boundary to a media

with index of refraction $n_2$ it states:

$$n_1 \sin\alpha = n_2 \sin\beta \ , \tag{3.2}$$

with $\alpha$ and $\beta$ the angle of incidence and of refraction. This law states a dependency of the scattering angle on the refractive index.

The ratio of the reflected to the refracted light is given by the *Fresnel* equations which can be found from *Maxwell*'s equations and the continuity condition of the tangential component of the electric field **E** and the normal component of the magnetic field **B**. Here I only consider the very simplified case of normal incident light as performed in transport experiments in chapter 5. The reflection coefficient $R$ and the transmission coefficient $T$ of the amplitude of the electromagnetic waves can be expressed as follows [84]:

$$R = \frac{n_1 - n_2}{n_1 + n_2} \qquad T = \frac{2n_1}{n_1 + n_2} \ . \tag{3.3}$$

The reflectance $\rho$ and the transmission $\tau$ of the boundary, which are the corresponding intensities, can then be calculated by taking the square of the absolute value of $R$ and $T$ and dividing by the index of refraction of the medium for the incident wave $n_1$ and multiplying by the index of refraction the wave propagates in after scattering:

$$\rho = |R|^2 \cdot \frac{n_1}{n_1} = \left(\frac{n_1 - n_2}{n_1 + n_2}\right)^2 \ , \tag{3.4}$$

$$\tau = |T|^2 \cdot \frac{n_2}{n_1} = \left(\frac{2\sqrt{n_1 n_2}}{n_1 + n_2}\right)^2 \ . \tag{3.5}$$

These coefficients are used in this thesis to calculate the multiple scattering behavior through a stack of glass slides. Here one can already conclude that a high refractive index difference leads to a large reflection amplitude or in other words to strong scattering.

### Mie scattering

When the size of the scatterer is comparable to the wavelength of the scattered light ($r \approx \lambda$) one needs to solve *Maxwell*'s equations for specific scatterer geometries [85]. While for arbitrarily shaped scatterers this is analytically difficult, Mie developed an analytic solution for a plain electromagnetic wave scattered by a spherical particle [86]. The scattering cross section $\sigma_s$, which is the ratio between the intensity scattered through a surface of a sphere surrounding

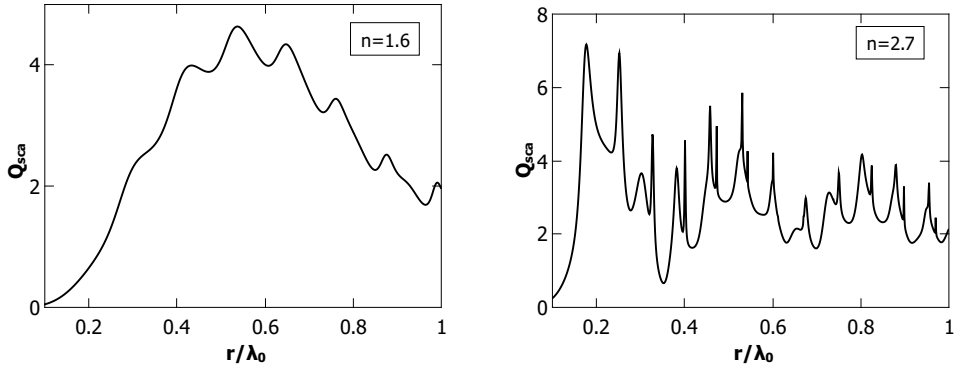


**Figure 3.1:** The scattering efficiency $Q_{\mathrm{sca}}$ of a spherical scatterer is calculated for different size parameters using the analytic expressions from ref. [85]: There resonances are called Mie resonances. Left: $n = 1.6$ (polystyrene); Right: $n = 2.7$ (rutile $TiO_2$).

the scatterer and the incident intensity, can vary strongly with the size parameter $r/\lambda$ in this solution. These so-called Mie resonances, which rise from resonant modes of the electromagnetic waves inside the scatterer, are shown in fig. 3.1 for two different refractive indices $n$ of a spherical particle with radius $r$ in vacuum ($n_0 = 1.0$). Here the scattering efficiency $Q_{\mathrm{sca}} = \sigma_{\mathrm{s}}/A$ is plotted, with $A = \pi r^2$ the particle cross-sectional area. As can be seen, the height and sharpness of the resonances increase strongly with increasing refractive index contrast. The refraction indices shown here represent typical index contrasts used in 3D scattering experiments performed in this thesis.

Mie scattering is strongly angle dependent and can lead to strongly enhanced forward scattering for spherical particles. In figure 3.2(a) the angular dependency of the scattering is shown for a Mie scatterer with radius $r = 250$ nm, a refractive index $n = 2.7$ in vacuum for a wavelength $\lambda = 590$ nm. The scattering amplitude is plotted for perpendicular and parallel polarization regarding the scattering plane. Moreover, the mean (natural polarization) is plotted. The scattering geometry is sketched in fig. 3.2(b).

The extinction cross section, which is the sum of the scattering and the absorption cross section ($\sigma_{\mathrm{ext}} = \sigma_{\mathrm{abs}} + \sigma_{\mathrm{s}}$), can be calculated by the optical theorem [85]:

$$\sigma_{\mathrm{ext}} = \frac{4\pi}{k^2} Re\left(f(\theta = 0)\right) \tag{3.6}$$

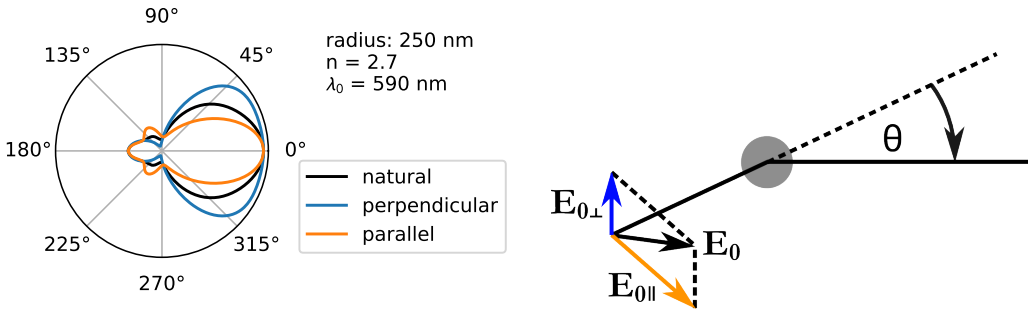


**Figure 3.2:** (a) Angular dependent Mie scattering: Normalized scattering amplitude $F(\theta)$ for perpendicular, parallel and natural polarized light (respective to the scattering plane) for a Mie scatterer with radius $r = 250$ nm, a refractive index $n = 2.7$ in vacuum for a wavelength $\lambda = 590$ nm. (b) Sketch of the scattering geometry with the incoming field $E_0$ (split into a parallel and perpendicular polarized component to the scattering plane) and the scattering angle $\theta$.

with $k = \frac{2\pi}{\lambda}$ the wave vector of the light wave and $f(\theta = 0)$ the forward scattering amplitude. The scattering cross section is then given by the angular integral over the intensity form factor $F(\theta, \phi) = |f(\theta, \phi)|^2$:

$$\sigma_s = \int_0^{2\pi} \int_0^{\pi} \frac{F(\theta, \phi)}{k^2} \sin\theta d\theta d\phi \ , \tag{3.7}$$

with $\theta$ the scattering angle and $\phi$ the angle between the laboratory coordinate system and the field coordinate system (e.g., $E_x$ and $E_\parallel$) . More explicitly for a plane wave scattered by a spherical particle the scattering cross section is given by:

$$\sigma_s = \frac{2\pi}{k^2} \sum_{l=1}^{\infty} (2l+1)(|a_l|^2 + |b_l|^2) \ , \tag{3.8}$$

with $a_l$ and $b_l$ the Mie coefficients calculated with the use of Bessel functions of first and second order. The resulting resonances (see fig. 3.1) can lead to strongly enhanced scattering for specific size ratios. If and how such resonances can survive in densely packed multiple scattering samples is part of the study in this chapter.

For particles much smaller than the wavelength of light $\lambda$, the incident plain wave can be considered to be homogeneous over the scatterers size [87] such that the scatterer can be simplified to a Hertzian dipole and scattering can be described by Rayleigh theory which is also included in the more general

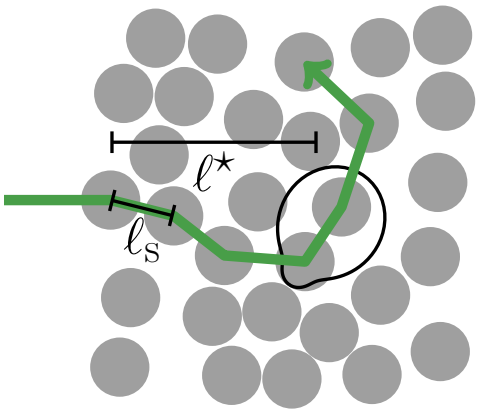


**Figure 3.3:** Sketch of the relevant length scales in a multiple scattering sample. The difference of the scattering mean free path $\ell_s$ and the transport mean free path $\ell^\star$ for Mie scatterers is shown. The Mie scattering cross section is sketched in black.

Mie-scattering solution.

## 3.2 A scattering model of photonic glasses

Let me start the description of the light transport in photonic glasses with a derivation of the mean free path $\ell$ which was already introduced as the characteristic length scale of the random walk of the photons in the multiple scattering regime. The scattering mean free path $\ell_s$, which is the path length between two scattering events (see fig. 3.3), can be expressed using the scattering cross section $\sigma_s$ and the density of scatterers $\rho_s$

$$\ell_s = \frac{1}{\rho_s \sigma_s} \, . \tag{3.9}$$

If the system size $L$ is smaller or in the order of magnitude of this length scale, the system is in the ballistic scattering or single scattering regime. For $L \gg \ell_s$ multiple scattering events take place. A detailed description of the mean free path can be found in several text books, e.g. in ref. [26].[1]

[1]The description of the transport mean free path and the effective refractive index is taken in large parts literally from a publication of myself and coworkers [88].

### 3.2.1 Transport mean free path

The photonic glasses studied in this thesis are assemblies of Mie scatterers which show an anisotropic scattering behavior (enhanced scattering probability in forward direction, see fig. 3.2(a)). The anisotropy leads to a correlation between scattering events in the direction of the photon transport. The anisotropy factor

$$\langle \cos\theta \rangle = \frac{\int \cos\theta \sigma(\theta) d\Omega}{\int \sigma(\theta) d\Omega} \tag{3.10}$$

can be used to account for this in the calculation of the mean free path. The scattering mean free path is then replaced by the transport mean free path in the random walk model

$$\ell^\star = \frac{\ell_\mathrm{s}}{1 - \langle \cos\theta \rangle} \ . \tag{3.11}$$

For isotropic scatterers, e.g., Rayleigh scatterers, the anisotropy factor is zero and the transport mean free path equals the scattering mean free path ($\ell^\star = \ell_\mathrm{s}$, see fig. 3.3).

In the case of an assembly of monodisperse spherical Mie scatterers eq. (3.11) can be written as follows:

$$\ell^\star = \frac{1}{1 - \langle \cos\theta \rangle} \frac{4\pi r^3}{3 f \sigma_\mathrm{s}} \ . \tag{3.12}$$

Here $r$ is the radius of the Mie spheres and $f$ the filling fraction of the spheres in the sample. Both the scattering cross section $\sigma_\mathrm{s}$ and the anisotropy factor $\langle \cos\theta \rangle$ of each scattering event in the multiple scattering regime can be expressed in terms of the form factor $F(\theta)$ (scattering properties of the single sphere) and the structure factor $S(\theta)$ (collective scattering of the sample) [20, 21]

$$\sigma_\mathrm{s} = \frac{\pi}{k^2} \int_0^\pi F(\theta) S(\theta) \sin\theta \, \mathrm{d}\theta, \tag{3.13}$$

$$\langle \cos\theta \rangle = \frac{\int_0^\pi \cos\theta F(\theta) S(\theta) \sin\theta \, \mathrm{d}\theta}{\int_0^\pi F(\theta) S(\theta) \sin\theta \, \mathrm{d}\theta}. \tag{3.14}$$

The intensity form factor $F(\theta)$ of a sphere is calculated by the Mie-theory [85]:

$$F(\theta) = |f_1(\theta)|^2 + |f_2(\theta)|^2 \ , \tag{3.15}$$

with the amplitude functions

$$f_1(\theta) = \sum_{n=1}^{\infty} \frac{2n+1}{n(n+1)} (a_n \pi_n(\cos\theta) + b_n \tau_n(\cos\theta)) \ , \tag{3.16}$$

$$f_2(\theta) = \sum_{n=1}^{\infty} \frac{2n+1}{n(n+1)} (b_n \pi_n(\cos\theta) + a_n \tau_n(\cos\theta)) \ . \tag{3.17}$$

Here $a_n, b_n$ are the Mie coefficients calculated with the use of Bessel functions of first and second order and $\pi_n, \tau_n$ are angle functions obtained using Legendre polynomials. If the colloids are randomly packed hard spheres, one can calculate $S(\theta)$ by using the Percus-Yevick structure factor [89]

$$S(q) = 1/(1 - n_\rho \tilde{c}(q)) \ . \tag{3.18}$$

Here $q = 2k \sin\theta/2$ with $k = 2\pi/\lambda$ and $\lambda$ the wavelength of the light in the surrounding medium. $\tilde{c}(q)$ can be calculated via the Ornstein-Zernike equation and $n_\rho = (6f)/\pi r^3$ is the number density that can be expressed via the volume fraction $f$ and the scatterer radius $r$.

Using this description, Fraden and Maret [20] were able to describe the effect of short-range correlations of the scatterers positions on multiple scattering of light in PS spherical colloids ($r = 230\,\text{nm}$) suspended in water with filling fractions up to 45% (refractive indices $n_{\text{PS}} = 1.60$ in $n_{\text{H}_2\text{O}} = 1.33$). However, when the average distance between nearest colloids is of order of the light wavelength, near field effects start to play a role in the transport properties [24]. These near-field effects are not caught in $F(\theta)$ when calculated with the bulk refractive index of the surrounding medium. Moreover, $S(q)$ depends on the surrounding refractive index via $\lambda$ as well. As I will show in the following section, the presence of other scatterers in the direct vicinity can be taken into account by defining an effective refractive index $n_{\text{eff}}$ for the surrounding medium.

This effect was not considered in ref. [20], but does not alter much that analysis because of the relatively low refractive index contrast between polystyrene and water. As will be shown in the experimental part of this thesis, a proper estimation of $n_{\text{eff}}$ is necessary when dealing with higher refractive index contrasts (like polystyrene in air, $n_0 = 1$). A first attempt to describe near-field effects was recently proposed by ref. [24], but takes into account only the fact that each scattered photon does not reach the far field limit before being rescattered, but leaves out that the surrounding medium effective index lowers the scattering compared to a freestanding scatterer in vacuum. The model pre-

sented in the following section takes into account both effects by considering that each scatterer in a densely packed random assembly is embedded in a properly estimated effective medium.

### 3.2.2 Effective refractive index

Beside the need of an effective index theory that takes into account the resonant behavior of Mie scatterers, different effective medium theories were developed in the quest of an appropriate description of transport properties in the high concentration regime in multiple scattering samples.

The energy transport velocity $v_{\mathrm{E}}$ of a wave propagating in a random medium is lowered with respect to the speed of light in vacuum, $v_{\mathrm{E}} = \frac{c}{n_{\mathrm{eff}}}$, $n_{\mathrm{eff}}$ being the effective refractive index of the complex material. For very small concentrations of scattering particles $n_{\mathrm{eff}}$ tends towards the refractive index of the matrix medium $n_{\mathrm{m}}$. If the sample is completely filled by the particle medium, $n_{\mathrm{eff}}$ converges to $n_{\mathrm{p}}$. The easiest way to define an effective refractive index which captures this behavior is

$$n_{\mathrm{eff}} = f n_{\mathrm{p}} + (1 - f) n_{\mathrm{m}}. \tag{3.19}$$

This is only valid for extreme situations of very low or very high filling fractions $f$. Advanced models have to be developed that take into account correlation effects, resonant behavior and near field coupling.

#### Maxwell Garnett refractive index

Another way to calculate the effective refractive index is the Maxwell Garnett[2] mixing formula [90]

$$n_{\mathrm{MG}} = n_m \sqrt{1 + \frac{3fK}{1 - fK}} \tag{3.20}$$

with $K = \frac{n_{\mathrm{p}}^2 - n_{\mathrm{m}}^2}{n_{\mathrm{p}}^2 + 2n_{\mathrm{m}}^2}$. The latter model is more physical than eq. (3.19) because it assumes that the polarizabilities are additive, not the refractive indices.

Nevertheless, even if the derivation of eq. (3.20) assumes the scatterers to be spherical, it completely neglects resonant scattering (the fact that energy can be stored in Mie scatterers for certain radius over wavelength ratios).

[2]Note that this refractive index theory is named after James Clerk Maxwell (prename) Garnett (surname).

### Coherent Potential Approximation

Beside the need of an effective index theory that takes into account the resonant behavior of Mie scatterers, the coherent potential approximations and its advances developed from the quest of an appropriate description of transport properties in the high concentration regime in multiple scattering samples. Earlier van Albada et al. [91] developed a theory using a Bethe-Salpeter equation that describes the energy transport velocity $v_\mathrm{E}$ very well in the regime of low $f$ consistent with experiments at $f = 0.36$. With their theory it was shown that experimentally obtained low values of the diffusion constant $D = \frac{v_\mathrm{E}\ell^\star}{3}$ can be related to low values of $v_\mathrm{E}$ due to resonant Mie scattering and a corresponding energy storage process and not to low values of $\ell^\star$ which would signify localization [22]. For high filling fractions ($f = 0.6$) experimental data is much better anticipated by advanced versions of the so called coherent potential approximation (CPA) [92].

In the "genuine" CPA [93, 94] a medium of two lossless materials consisting of spheres with radius $r$, refractive index $n_\mathrm{p}$ and a volume fraction $f$ in a host material with refractive index $n_\mathrm{m}$ is considered. Each point in the medium will be either in a region with $n_\mathrm{p}$ with a probability $f$, or in a region with $n_\mathrm{m}$ with a probability $1 - f$. The medium is modeled by spheres of radius $r$ having a refractive index given by the aforementioned probabilities. The effective refractive index is then found such that the averaged forward scattering amplitude vanishes,

$$fF_\mathrm{p}(0) + (1 - f)F_\mathrm{m}(0) = 0, \tag{3.21}$$

with $F_\mathrm{p}$ (resp. $F_\mathrm{m}$) being the differential scattering cross-section of a sphere of refractive index $n_\mathrm{p}$ (resp. $n_\mathrm{m}$) embedded in a medium having the effective refractive index $n_\mathrm{eff}$.

This approach neglects topological and geometrical differences between the scattering spheres and the host material, e.g., for high $f$ the host spheres are not only less probable but also have to have smaller radii. The real random system would be much better estimated by a mixture of coated sphere (where the scatterer with $n_\mathrm{p}$ is coated by a spherical region of host material $n_\mathrm{m}$) and of spheres (of refractive index $n_\mathrm{m}$). Equation 3.21 (this time with $F_\mathrm{p}$ the differential scattering cross-section of the coated sphere) is then solved in the same way as in the classical CPA to obtain the effective medium refractive index $n_\mathrm{CPA}$ self-consistently. In this approach the coating thickness varies with $f$. Due to the condition that the spheres should not overlap, the distribution of spacings between neighboring spheres has a peak at $r_\mathrm{c} > r$ with $r_\mathrm{c} = r/f^{1/3}$.

This advanced version of the CPA has the advantage of taking into account short range order and thus fits to experimental data quite well in the high $f$ regime [92].

### Energy Coherent Potential Approximation

In the classical CPA the energy density is homogeneous by construction. This can be violated in the coated CPA approach because of the coated sphere as the basic scattering unit. For low $f$ (large coatings) this leads to unphysical behavior near the single sphere Mie-resonaces, e.g. refractive indices smaller than 1 such that $v_{\mathrm{E}} > c$. Therefore, a new CPA approach was developed by Busch and Soukoulis [95], the so called Energy-density Coherent Potential Approximation (ECPA). Here the termination criterion for the iterative determination of the effective refractive index $n_{\mathrm{ECPA}}$ is that a homogeneous energy density $\rho_{\mathrm{E}}$ on scales larger than the basic scattering unit is reached. This approach is schematically shown in fig. 3.4.

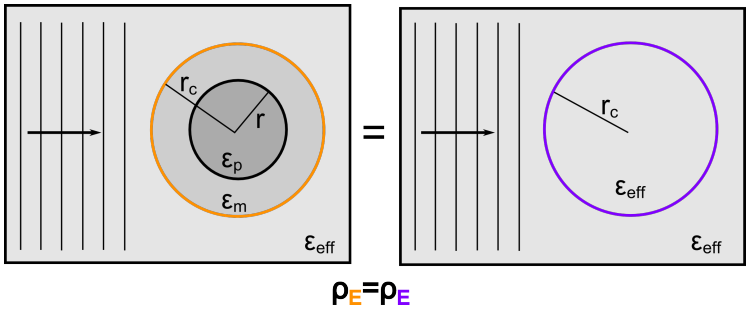


**Figure 3.4:** Energy-density Coherent Potential Approximation (ECPA) scheme: The energy density $\rho_{\mathrm{E}}$ in a scattering unit with dielectric constant $\epsilon_{\mathrm{eff}}$ has to be constant with and without coated sphere with radius $r_{\mathrm{c}}$, dielectric constant $\epsilon_{\mathrm{m}}$ of the surrounding medium in the coating and dielectric constant $\epsilon_{\mathrm{p}}$ of the particle with radius $r$.

The criterion of a constant energy density in the case of a plane wave hitting a coated sphere embedded in the effective medium versus the case where the same volume is filled by the effective medium only is quantitatively expressed in the self-consistent equation

$$\int_0^{r_{\mathrm{c}}} d^3R \rho_{\mathrm{E}}^{(1)}(\mathbf{R}) = \int_0^{r_{\mathrm{c}}} d^3R \rho_{\mathrm{E}}^{(2)}(\mathbf{R}) \ , \tag{3.22}$$

where $\rho_{\mathrm{E}}^{(1)}(\mathbf{R})$ and $\rho_{\mathrm{E}}^{(2)}(\mathbf{R})$ are the energy densities in the coated sphere and in

the same volume filled with a medium having a refractive index $n_{\text{eff}}$ respectively (see fig. 3.4). The energy density of an electromagnetic wave can be expressed as:

$$\rho_{\text{E}}(\mathbf{R}) = \frac{1}{2}\left[\epsilon(\mathbf{R})|\mathbf{E}(\mathbf{R})|^2 + \mu|\mathbf{H}(\mathbf{R})|^2\right] \ . \tag{3.23}$$

where $\epsilon$ is the dielectric constant and $\mu$ the magnetic permeability (the latter is assumed to be the same in both materials). With these equations the effective refractive index can be determined for all frequencies guaranteeing a homogeneous energy density on scales larger than the scattering unit.

Reference [95] claims that their model, which takes into account multiple scattering effects in a mean field sense, can be used for scalar (acoustic), vector (electromagnetic) and tensor (elastic) waves and is valid for all densities of scatterers. They also test it on earlier experimental data. More interesting for this thesis, this model captures the effects of resonant scattering and near-field coupling in the multiple scattering regime.

### 3.2.3 The ECPA scattering strength

In this section the Energy-density Coherent Potential Approximation (ECPA) by ref. [95] is used as an estimate for the effective refractive index to calculate the scattering strength $\lambda_0/\ell^\star$ of photonic glasses as will be studied in this chapter experimentally.

The result of this iterative calculation of the effective refractive index, as described in the previous section, is plotted in fig. 3.5(b) as a function of the size parameter and of the scatterers density for polystyrene colloids $n_{\text{PS}} = 1.6$ embedded in air $n_{\text{air}} = 1.0$. Clear resonances are seen as a function of the size parameter. One can furthermore see an increase of the refractive index with increasing filling fraction. Note that the largest $n_{\text{ECPA}}$ corresponds approximately to the index of the scattering particles ($n_{\text{PS}} = 1.6$).

Replacing the wave vector $k$ by $k_{\text{eff}} = 2\pi n_{\text{ECPA}}/\lambda_0$ in the calculation of $\sigma_{\text{s}}$ and $\langle\cos\theta\rangle$, one can calculate the scattering strength $\lambda_0/\ell^\star$ using eq. (3.12) as a function of both $r/\lambda_0$ and $f$ (see fig. 3.5(c)). Again resonances can be seen as a function of the size parameter. Note that the peaks of $\lambda_0/\ell^\star$ are placed at dips of $n_{\text{ECPA}}$. This can be understood in terms of partial index matching between the scatterers and the effective surrounding medium. It further means that high scattering strengths correspond to low $n_{\text{ECPA}}$. This should be emphasized as it is counter-intuitive to the definition of the effective refractive index via the energy velocity $v_{\text{E}} = c/n_{\text{eff}}$. It shows that effective refractive index $n_{\text{ECPA}}$ used in the calculation of the scattering cross section $\sigma_{\text{s}}$ for the static scattering property $\ell^\star$ differs from the mean effective refractive index $n_{\text{eff}}$ used to calculate

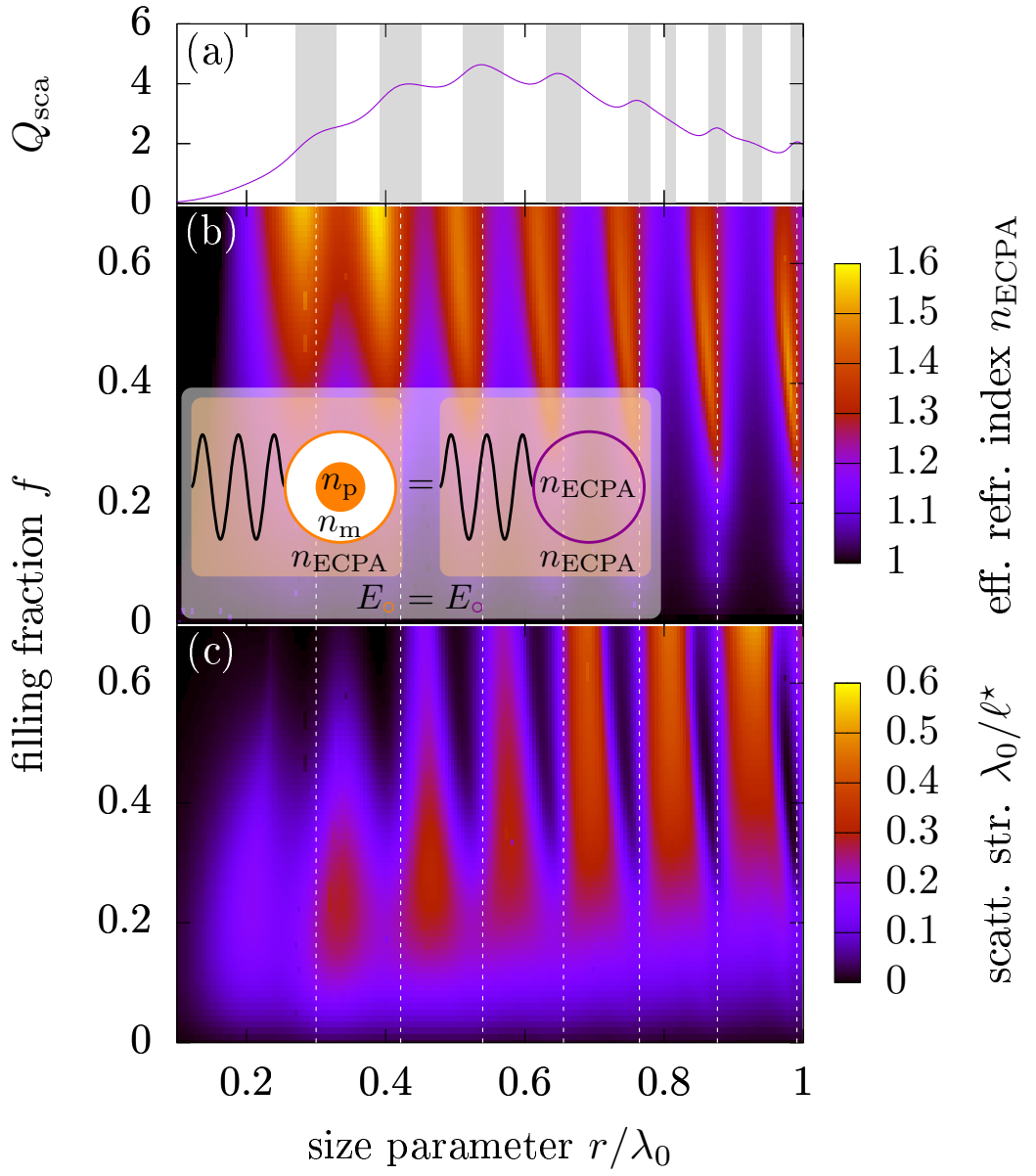


**Figure 3.5:** (a) Scattering efficiency $Q_{\mathrm{sca}}$ of an isolated Mie scatterer having a refractive index of $n_{\mathrm{PS}} = 1.6$ in air (same as fig. 3.1). The shaded regions highlight the region with negative curvature and the dashed white lines are a guide to the eye. – (b) Color map of $n_{\mathrm{ECPA}}$ calculated for a refractive index of the particle $n_{\mathrm{PS}}$ surrounded by air. Inset: principle of the ECPA – (c) Color map of the scattering strength $\lambda_0/\ell^\star$ calculated with eq. (3.12) using $n_{\mathrm{ECPA}}$. In both cases, the quantities are shown as a function of both the size parameter $r/\lambda_0$ and the filling fraction $f$. Figure same as in ref. [88].

the dynamic scattering property $v_E$. This difference is not noted in literature as the same term is often used for both indices.

Note further that the peak positions of $\lambda_0/\ell^\star$ of the multiple scattering Mie resonances differ from the single Mie resonance peaks as plotted in fig. 3.5(a) (replotted from fig. 3.1(a)). The white dashed lines are a guide to the eye for the single sphere maximum positions. The validity of the presented multiple scattering model will be tested later in this thesis experimentally and in simulations.

## 3.3 Light transport samples and setups

All commercially available $TiO_2$ powders are highly polydisperse and randomly shaped. Polydispersity and the random shape average out resonant behavior. Thus, the commercial samples used in chapter 2 are not suitable for a study of resonant transport behavior and to test the scattering model introduced in the last section. The scattering model in sec. 3.2 was developed for random assembled spherical particles all of the same size (so called photonic glasses). A description of the preparation and characterization of photonic glasses (low and high index) follows. Moreover, a spectral coherent backscattering cone (CBC) setup is introduced for small angles to test the model for the transport mean free path on relatively weak scattering but easily synthesizeable materials.

### 3.3.1 Small angle coherent backscattering

The transport mean free path $\ell^\star$ can be measured directly via the width of the coherent backscattering cone (CBC) [8, 9] as described in sec. 2.2.2. A parallel light beam illuminates the multiple scattering sample via a beamsplitter (see fig. 3.6) and the backscattered light is imaged in Fourier space on a CCD Camera (Apogee Alta U4000) placed in the focal plane of a convex lens. Most of the time a focal length of $f' = 200\,\text{mm}$ was chosen to probe as large angles as possible while ensuring the distance from the sample to the lens $d$ to be smaller than the focal length of the lens $f'$ (otherwise the CBC is superimposed on a real space image). A circular polarizer in front of the sample filters single scattered light.[3] The CCD chip has an imaging area of 230 $mm^2$ consisting of $2048 \times 2048$ pixel (px) with a 16 bit resolution. The angular resolution on the camera is given by the pixel size of 7.4 $\mu$m and the used focal length of the lens. The chip size and the limited size of the beamsplitter and the lens limits

[3] In single scattering events the helicity is flipped and filtered by the circular polarizer while multiple scattering randomizes the polarization and survives this filtering.

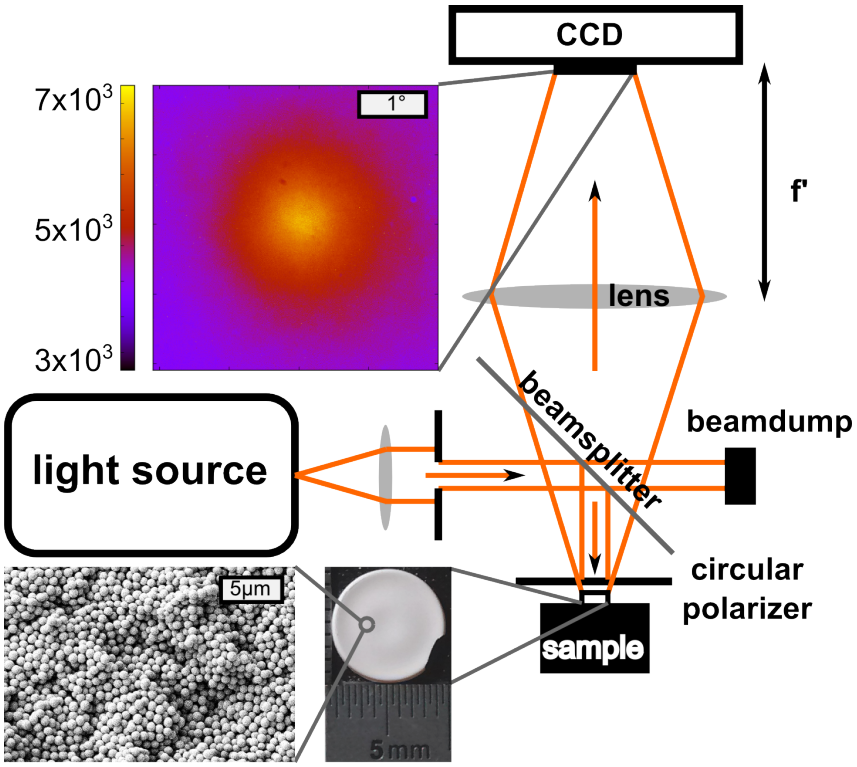


**Figure 3.6:** Scheme of the CBC setup used to measure $\ell^\star$ of multiple scattering samples: A coherent light source illuminates the sample via a 50:50 beamsplitter and a circular polarizer is used to filter single scattered light. The reflected light is imaged in the Fourier plane of a $f' = 200\,\mathrm{mm}$ lens on a CCD camera. A typical image of the cone of a PS photonic glass is shown on the left of the CCD. An image of a macroscopic PS sample is shown in the lower left with a SEM image of the same sample to its left. Figure same as in ref. [88].

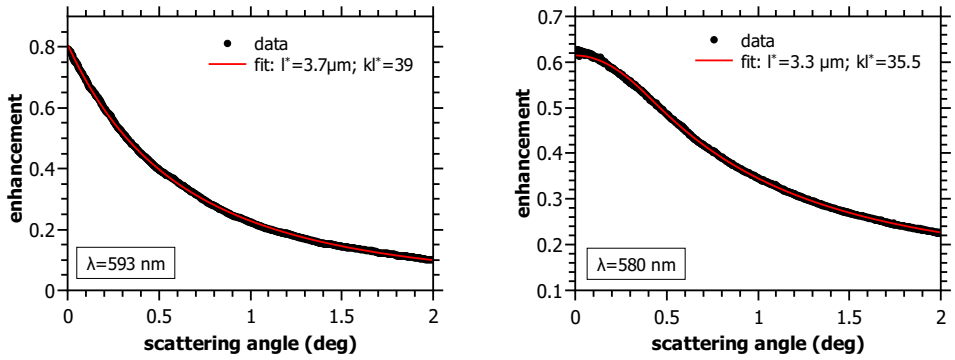


(a) laser illumination (b) LED illumination

**Figure 3.7:** Measurement data (black dots) and corresponding fits (red solid lines) of a PS photonic glass (particle radius $r = 170.5 \pm 6.0$ nm) using two different light sources (a) a coherent laser and (b) an incoherent LED measured with the setup described in this section. In (a) the standard CBC formula was used for the fit. In (b) the convolution procedure with the beam spot (see text) was applied to account for divergence.

this setup to small angles of $\approx 3°$. This is sufficient for relatively narrow cones as obtained by measuring samples with large $\ell^\star$ (in the $\mu$m range) such as the polysterene photonic glasses used later in this thesis to test the model described in sec. 3.2. The image in fig. 3.6 shows the CBC of such a PS photonic glass. When using a coherent light source and a static multiple scattering sample, the backscattered light forms a speckle pattern overlapping with the CBC. 5 images were recorded (exposure time $t_{\text{exp}} = 3\,\text{s}$) for each measurement while the sample was rotated with a motor to average this pattern out. Moreover, the saved image was averaged azimutally on concentric rings of different radii from the center of the cone tip[4] to obtain a 1D data set that can be fitted with the standard CBC formula (see eq. (2.16)). The diffusion constant $D$ and the absorption time $\tau_{\text{a}}$ were measured separately in time of flight experiments and used in the fits. The absorption length $L_{\text{a}} = \sqrt{D\tau_{\text{a}}}$ was typically in the order of the sample thickness $L \gg \ell^\star$, meaning that absorption was very low. The averaged cone data (black dots) and its fit (red solid line) from a PS photonic glass measured at $\lambda = 593$ nm can be seen in fig. 3.7(a). Here the sample was illuminated with a tunable coherent light source, namely the titanium sapphire laser coupled in the frequency doubled OPO as introduced in the latter section. This setup can be used to probe $\ell^\star$ spectrally changing the incident wavelength.

[4]The cone tip was evaluated by fitting a 2D Gaussian to the measured image.

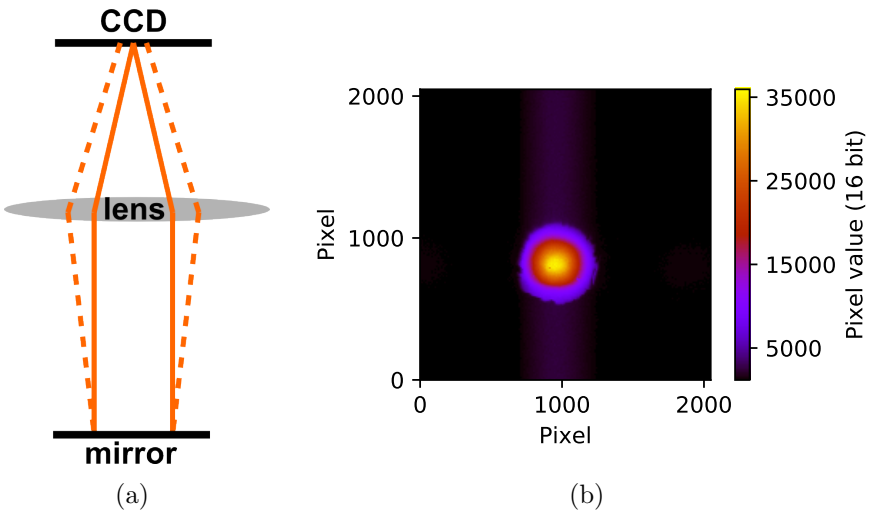


(a) (b)

**Figure 3.8:** (a) Sketch of the effect of the divergence on a focused beam (b) Measured image of the divergent spot with the LED as light source.

The laser was exchanged by a white LED (LUXEON CoB 109) coupled in a monochromator (Acton SP-2150i, Princeton Instruments) as light source to extend the spectral range. As a side effect it makes the experiment a cheap tabletop setup. The wavelength $\lambda$ can be tuned between 450-700 nm with a wavelength width of $\Delta\lambda \approx 5\,\text{nm}$.[5] Since the LED is an incoherent source, there is no need to average over speckles to measure the CBC.

Compared to a coherent laser beam the LED has a strongly divergent beam which needs to be accounted for in the analysis. The backscattered light from the sample will diverge slightly before captured by the lens and imaged in the Fourier space. This will lead to a smeared out (in angles) cone measurement. The divergence of the parallalized beam from the LED compared to a perfectly parallel beam can be measured. Therefore, the sample is replaced by a mirror. For a parallel beam this leads to a perfectly focused spot on the CCD if the setup is adjusted well. A divergent beam will lead to a wider spot reflecting the angular divergence of the light source (see fig. 3.8(a)). This spot was measured (see fig. 3.8(b)). The spot has a radius of $r \approx 1.4$ mm. For the analysis a binary image was generated with a circular spot of the same size centered around the center of the measured CBC. This calibration image was then convoluted with the CBC formula [1] as follows: A 2D image was generated from the CBC

[5]The earlier introduced white light laser coupled into the LLTF was not available at this time, but was used later for illumination as it extends the spectral range even further.

formula and transformed with a discrete cosine transform (DCT). The DCT is a similar function as a discrete Fourier transform but has the advantage to neglect redundant information when a point-symmetric image (such as a CBC) is analyzed. The calibration image was also transformed by a DCT and both functions are multiplied in Fourier space. The result is then transformed back by an inverse DCT. This function is finally used to fit the measured images of the CBC smeared out by divergence of the beam. Figure 3.7(b) shows the 1D data (black dots) and the fit (red solid line) of this fitting routine for the same PS sample as measured in fig. 3.7(a) but at $\lambda = 580$ nm. Both fitting routines work quite well and lead to reliable and reproducible $\ell^\star$ values.

### 3.3.2 Photonic glasses

If and how resonant Mie scattering can survive in densely packed monodisperse random assemblies of spheres is studied in this chapter. Therefore, custom made photonic glasses need to be synthesized. The synthesis of polysterene photonic glasses was performed by Mengdi Chen in a collaboration as published in Chen *et al.* [96]. In the following a summary with additional optical characterizations will be given.

#### Freestanding polystyrene photonic glasses

Photonic glasses are random assemblies of monodisperse spherical particles. They were introduced first by Garcia *et al.* [97, 98] as the disordered counterpart to photonic crystals. While photonic crystals undergo Bragg scattering and interesting optical phenomena such as a photonic bandgap occur [97], the disordered counterpart have not been studied intensely. In a study by the same authors they observed resonant light scattering behavior which they connect with resonant multiple Mie scattering in these materials [10, 23], but no quantitative description is given.

Synthesizing such materials is a challenging task as they need to fulfill different properties to be suitable for optical transport experiments. Firstly, the particles need to be all of the same size (monodiperse) with at least less than 5% polydispersity. Otherwise the resonant behavior smears out strongly [23]. How to obtain a large amount of such high quality particles from $TiO_2$ as needed for macroscopic sized photonic glasses is rarely reported in literature [99, 100]. Thus, a lower index material which can easily be synthesized in large amounts, namely polystyrene, was chosen in the first place. Polysterene has a refractive index of $n = 1.59$ at $\lambda = 590$ nm [101] and a density of $\rho = 1.06$ g/cm$^3$ [73]. A

detailed description of the preparation of the used freestanding PS photonic glasses can be found in ref. [96].

Letting self-assembly a stabilized solution of monodisperse spheres (where all particles are well separated) will lead to a crystalline superstructure as it is the entropically favored state. Destabilizing the particle solution during self-assembly allows these particles to come closer together and eventually form oligomers (clusters of 2, 3, 4... particles). These oligomers hinder the crystallization and a disordered superstructure can build up. Thus, disorder can be induced by reducing the stability of the particles in a charge stabilized dispersion via the addition of electrolytes. $CaCl_2$ was used for the samples measured in this thesis.

In figure 3.9(a) the effect of the amount of $CaCl_2$ on the disorder of the dried self assembled material is observed. I) shows an SEM image of a colloidal packing dried under gravitation from an aqueous monodisperse polystyrene dispersion with no addition of salt. An ordered *fcc* lattice is formed. Increasing the amount of salt to 5.3 mM $CaCl_2$ leads to a disordered arrangement as shown in II). Having a concentration of 10.7 mM even leads to a formation of voids in the material as can be seen in III). The particle diameter shown here is $d \approx 200$ nm.

A centrifugal force is applied to the dispersion to trigger the colloidal assembly. The dispersion is placed in a centrifuge tube with an additional glass insert to obtain a macroscopic flat slab shaped sample as schematically shown in fig. 3.10(a). After drying the sediment, the sample is removed and a freestanding photonic glass, as shown in fig. 3.10(b), is obtained. The obtained samples have a thickness $L \approx 1\,\text{mm}$ and a diameter $D \approx 1\,\text{cm}$. At the critical salt concentration (see II in fig. 3.9(a)) the effect of the centrifugal force on the sediment can be seen as a gradient of disorder induced by a gradient of particle concentration in the sample as shown in fig. 3.9(b) I). At the top part a crystalline structures forms, while at the bottom the sample is completely disordered. At higher salt concentration no gradient is observed and a homogeneous disordered material as shown in fig. 3.9(b) II) can be prepared.

A homogeneous material of macroscopic size is preferred to study the light transport in photonic glasses. Large voids which might appear at high salt concentrations need to be avoided as they can lower the scattering and can act as optical shortcuts where the photons can pass without being scattered. The macroscopic quality of the sample can be quantified in ToF experiments as introduced in sec. 2.3.1. If the sample is macroscopically homogeneous, the ToF follows the diffusion law from eq. (2.12). Such a measurement performed on a freestanding PS photonic glass is shown in fig. 3.11 as black solid curve. Large voids in the sample lead to optical shortcuts that appear as an early

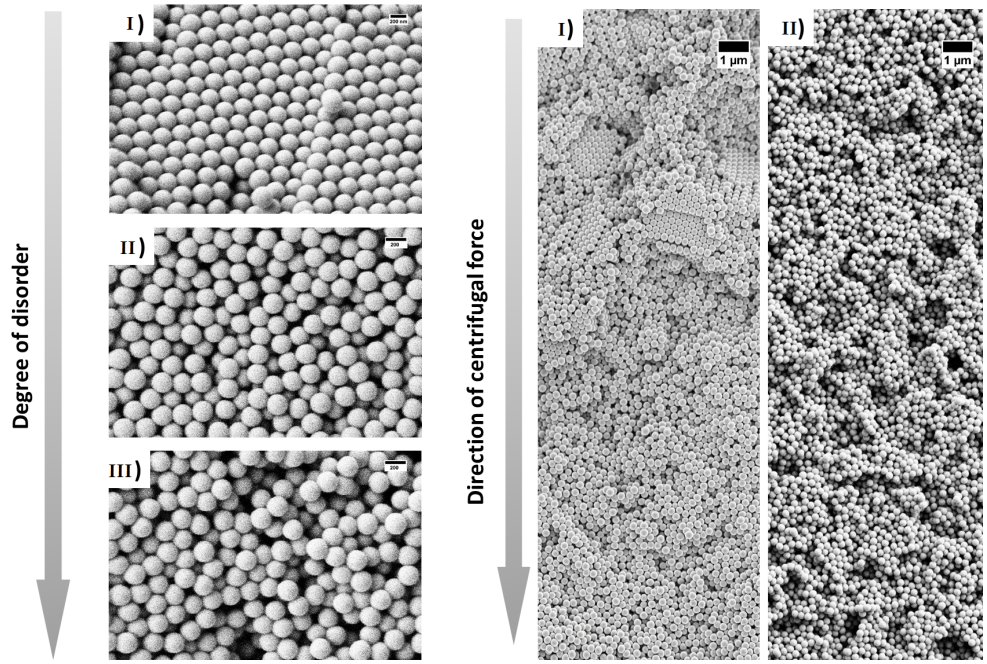


(a) (b)

**Figure 3.9:** SEM images of dried assemblies of PS spherical particles. (a) shows the effect of varying the electrolyte concentration in the solution. I) no $CaCl_2$ II) 5.3 mM $CaCl_2$ and III) 10.7 mM $CaCl_2$ is used. Scale bar: 200 nm. (b) shows the effect of the centrifugal force gradient in the sample for a sample near the critical salt concentration (5.3 mM $CaCl_2$) I) and well above the critical salt concentration (13.2 mM $CaCl_2$) II). Scale bar: 1 $\mu$m. Figure same as in ref. [96].

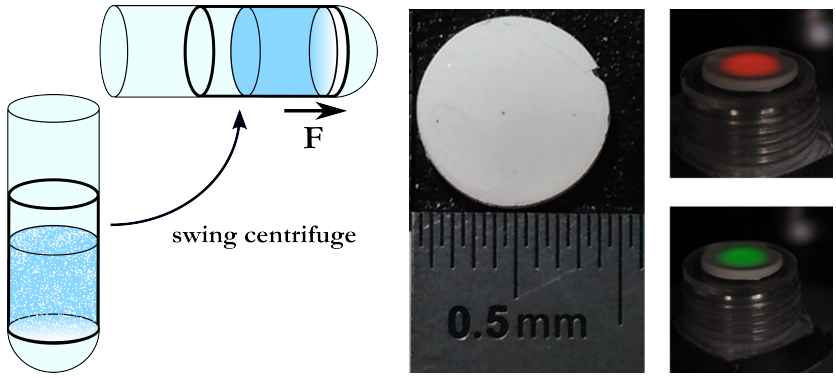


(a) (b)

**Figure 3.10:** (a) shows a scheme of the preparation of a slab shaped sample from a solution with particles: The solution in an insert in the tube is put in a centrifuge to sediment the particles by an external force. After drying, the slab shaped sample can be removed and a freestanding sample as shown in (b) is obtained.

peak in the ToF curve since photons leave the sample earlier than expected from diffusion (red dashed line). While drying the sample, cracks might also appear. In this case or in the case of very large voids most photons will pass the sample without being scattered and the detector signal equals the laser pulse reference (blue dotted curve in fig. 3.11). A co-assembly method was used to avoid such cracks and obtain a stable freestanding photonic glass. A small amount of polyacrylamide was added to the solution to have a hydrogel network that holds the particles together. The amount of hydrogel needed to be kept low so the refractive index contrast between the particles and air is only weakly affected and the scattering properties are preserved. Figure 3.12 shows SEM images of two samples prepared from the same particles but in (a) with 5 mM $CaCl_2$, which led to a dense particle packing and thus low polyacrylamide concentration between the particles. In (b) 16 mM $CaCl_2$ was used and the formation of large voids between the particles led to a relatively high polyacrylamide concentration. In fig. 3.12(b) the hydrogel fills large parts of the space between the particles. In figure 3.13 the scattering strength $\lambda_0/\ell^\star$ of the same samples is measured with the small angle CBC setup as described in sec. 3.3.1. The sample with the higher hydrogel concentration shows a lower scattering strength since the particles are optically connected. Also, the sample with low amount of hydrogel shows a wavelength dependency (feature of a resonance) that seems to be smeared out for the sample with high hydrogel concentration. While the hydrogel holds the particles together and allows for

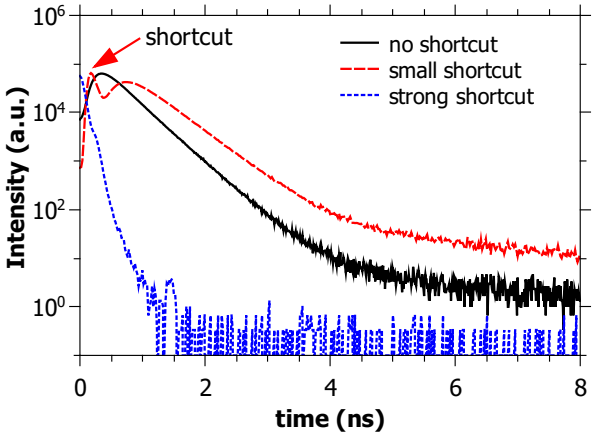


**Figure 3.11:** Time of flight measurements are shown for three different freestanding PS photonic glasses. A homogeneous sample with no optical shortcut that behaves diffusively (black solid line), a sample with voids or a small crack that shows signs of an optical shortcut as early peak in the ToF curve (ref dashed line) and a sample with a large crack where all photons pass without being scattered (blue dotted line). Figure same as in ref. [96].

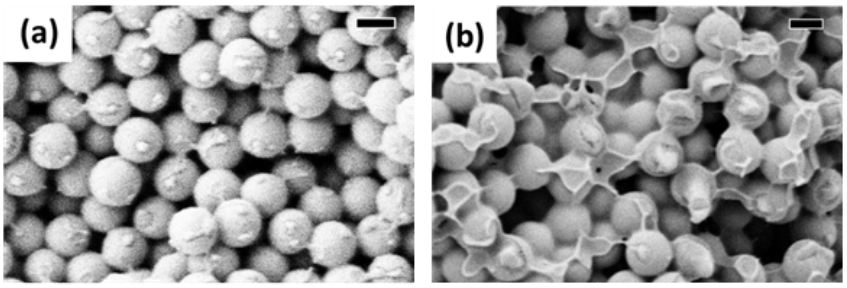


**Figure 3.12:** SEM images of assemblies of PS spheres surrounded by hydrogel to hold the particles together. (a) shows a sample prepared with 5 mM $CaCl_2$ ($\Rightarrow$ low hydrogel concentration) and (b) shows a sample made from the same particles prepared with a 16 mM $CaCl_2$ ($\Rightarrow$ high hydrogel concentration). Scale bar 200 nm.

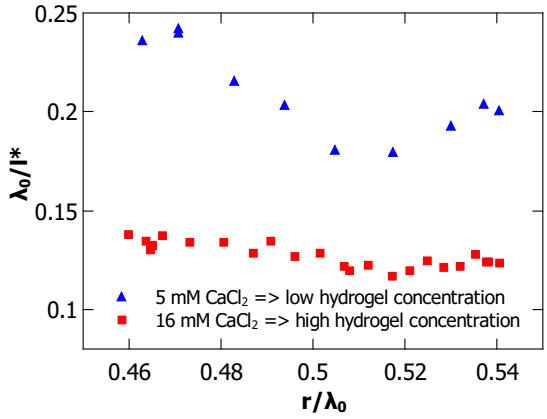


**Figure 3.13:** Spectral measurement of the scattering strength $\lambda_0/\ell^\star$ for two PS photonic glasses made from the same particles with radius $r = 298.5 \pm 5.5$ nm. One sample was prepared with 5 mM $CaCl_2$ ($\Rightarrow$ low hydrogel concentration, blue up triangles) than the other sample was prepared with a 16 mM $CaCl_2$ ($\Rightarrow$ high hydrogel concentration, red squares) as shown microscopically in fig. 3.12. The transport mean free path $\ell^\star$ is obtained from CBC measurements performed with the Ti:Sa system as spectral light source.

the preparation of a freestanding photonic glass, it also affects light transport if the concentration is too high.

An estimate of the filling fraction of the particles in the sample is needed to be able to compare the transport measurements to the ECPA scattering model. Due to the hydrogel present in the freestanding samples only an upper limit of the volume fraction can be calculated by measuring the mass and the volume of the slab shaped samples. The value obtained from these measurements is $f < 0.55$. Later when preparing such photonic glasses in the same way with high index $TiO_2$ spheres, the solid content of the particles was measured from the original solution. With this the filling fraction was evaluated to be around $f \approx 0.3$.

A wide range of $r/\lambda_0$ from 0.17 to 0.7 can be covered using the earlier introduced spectral light sources and additionally varying the particles size from $r = 125\,\text{nm}$ to $r = 335\,\text{nm}$.[6] With these samples the model of sec. 3.2.3 will be checked later in this thesis.

[6]The radii (and their errors) are obtained from the analysis of SEM images (as the one shown in fig. 3.12(a)).

### Titanium dioxide photonic glasses

As mentioned earlier the optical properties of titanium dioxide (high refractive index and low absorption) in the visible makes it an ideal material for scattering experiments. We need to prepare photonic glass made of $TiO_2$ to increase the scattering strength and show the generality of the model presented in sec. 3.2.3. Therefore, monodisperse (less than 5% polydispersity) $TiO_2$ particles with a size in the range of the wavelength or even smaller are synthesized.[7]

The difficulty is to synthesize large amounts of monodisperse $TiO_2$ and then apply the preparation of the freestanding PS photonic glasses to high index particles. While the synthesis of monodisperse PS in large quantities is well known, only few attempts can be found in literature for $TiO_2$. Different synthesis methods for monodisperse amorphous $TiO_2$ (see [99] (performed in our group) and [100]) were optimized by I. Wimmer. [102]. The educts mainly differ in the stabilization (either electrostatic (charge) stabilized or steric (polymer) stabilized) of the amorphous $TiO_2$ particles.

Eiden-Assmann *et al.* [99] show a synthesis with electrostatic stabilized particles. The advantage of this synthesis is that after preparation (drying) of the photonic glass no organic residue is left on the particles surface which could cause problems in the light scattering experiments (lowering of refractive index contrast, absorption). The salt concentration in the aqueous solution can be used to control the size of the particles in the synthesis. This synthesis was reproduced by I. Wimmer [102] and spherical amorphous particles as shown in fig. 3.14(a) were obtained. Here the particles have a mean diameter of $d = 557.2 \pm 53.4$ nm. The particles' size and standard deviation were obtained by measuring the size of 200 particles in the shown SEM image. Unfortunately these particles are quite polydisperse (11.6%). The broad distribution (see fig. 3.15(b)) and the non-perfect spherical shape hinder crystallization during self-assembly when drying these samples. Although this is an advantage when preparing freestanding photonic glasses, such that the dried powder can be pressed to slabs in the same way as the commercial $TiO_2$ powders, the polydispersity will smear out resonance behavior in optical experiments.

Therefore, a different synthesis method based on steric stabilized particles by Tanaka *et al.* [100] was optimized [102]. Again, a SEM image of the dried particles obtained from this synthesis is shown (fig. 3.15(a)). The observed self-assembly to a crystalline structure already indicates the narrow size distribution with 2.8% polydispersity (see fig. 3.15(b)). The mean diameter of the

[7] The here presented description of the preparation of high index $TiO_2$ photonic glasses summarizes the results from Ilona Wimmer, who did her master thesis on this preparation in our research group [102].

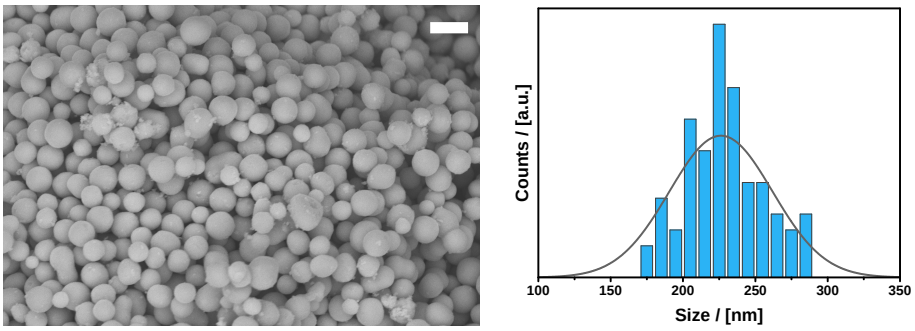


(a) SEM (b) distribution

**Figure 3.14:** (a) SEM image of static stabilized amorphous $TiO_2$ particles with $r = 228.6 \pm 26.7$ nm. Scale bar 0.5 $\mu$m. (b) Size distribution of the same particles obtained from counting 200 particles in the SEM image. Image taken from [102].

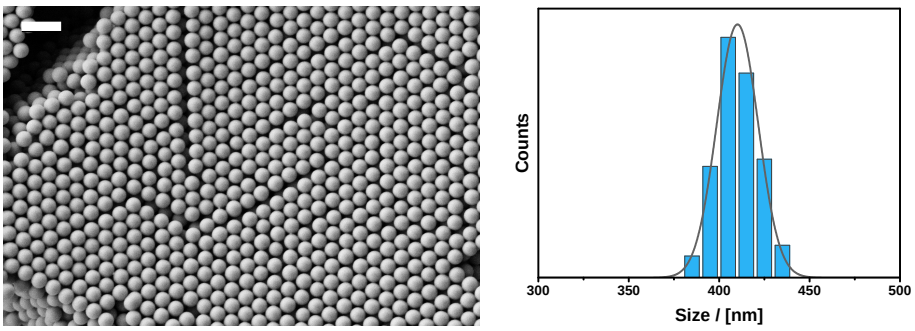


(a) SEM (b) distribution

**Figure 3.15:** (a) SEM image of steric stabilized amorphous $TiO_2$ particles with $d = 410.1 \pm 11.5$ nm. Scale bar 1 $\mu$m. (b) Size distribution of the same particles obtained from counting 200 particles in the SEM image. Image taken from [102].

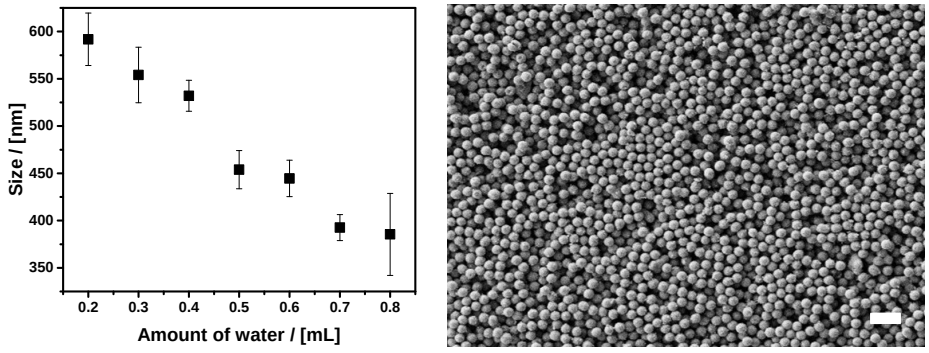


(a) (b)

**Figure 3.16:** (a) Size control of the steric stabilized $TiO_2$ particle synthesis via water concentration measured from SEM images. (b) SEM image of a pressed $TiO_2$ particle surface made from monodisperse amorphous $TiO_2$ as described by Tanaka *et al.* [100]. Scale bar 2 $\mu$m. Images taken from ref. [102].

particles is $r = 410.1 \pm 11.5$ nm. Tanaka *et al.* [100] reported a size distribution of 4%. The size can be controlled by adjusting the amount of water added to the solution [102]. With this, the particle diameter can be tuned from 390 nm to 592 nm (see fig. 3.16(a)) and thus a size ratio from $r/\lambda_0 = 0.25 - 0.63$ could be probed in the optical experiments with the available wavelengths.

Grinding and pressing these dried powders led to partly crystallized superstructures (see fig. 3.16(b)). Thus, the preparation method of freestanding photonic glasses as used by Chen *et al.* [96] for preparation of the PS samples was applied to the $TiO_2$ particle solution.

Steric stabilized particles are often still partly charge stabilized due to the surface charge of the particles. Thus, adding salt (in this case $CaCl_2$) destabilizes the solution and agglomeration occurs. Figure 3.17 shows three SEM images of the same particles, but different amounts of salt were added to the solution before drying them. As one can see from the images, already 5 mM $CaCl_2$ leads to the formation of a glass like structure, while larger voids appear with a higher concentration of salt. To avoid optical shortcuts/cracks when drying and allow the formation of a solid freestanding photonic glass, again a hydrogel network (made from polyacrylamide) was added using the earlier introduced co-assembly method [102]. Therefore, a monomer and a linker were inserted and an initiator was added before ultracentrifugation to obtain a slab shaped freestanding photonic glass as shown in fig. 3.18.

Spectral coherent backscattering experiments were carried out with the setup described in sec. 2.3.2 to study the influence of the salt added for de-

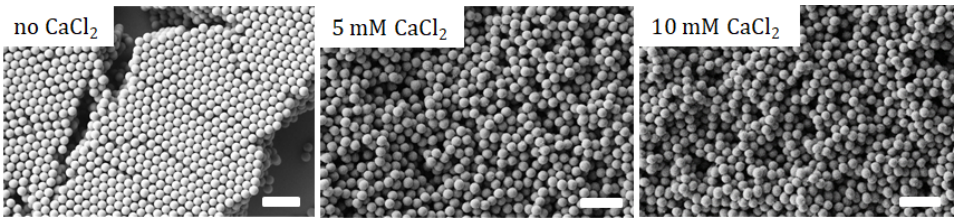


**Figure 3.17:** SEM images of dried monodisperse $TiO_2$ particles adding different amounts of salt to the particle solution before drying: a) no salt b) 5 mM c) 10 mM. Scale bar 2 $\mu$m. Images taken from [102].

**Figure 3.18:** Image of a freestanding photonic glass made of amorphous $TiO_2$ and compared to a 1 cent coin.

stabilization and the influence of the polyacrylamide network on the scattering behavior. Figure 3.19(a) shows measurements of four samples all made from the same particle solution ($d = 345.7 \pm 18.8$ nm) but using a different salt concentration for destabilization during ultracentrifugation. An optimized scattering strength is observed for a sample using 5 mM $CaCl_2$ (light blue squares). This equals the critical concentration between completely disordered and partly ordered superstructures (see fig. 3.17). Increasing the salt concentration to 7.5 mM (blue diamonds) or even 10 mM (dark blue triangles) will create voids in the sample and thus lowers the scattering. Decreasing the concentration to 2.5 mM leads to partly ordered superstructures, which also lowers the scattering strength $\lambda_0/\ell^\star$.

Two samples from two particle sizes ($d = 419 \pm 15$ nm, squares and $d = 410 \pm 12$ nm, circles) were prepared and measured spectrally as shown in fig. 3.19(b) to study the effect of the hydrogel network on $\lambda_0/\ell^\star$. The 20 wt% (closed symbols) and 40 wt% (open symbols) refer to the concentration of the monomer solution added before ultracentrifugation in the preparation process. For both particle sizes, the higher amount of monomer solution and thus the higher amount of hydrogel network decreases the scattering strength as already observed for PS in fig. 3.13. Note also that in both figures resonances are observed for the monodisperse photonic glasses. The origin of the resonances and a

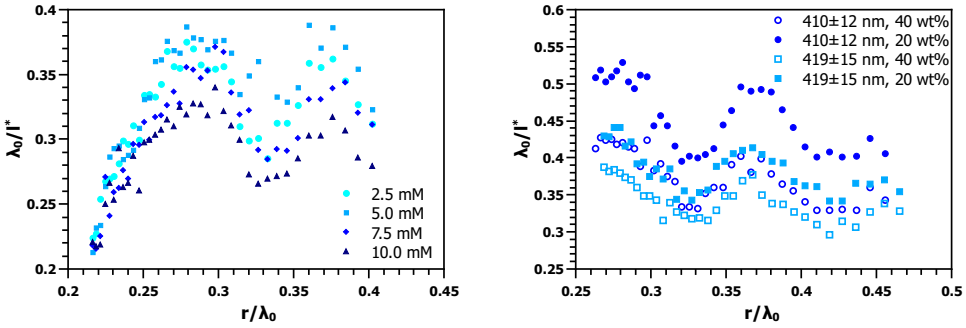


(a) (b)

**Figure 3.19:** Measured scattering strengths $\lambda_0/\ell^\star$ for (a) four samples made from the same amorphous $TiO_2$ particle solution ($d = 345.7 \pm 18.8$ nm) using different amounts of salt concentration 2.5 mM, 5 mM, 7.5 mM and 10 mM; (b) two particle sizes ($d = 419 \pm 15$ nm, squares and $d = 410 \pm 12$ nm, circles) each two samples with different monomer concentrations (20 wt%, closed symbols and 40 wt%, open symbols) in the added monomer solution before preparation.

comparison to our model from sec. 3.2.3 follows later in this thesis. Moreover, one can see that the sample with the lower polydispersity (blue circles with 2.9% compared to light blue squares with 3.6%) show a stronger scattering strength and more pronounced resonances.

Angular dependent resonances varying for different size ratios $r/\lambda_0$ are observed in the coherent backscattering cones measured on these monodisperse high index photonic glasses with the setup from sec. 2.3.2 (see fig. 3.20). Lenke *et al.* [103, 104] observed similar oscillations in the angle dependency of the CBC for suspensions of monodisperse Mie spheres. They explain this behavior by double scattering events that can be detected in the used setup and carry angular dependent information on the scattering cross section (although single scattering is filtered by the polarizer). Thus, the CBC of a monodisperse sample ($r = 430$ nm) measured at $\lambda_0 = 555$ nm is plotted in fig. 3.20(a) and compared to the differential scattering cross section $d\sigma$ for different sized Mie scatterers. The expected size fits the resonance position quite well. At small angles this quantity decreases to zero for the helicity conserving channel, such that the normal CBC fit (eq. (2.16)) can be fitted for these angles (red solid line). Adding the differential cross section $d\sigma$ with a free parameter for the amplitude as an additional term in the fit of the CBC allows to extract the particle size from this measurement as shown in fig. 3.20(b) for a monodisperse photonic glass ($r = 265 \pm 10$ nm) measured at $\lambda_0 = 550$ nm.

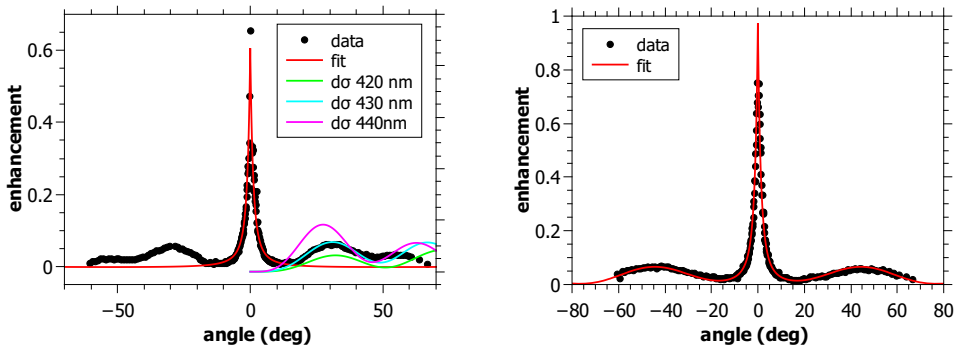


(a) (b)

**Figure 3.20:** (a) CBC measurement of a sample with size $r = 430$ nm at $\lambda_0 = 555$ $nm$ and the corresponding fit (eq. (2.16), red line) done for small angles up to 12° compared to the differential cross section d$\sigma$ of a single Mie sphere for three particle radii. (b) CBC measurement of a sample with size $r = 265 \pm 10$ nm at $\lambda_0 = 550$ $nm$ and the fit (red line) including d$\sigma$.

Synthesizing $TiO_2$ as described in ref. [102] leads to the formation of an amorphous phase. Due to their higher atomic densities the crystalline phases of $TiO_2$ have a higher refractive index and thus stronger scattering is expected. Heat treatment allows for the conversion of amorphous to anatase and at higher temperature to rutile phase $TiO_2$. Figure 3.21 shows SEM images of the same $TiO_2$ particles sintered at different temperatures $T = 400$ °C, $T = 500$ °C, $T = 600$ °C, $T = 700$ °C, $T = 800$ °C, and $T = 900$ °C for 1 h. In figure 3.22 corresponding powder x-ray diffraction (PXRD) measurements are shown. Below 400 °C the amorphous phase is preserved (no peaks occur). At $T = 400$ °C a transformation to anatase took place and only anatase peaks can be observed (red reference peaks at the bottom). Here the particle shape is preserved as can be seen in the SEM image. Note that the size of these particles already shrunk from $d = 410$ nm to $d = 317$ nm keeping the small size distribution. At higher temperatures rutile peaks occur and from $T = 600$ °C a pure rutile phase is observed in the PXRD measurements (see fig. 3.22(b).) While in the mix phase at $T = 500$ °C the particles shape is still kept as seen from fig. 3.21, for higher temperatures a polycrystalline structure becomes visible as measured by I. Wimmer [102]. At $T = 700$ °C particles start to melt together which optically connects the particles and lowers light scattering. Thus, in the performed scattering experiments the samples were heated to $T = 400$ °C to obtain pure anatase phase $TiO_2$ particles and preserve

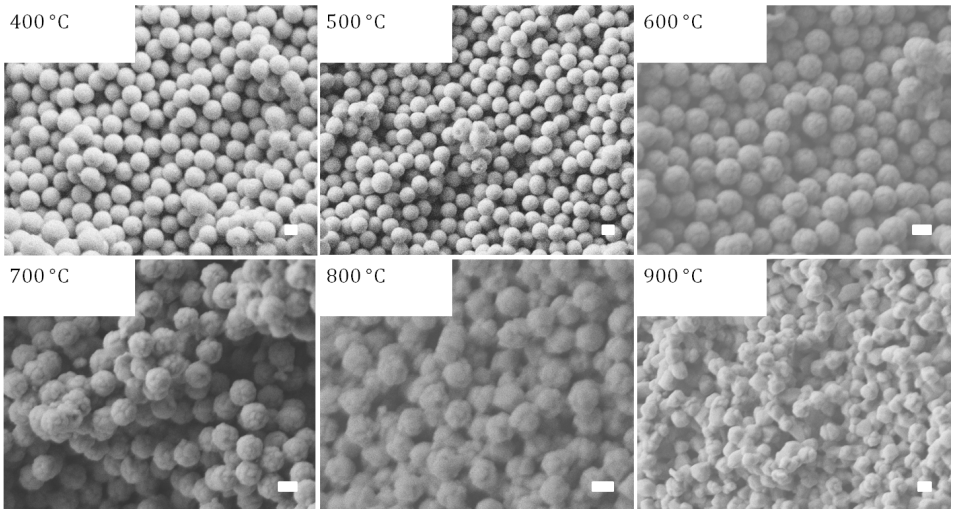


**Figure 3.21:** SEM images of $TiO_2$ particles heated to the specified temperatures for $t = 1$ h. Scale bar 200 nm. Images taken from [102].

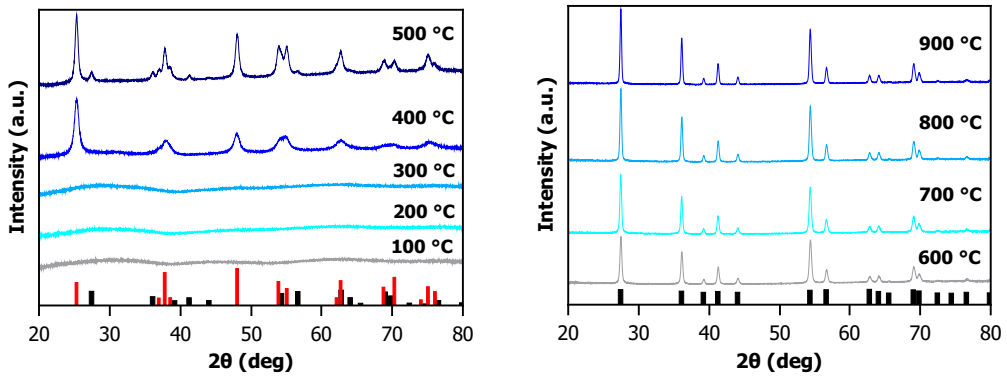


(a) (b)

**Figure 3.22:** PXRD measurements of the same $TiO_2$ particles as shown in fig. 3.21 sintered at (a) 100 °C, 200 °C, 300 °C, 400 °C and 500 °C (b) 600 °C, 700 °C, 800 °C and 900 °C for 1 h. In (a) red bars indicate anatase phase reflexes, black bars indicate rutile phase reflexes. In (b) black bars indicate rutile phase reflexes. Same data as in ref. [102].

the particles' shape and monodispersity. After heat treatment and redispersion the same co-assembly method as used for the amorphous $TiO_2$ particles was applied to obtain freestanding anatase photonic glasses.

## 3.4 Engineering the scattering strength in photonic glasses

In the earlier introduced scattering experiments the samples were prepared using commercial "white paint" materials of random scatterer shape and size with high polydispersity. Controlling the shape and size of the particles and lowering the polydispersity, one might be able to tune the scattering to Mie-resonances of the scatterers and thus obtain strong scattering for certain frequency windows. Such photonic glasses were introduced by Garcia *et al.* [23, 98] and as mentioned earlier they observed Mie resonant behavior in the multiple scattering in relatively low index glasses made of polystyrene spheres. But all attempts to describe these resonances more than qualitatively failed [10, 105, 106].

In this section light transport in photonic glasses is predicted by the model of the transport mean free path $\ell^\star$ introduced in sec. 3.2, which uses the ECPA effective refractive index to account for near field coupling while taking structural correlations into account. The model will be tested against *ab initio* numerical simulations, earlier experimental data obtained from transmission experiments [23], and new experimental results from backscattering experiments (using the CBC setup as described in sec. 3.3.1) on specially synthesized polystyrene colloidal glasses [96] (as described in the latter section 3.3.2).[8] Later the model will be tested on high refractive index photonic glasses made of amorphous and anatase $TiO_2$ (described in sec. 3.3.2) and these advanced "white paints" will be compared to the commercial "white paint" materials.

### 3.4.1 Numerical simulations

Figure 3.23(a) shows the scattering strength $\lambda_0/\ell^\star$ as calculated by the ECPA scattering model in sec. 3.2.3 for a polysterene photonic glass ($n = 1.6$) in air and a given filling fraction ($f = 0.5$, red solid curve) and compares it to the one expected taking a given polydispersity of the spheres into account (dash-dotted red curve). As expected, the resonances are somewhat smeared out.

[8]This section about numerical simulations and experimental tests in PS photonic glasses is taken in large parts from a publication of myself and coworkers [88].

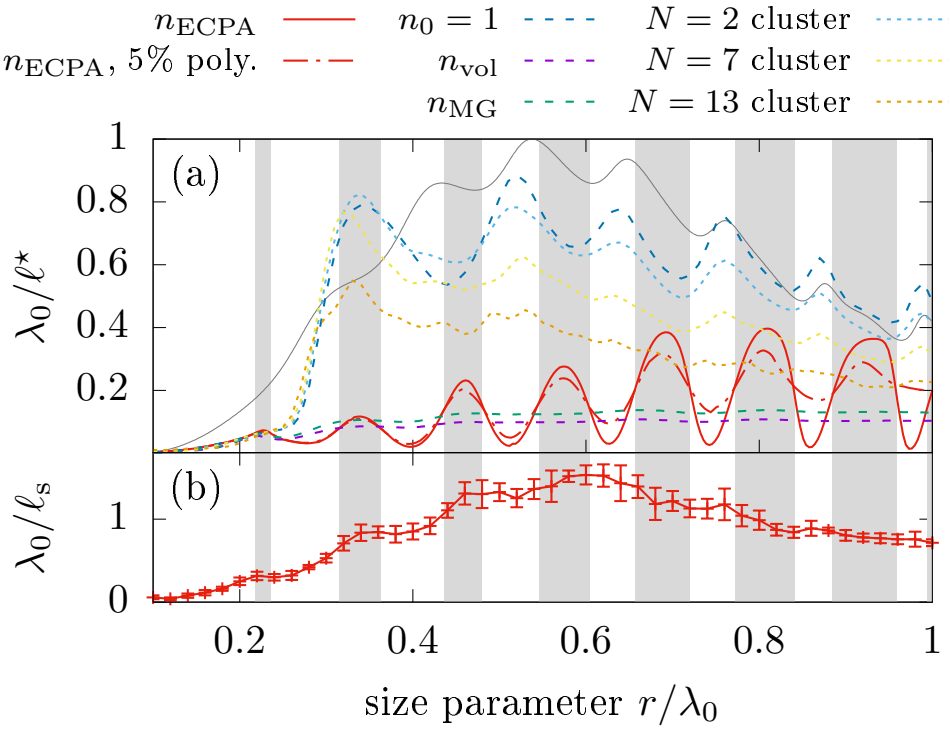


**Figure 3.23:** (a) Scattering strength $\lambda_0/\ell^\star$ calculated with different models for a filling fraction $f = 0.5$ (red curves: using $n_{\mathrm{ECPA}}$ (solid: monodisperse, dot dashed: 5% polydispersity) the shaded regions highlight negative curvature of the solid red curve; dashed curves: simple model for $n_{\mathrm{eff}}$ (see text); dotted curves: calculated with the differential cross section of the $N$ cluster). The single sphere scattering efficiency (also plotted in fig. 3.5(a) is shown for comparison in gray (arbitrary units). – (b) Averaged $\lambda_0/\ell_{\mathrm{s}}$ calculated with the MSTM code over five realizations of numerical photonic glasses, each one having $f = 0.5$. Figure taken from Aubry and Schertel *et al.* [88].

For larger size ratio the effect of polydispersity becomes stronger as it is fixed by the particle size and the relative effect on the wavelength becomes larger. Moreover, a larger size ratio is associated with higher order Mie resonances where small particle size deviations add up in multiple "cavity" roundtrip modes.

To emphasize the claim that a proper choice of $n_{\text{eff}}$ is necessary for the calculation of the transport properties of dense high index photonic glasses, the difference between the scattering strength calculated using $n_{\text{ECPA}}$ (red solid curve in fig. 3.23) and the one calculated using a simpler model (violet)

$$n_{\text{vol}} = f \cdot n_{\text{PS}} + (1 - f) \cdot n_0 \tag{3.24}$$

and $n_{\text{MG}}$ for the Maxwell Garnett effective refractive index [90] (green), as described in sec. 3.2.2, is also shown in fig. 3.23(a). The simple models lead to no resonant behavior in $n$, but the order of magnitude of the scattering strength agrees more with the $n_{\text{ECPA}}$ predictions than the curve calculated without using any effective refractive index (blue dashed curve).

More advanced numerical simulations were performed by G. J. Aubry and will be described in the following for completeness. Another way to take the presence of other scatterers in the direct vicinity of each scatterer into account for its scattering properties is to calculate directly the differential scattering cross section $F(\theta)$ for a scatterer surrounded by other scatterers (as suggested by [23]). Therefore, the average over all possible orientations of $F_N(\theta, d_{\text{NN}}(f))$ of clusters of $N = 2$, 7, or 13 particles made of one sphere having $N - 1$ neighboring spheres placed at the average nearest-neighbor distance in the glass $d_{\text{NN}}$ (which is a function of $f$ [107]) is calculated numerically by G. J. Aubry using the Multiple Sphere T Matrix (MSTM) code [108]. Then $F(\theta)$ was replaced by $F_N(\theta, d_{\text{NN}}(f))/N$ in eqs. (3.13) and (3.14) *without* using an effective refractive index. By doing this, near-field effects in the scattering properties are taken into account in a similar way as in ref. [24]. As shown by the dotted curves in fig. 3.23(a), the scattering strength decreases with the number of nearest neighbors indicating stronger near-field effects, but is still very different than the one predicted using $n_{\text{ECPA}}$.

To test the model using $n_{\text{ECPA}}$ (red solid line in fig. 3.23(a)), the transmission trough thin slabs (6.25 times the radius of the spheres) of monodisperse spheres are simulated using the Multiple Sphere T Matrix code [108]. In the simulation of fig. 3.23(b) the transmission of the nonscattered field is calculated and the *scattering* mean free path $\ell_{\text{s}}$ is extracted from this quantity.

The scattering geometry is shown in fig. 3.24: cylindrical slabs having a diameter of 10000 nm, a thickness of $L = 1000$ nm containing about 2270

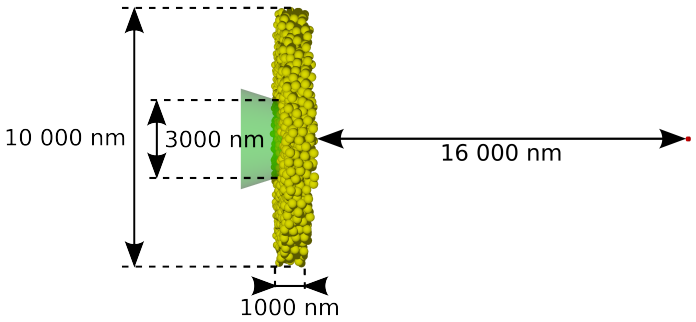


**Figure 3.24:** MSTM geometry: a Gaussian beam is focussed on one side of the sample, and the intensity is calculated in the far field on the red spot (see text for details). The figure is at scale. Figure taken from Aubry and Schertel *et al.* [88].

particles with a radius $r = 160\,\mathrm{nm}$ (filling fraction of 50%) were created. Five samples were created by using the Force Biased Algorithm code of Baranau and Tallarek [109] to average on sample configurations.

A Gaussian beam (wavelength $\lambda_0$ between 160 and 1600 nm) was focused on one side of the slab (waist $w_0 = 1500\,\mathrm{nm}$), and $I = \langle E^2 \rangle$ —the integral of the intensity on a circle of radius 100 nm placed at a distance of 16000 nm on the other side of the sample (ten times the largest wavelength to get rid of any evanescent wave present close to the spheres)— was calculated.[9] The influence of the target size is shown in fig. 3.25. The smallest shown target size was used as here mostly ballistic photons arrive. The same calculation without any scatterers ($I_0 = \langle {E_0}^2 \rangle$) was done as a reference calculus. The samples are optically thin ($\lambda_0/L$ ranges from 0.16 to 1.6). Therefore, most of the photons are expected to be scattered only once. In this regime the coherent part of the beam $I_\mathrm{c}$ (i.e. the part of the wave which is not scattered) is attenuated exponentially

$$I_\mathrm{c} = I_0 \cdot \exp\left(-\frac{L}{\ell_\mathrm{s}}\right), \tag{3.25}$$

where $I_0$ is the incident intensity and $\ell_\mathrm{s}$ is the *scattering* mean free path. By integrating the intensity on a small surface at such a large distance on such a thin sample, the major part of it corresponds to the coherent intensity, therefore $I \simeq I_\mathrm{c}$. This allows us to calculate $\ell_\mathrm{s}$ using eq. (3.25).

[9] Five different glass configurations were calculated on the Scientific Compute Cluster (Universität Konstanz) using between 10 and 20 processors for computing time ranging from a few hours to a few days depending on the wavelength.

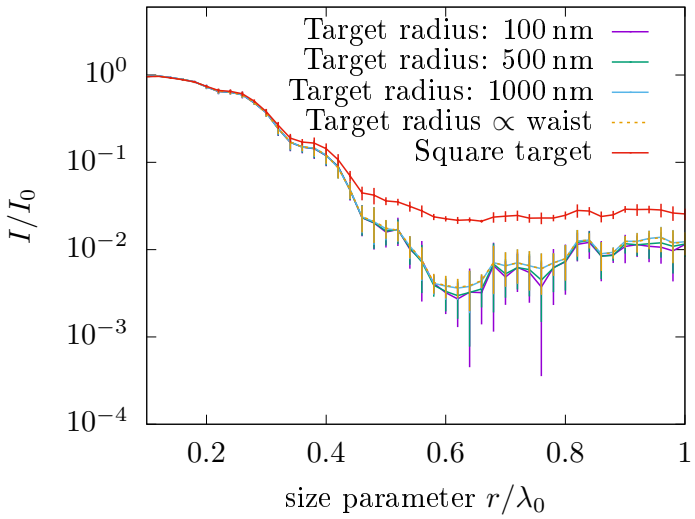


**Figure 3.25:** Average over five different slabs of the MSTM calculated transmission as a function of the size parameter: influence of the target size on the transmission values. The target is either circular (violet, green, blue and yellow lower curves) or square (red upper curve, square area $10640^2\,\mathrm{nm}^2$). Away from the focus, the width of a Gaussian beam depends on the wavelength: the yellow dashed curve was calculated by taking the radius of the target such that $I_0(r) > I_0(0)/2$. All error bars correspond to the standard deviation. Figure taken from Aubry and Schertel *et al.* [88].

As expected, the so-extracted $\ell_s$ are smaller than the $\ell^\star$ predicted by our model. Moreover, one can recognize in fig. 3.23 the same resonant behavior between $\ell_s$ and $\ell^\star$, at least for $r/\lambda_0 \lesssim 0.7$. For larger ones, the resonances seems to be smeared out (in this range, the overall transmissions fall in the $10^{-3}$ range, making it difficult to extract the coherent beam without any scattered contribution).

### 3.4.2 Experimental test on polysterene photonic glasses

The transport mean free path $\ell^\star$ of PS photonic glasses is measured for different size parameters $r/\lambda_0$ in a range from 0.17 to 0.7 to test the ECPA scattering model experimentally. The transport mean free path $\ell^\star$ is extracted by analyzing the shape of CBC as described in sec. 3.3.1 for different incident wavelengths. The width of the CBC is inversely proportional to $k\ell^\star$.

The samples are free standing PS photonic glasses as described in sec. 3.3.2. A wavelength scan of the scattering strength of five PS photonic glasses with different radii varying from $r = 125$ (dark blue, left triangles) to $r = 335\,\text{nm}$ (blue, diamonds) is shown in fig. 3.26 using the CBC setup with the LED and monochromator as tunable light source. This measurement reveals the first direct observation of strong resonances of $\lambda_0/\ell^\star$ in the visible. For comparison a randomly shaped and highly polydisperse sample of chalk powder (black diamonds) is measured (for this sample $r = 335\,\text{nm}$ was set arbitrarily) and, as expected, no resonant behavior is observed in this case. An SEM image of the chalk sample is shown in fig. 3.27. Comparing the data with the predictions of the scattering model (eq. (3.12) using $n_{\text{ECPA}}$) for different filling fractions (solid lines), the data recovers the theory for a filling fraction of $f = 0.3$ (grey solid line) in the best way. This can be seen better from fig. 3.28. Such a filling fraction was already predicted in sec. 3.3.2.

The experimental data show that the positions of the resonances are very well predicted when the transport properties are calculated using the ECPA effective refractive index (see the comparison between the scattering strengths and resonance positions predicted by different models in fig. 3.23). The amplitudes of the resonances are slightly smeared out compared to the model. This can partially be understood because of the residual polydispersity of the particles and of the wavelength width of the source (see also dashed dotted red line in fig. 3.23). To further test the model the data of fig. 19 of ref. [23] is plotted (red diamonds). They measured $\ell^\star$ via diffuse transmission measurements in the infrared with polystyrene particles of $r = 610\,\text{nm}$. The model presented in this thesis recovers the position of their resonances very well. The lower amplitude of the measured resonances compared with the model could

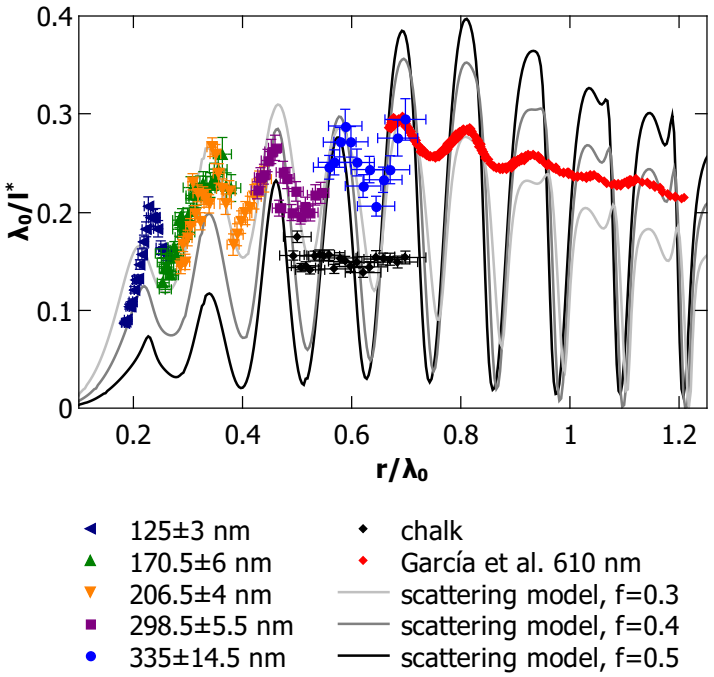


**Figure 3.26:** Measured scattering strength (using the LED setup) of five monodisperse polystyrene photonic glasses from $r = 125$ to 335 nm compared to a chalk sample (irregular particle shape, for this sample we arbitrarily set $r = 335$ nm). The errors in $\ell^\star$ are estimated from the fits to be $\pm 0.1\,\mu$m. The data are compared with the predictions of the scattering model (eq. (3.12) using $n_{\mathrm{ECPA}}$) for different filling fractions (solid lines) and with the transmission data extracted from [23] ($r = 610$ nm). Figure taken from Aubry and Schertel *et al.* [88].


**Figure 3.27:** SEM image of a chalk sample of random shape and size. The sample was used as reference. Scale bar: 1 $\mu$m

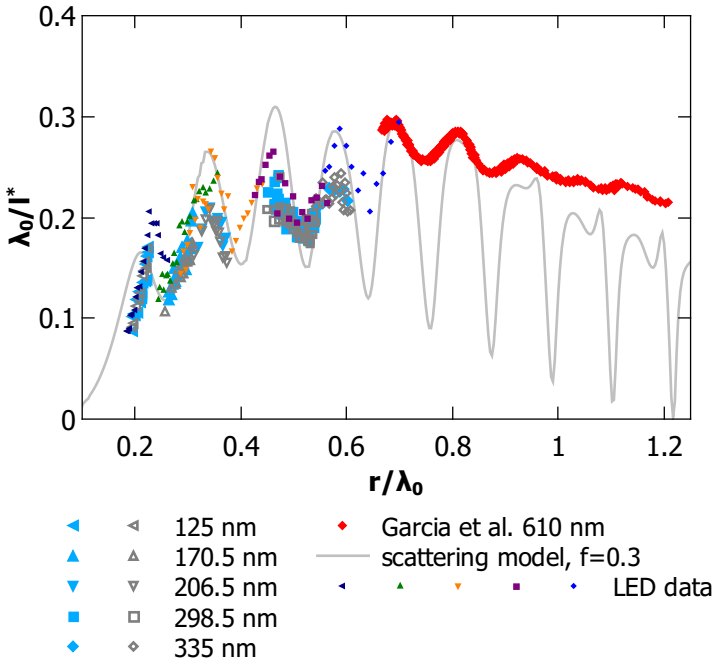


**Figure 3.28:** Measured scattering strength of five monodisperse polystyrene photonic glasses from $r = 125$ to 335 nm. The data was measured using different light sources: A tunable laser system (Ti:Sa and OPO) shown as filled light blue symbols and open gray symbols and a LED followed by a monochromator (small symbols, same data as in fig. 3.26). The data are compared with the predictions of the scattering model (eq. (3.12) using $n_{\mathrm{ECPA}}$) for a filling fraction of $f = 0.3$ (light grey solid line) and with the transmission data extracted from ref. [23] ($r = 610$ nm).

be explained by the polydispersity of their sample, but no such information is given in the paper.

The LED data (shown in fig. 3.26) is further compared in fig. 3.28 to data obtained using the Ti:Sa followed by the OPO as tunable light source. This data is measured twice (filled light blue and open grey symbols) to check for reproducibility. The datasets are quite well reproducible and moreover the LED and the laser measurements overlay. The LED has a larger wavelength range and thus allows for a continuous scan of the resonances. The measurements are again compared to the data of fig. 19 of ref. [23]. All these six different data sets collapse on the same curve and cover the first nine Mie resonances versus $r/\lambda_0$, and this without any fit parameter.

Together, the experimental and the numerical test show the importance of an appropriate model for $n_{\text{eff}}$ in the description of the transport properties of dense photonic materials where near-field coupling influences scattering behavior. The shell introduced in the definition of $n_{\text{ECPA}}$ is the key to take near-field effects into account. It has a thickness which is related to the average particle distance in the glass, and couples electromagnetically each scatterer with the surrounding medium. Unlike all other models used so far, the ECPA model seems to predict very well the resonant behavior in photonic glasses without any fit parameter.

### Energy transport velocity

As mentioned in sec. 2.1.1 a measurement of the scattering strength is a measurement of the static scattering property $\ell^\star$ only. One has to measure the diffusion constant $D$ via ToF measurements to learn about the dynamic scattering via a measurement of the energy velocity $v_{\text{E}}$ of the electromagnetic wave in a multiple scattering sample. How $v_{\text{E}}$ is effected by resonant scattering and which of these two quantities ($v_{\text{E}}$ and $\ell^\star$) dominates $D$ is not fully exploited in the literature.

Figure 3.29 shows a spectral ToF measurement of a PS photonic glass ($r = 125$ nm) measured with the setup described in sec. 2.3.1. The tail of the ToF curve becomes longer for smaller wavelengths.[10] Also the maximum of the ToF curve which is inversely proportional to the diffusion constant $D$ for low absorption shifts to larger values for smaller wavelengths. Fitting these curves with eq. (2.12) let us extract $D$ for each wavelength as plotted in fig. 3.30(a) versus the size parameter. The diffusion constant lowers with larger size para-

[10]Note here that a fluorescent tail for very long times is observed similar to sec. 2.5.2. This tail disappeared when using a bandpass filter on the incident wavelength. It might come from a fluorescent signal of the polymeric network holding the particles together.

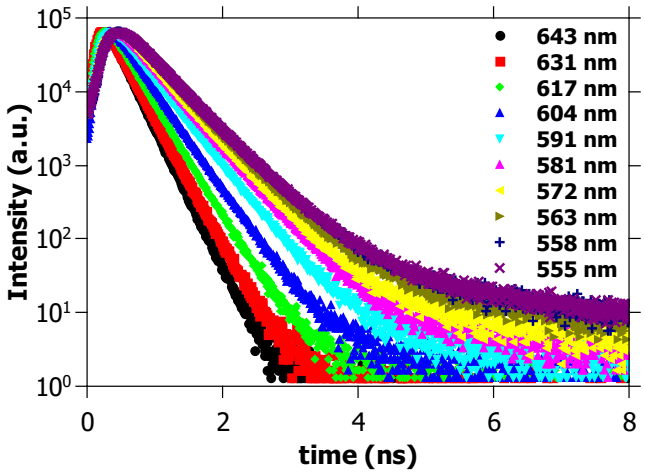


**Figure 3.29:** Spectral time of flight of a PS photonic glass with $r = 125$ nm and $L = 1.1$ mm. The different ToF curves were measured at different wavelength using a setup as described in sec. 2.3.1.

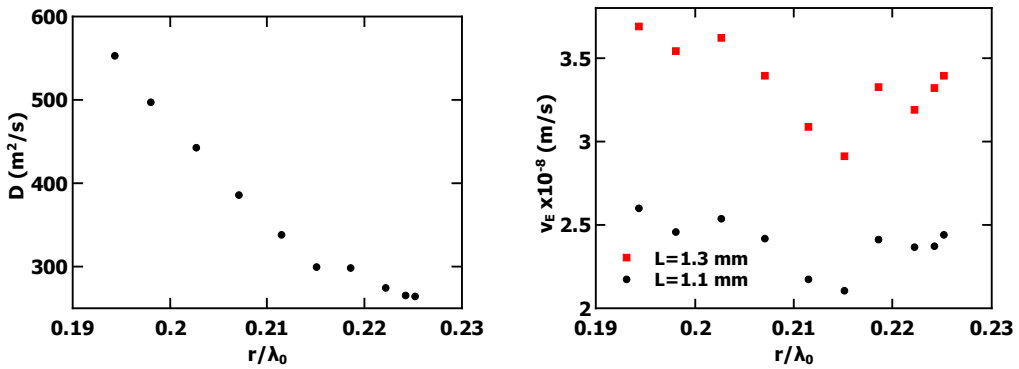


(a) (b)

**Figure 3.30:** Spectral measurements of (a) the diffusion constant $D$ and (b) the energy velocity $v_E$ plotted against the size parameter $r/\lambda_0$. The sample was a PS photonic glass with particle radius $r = 125$ nm and sample thickness $L = 1.1$ mm (black circles). The sensitivity to the thickness is shown in (b) by showing the same analysis using a different measured thickness $L = 1.3$ mm (red squares).

meter for this sample while the scattering strength is growing (see fig. 3.28). This recovers the fact that $D \propto \ell^\star$. The energy velocity $v_\mathrm{E} = 3D/\ell^\star$ can now be extracted (see black circles in fig. 3.30(b)). It seems to be constant with no clear resonant behavior, but quite noisy. The mean value ($v_\mathrm{E} \approx 2.5 \times 10^8$ m/s) is well approximated by $v_\mathrm{E} = c/n_\mathrm{MG} \approx 2.6 \times 10^8$ m/s for $f = 0.3$. Note that the analysis procedure is very sensitive to the value of the thickness of the sample. Here a thickness of $L = 1.1$ mm was used. The thickness of the freestanding photonic glasses is measured with a micrometer screw. Due to the non-perfect surface of the photonic glasses the thickness can locally vary very strongly. At another surface position a thickness of $L = 1.3$ mm was obtained. The energy velocity obtained in this case is shown in fig. 3.30(b) in red, but leads to non-physical results larger than the speed of light $v_\mathrm{E} > c$.

Moreover, the sample used for the shown measurement was the one with the best overall sample quality, meaning it was very homogeneous and had a relatively flat surface and no optical shortcuts. Optical shortcuts as well as a bad sample surface quality (such that no reliable thickness $L$ can be extracted) hinders to apply the aforementioned analysis procedure. Additionally, the low refractive index of PS and the connected short photon flight times requires very thick homogeneous photonic glasses which are difficult to prepare. Thus, no scan over the whole size parameter range was possible with the available samples. In addition, high index glasses in which longer photons flight times and stronger resonant behavior is expected, seem more suitable for such a study.

### 3.4.3 High refractive index photonic glasses

The resonant behavior in polymeric photonic glasses leads to strong scattering at certain $r/\lambda_0$ values. Increasing the refractive index contrast by using higher index materials such as $TiO_2$ spheres in air will lead to much stronger resonant behavior. This can be seen in fig. 3.31. Here the ECPA scattering strength is plotted at a filling fraction of $f = 0.5$ for four different colloid refractive indices: $n = 1.6$ (corresponding to polystyrene), $n = 2.0$ (amorphous $TiO_2$, lower limit), $n = 2.5$ (anatase $TiO_2$) and $n = 2.7$ (rutile $TiO_2$). With increasing index the resonances become higher, sharper and shift to smaller size parameters. The shift disappears when the scattering strength is plotted against the relative size ratio $r \cdot n_x/\lambda_0$.

While the preparation of freestanding photonic glasses made of such high index colloids with the right $r/\lambda_0$ values is technically challenging, it would possibly give access to a new scattering regime where signatures of three-dimensional light localization might be observed. Note here that the highest

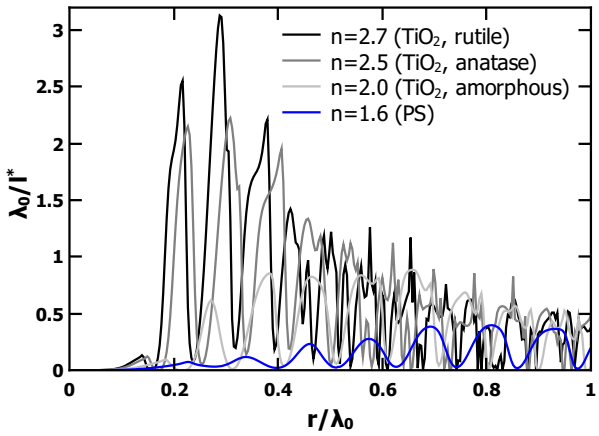


**Figure 3.31:** The ECPA scattering strength is shown for $n = 1.6$ (PS, blue), $n = 2.0$ (amorphous $TiO_2$, light grey), $n = 2.5$ (anatase $TiO_2$, dark grey), $n = 2.7$ (rutile $TiO_2$, black). A surrounding medium index $n_0 = 1.0$ is used.

value of the scattering strength $\lambda_0/\ell^\star \approx 3.18$ for rutile phase $TiO_2$ predicted by the ECPA model in fig. 3.31 is still smaller than the transition value to Anderson localization expected by the Ioffe-Regel criterion (see sec. 2.2.3). Nevertheless, the ECPA scattering model should be tested with high index photonic glass to check the generality of the model and learn about resonant transport in these materials.

The large angle cone setup needs to be used (see sec. 2.3.2) to measure such a high index photonic glass since the cone becomes much wider than for the PS photonic glass using these strong scattering samples. To check whether this setup leads to the same quantitative results as the small angle cone setup, a PS photonic glass ($r = 335$ nm) was measured in both setups (see fig. 3.32). Again, the scattering data of the PS photonic glass is well described by the ECPA model. Moreover, the small and large angle cone measurement overlap very well. Note also that in the analysis of the small angle CBC the effect of internal reflection was neglected while it was taken into account in the analysis of the large angle CBC. This leads to nearly the same results for PS photonic glass because of the low refractive index contrast. For $TiO_2$ internal reflections were always taken into account using eq. (2.17).

### Commercial $TiO_2$ powders

Resonant behavior is expected to smear out for polydisperse photonic glasses. Nevertheless, a wavelength dependency following the mean scattering behavior

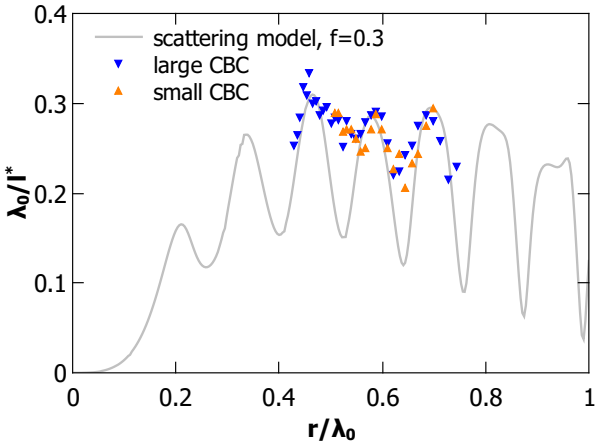


**Figure 3.32:** Two measurements of the scattering strength of the same PS photonic glass with $r = 335$ nm once measured with the small angle cone setup (orange triangles up) and once with the large angle cone setup (blue triangles down) are shown. For comparison the ECPA scattering model is plotted for $f = 0.3$.

might be present. To understand the wavelength dependency of the scattering strength of the commercial "white paint" powders better and understand the behavior observed in sec. 2.5.5, a wavelength scan (from $\lambda_0 = 430$ nm to $\lambda_0 = 790$ nm in $\Delta\lambda_0 = 20$ nm steps) of the scattering strength of these powders was measured and is compared to the ECPA scattering model in fig. 3.33. Here the white light laser combined with the large angle cone setup was used (see sec. 2.3.2). Two rutile powders from DuPont are plotted exemplarily (R960 in red and R700 in blue) since all other powders from DuPont have a similar particle size and show similar scattering behavior. A rutile powder from Aldrich (Aldrich Rutile, AR) with larger particle size is plotted in green. The data is plotted versus the relative size parameter $rn_{\mathrm{TiO_2}}/\lambda_0$. This correction is performed as the data was obtained by varying the wavelength while the scattering model is calculated for a fixed wavelength (590 nm) varying the particle radius. As the refractive index is wavelength dependent the used wavelength in the experiments are weighted by the wavelength dependent $n_{\mathrm{TiO_2}}$ from ref. [110].

The scattering strength of the commercial rutile powders follows the trend of the ECPA scattering model for a large range of $r \cdot n_{\mathrm{TiO_2}}/\lambda_0$ from 0.5 to 2.0. Note that the amplitude of the scattering strength is higher than expected by the model mean value. Either the model slightly underestimates the scattering strength or the random shape of the particles (different from simply polydisperse photonic glass) leads to stronger scattering. Nevertheless, the ECPA

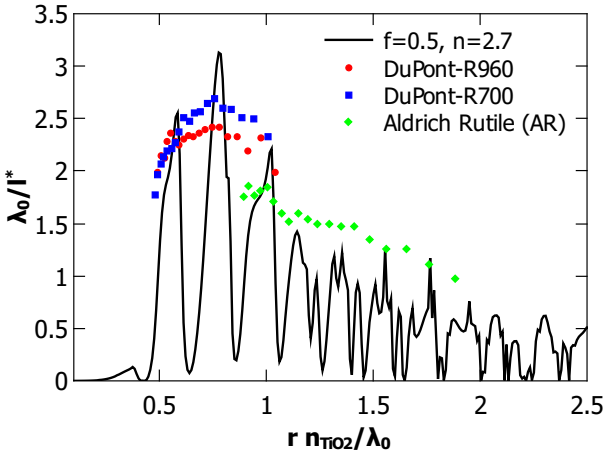


**Figure 3.33:** Scattering strength $\lambda_0/\ell^\star$ of commercial rutile phase "white paint" powders shown for different size ratios $r \cdot n_{\mathrm{TiO_2}}/\lambda_0$. Two DuPont powders (R960 (red circles) and R700 (blue squares)) and one Aldrich powder (Rutile, green diamonds) are compared to the ECPA scattering model with $f = 0.5$ and $n = 2.7$.

model predicts quite well the scattering behavior of the random shaped "white paint" powders.

The same samples were used to study dynamic transport behavior by measuring $D$ spectrally via ToF measurements. This is shown in fig. 3.34(a). The diffusion constant $D$ decreases for increasing size parameter for both kinds of samples. The scattered data points for small wavelengths (large $r/\lambda_0$) might be caused by difficulties with the measurement/analysis due to the low laser power and the strong fluorescence at these wavelengths. From $D$ and $\ell^\star$ the energy velocity $v_\mathrm{E}$ is calculated as shown in fig. 3.34(b).

Surprisingly, the energy velocity decreases constantly with increasing size ratio for both samples in contrast to the behavior of $\ell^\star$. Moreover, it is even lower for the weaker scattering sample AR and for both samples it is lower than the value expected from $v_\mathrm{E} = c/n_\mathrm{MG} \approx 1.87 \times 10^8$ m/s using $f = 0.5$ in the calculation of $n_\mathrm{MG}$. This shows the complexity of the scattering behavior in the multiple scattering, randomly shaped, densely packed samples.

No resonant behavior is observed for the commercial samples. Monodisperse photonic glass needs to be studied to obtain resonant scattering behavior.

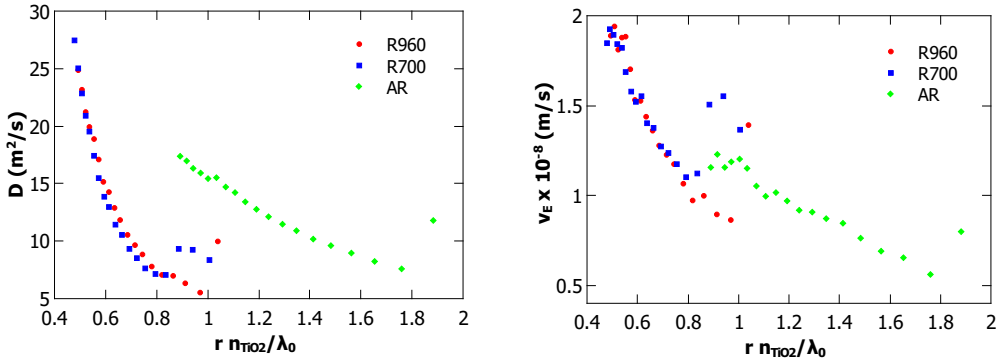


(a) (b)

**Figure 3.34:** The transport behavior is studied by measuring (a) the diffusion constant $D$ via ToF measurements and extracting (b) the energy velocity $v_E$ by knowing $\ell^\star$ from fig. 3.33. The samples are commercial rutile phase $TiO_2$ powders from DuPont (R960 (red circles) and R700 (blue squares)) and from Aldrich (Rutile, green diamonds).

## Custom $TiO_2$ photonic glasses

In a first attempt the spherical but still quite polydisperse photonic glasses of amorphous $TiO_2$ obtained with the synthesis by Eiden-Assmann *et al.* [99] using static stabilization were studied. Spectral CBC measurements (440 nm - 800 nm in 10 nm steps) of two samples were performed. The samples vary in particle radius (229±27 nm and 509±66 nm) and were prepared by pressing the synthesized and dried powders in the same way as the commercial powders. The measured scattering strengths $\lambda_0/\ell^\star$ are shown in fig. 3.35(a) and compared to the ECPA scattering model for amorphous $TiO_2$ (back solid line) using a refractive index of $n = 2.0$ (see sec. 2.3.3) and a filling fraction of $f = 0.5$ justified by the pressing of these samples. No resonant behavior can be seen as expected for highly polydisperse PG, but the data follows the scattering behavior of the model quite well.

In a second attempt the optimized synthesis of Tanaka *et al.* [100] (see sec. 3.3.2) was used to obtain monodisperse (polydispersity $\approx 5\%$) amorphous $TiO_2$ photonic glasses. Figure 3.35(b) shows the spectral measurements of three samples with radius $209 \pm 8$ nm, $228 \pm 11$ nm and $240 \pm 15$ nm. The data is compared to the ECPA model for $n = 2.0$ (amorphous), $f = 0.3$ and a polydispersity of 5% as obtained from the experimental characterization. The experimental data show resonant behavior for all three samples overlapping

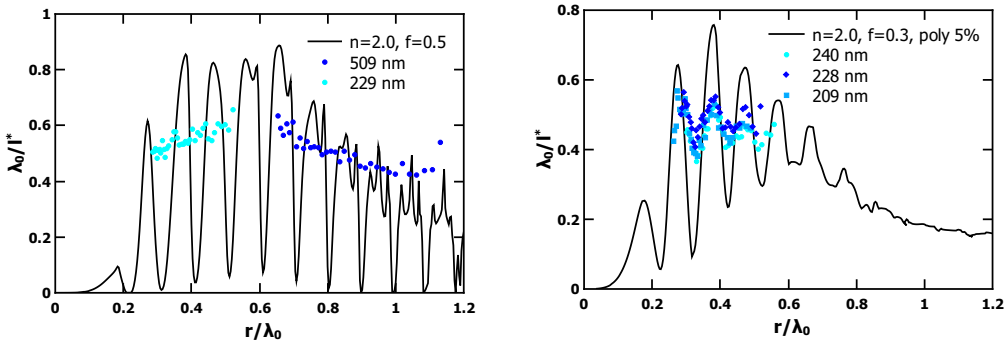


(a) polydisperse amorphous PG (b) monodisperse amorphous PG

**Figure 3.35:** Comparison of the ECPA scattering model with amorphous $TiO_2$ data: (a) shows the scattering strength $\lambda_0/\ell^\star$ of the model for $n = 2.0$ and $f = 0.5$ (black line) compared to the data of two strongly polydisperse samples with radius $229 \pm 27$ nm and $509 \pm 66$ nm. (b) shows $\lambda_0/\ell^\star$ for $n = 2.0$, $f = 0.3$ and a polydispersity of 5% (black line) compared to the data of three nearly monodisperse (polydispersity$\approx$ 5%) samples with radius $209 \pm 8$ nm, $228 \pm 11$ nm and $240 \pm 15$ nm.

very well. The positions of the experimental observed resonances overlap also very well with the predictions from the ECPA scattering model. The data as well as the model show that for larger $r/\lambda_0$ values the resonances smear out by polydispersity. The amplitudes of the observed resonances are weaker than expected from the model, but the mean absolute value matches quite well. Note here that in the experiments the scattering might be lowered by the spectral width (2.5 nm) of the laser and by the hydrogel network that holds the particles together. Still the resonances of the amorphous $TiO_2$ are enhanced by at least a factor of two compared to the PS photonic glass (see fig. 3.26).

The transport behavior in the amorphous $TiO_2$ sample with $r = 228$ nm is studied further in ToF experiments. Figure 3.36 shows measurements of the diffusion coefficient $D$ (black dots) versus the size parameter $r/\lambda_0$. $D$ shows a minimum at exactly the same position where $\ell^\star$ (red squares, same data as in fig. 3.35(b)) has its minimal value. Unfortunately, $D$ could not be measured over the same range of $r/\lambda_0$ since fluorescence caused problems at small $\lambda_0$. Again $v_E$ can be calculated from $D$ and $\ell^\star$ (see blue diamonds in fig. 3.36) and compared to $v_E = c/n_{MG} \approx 2.3 \times 10^8$ m/s (dashed black line). Accounting for the error in the measurement of $L = 0.5 \pm 0.2$ mm, the observed energy velocity agrees quite well with that value. Also a minimum in $v_E$ (blue diamonds) is observed where $\ell^\star$ (red squares) shows a minimum, even though the data are

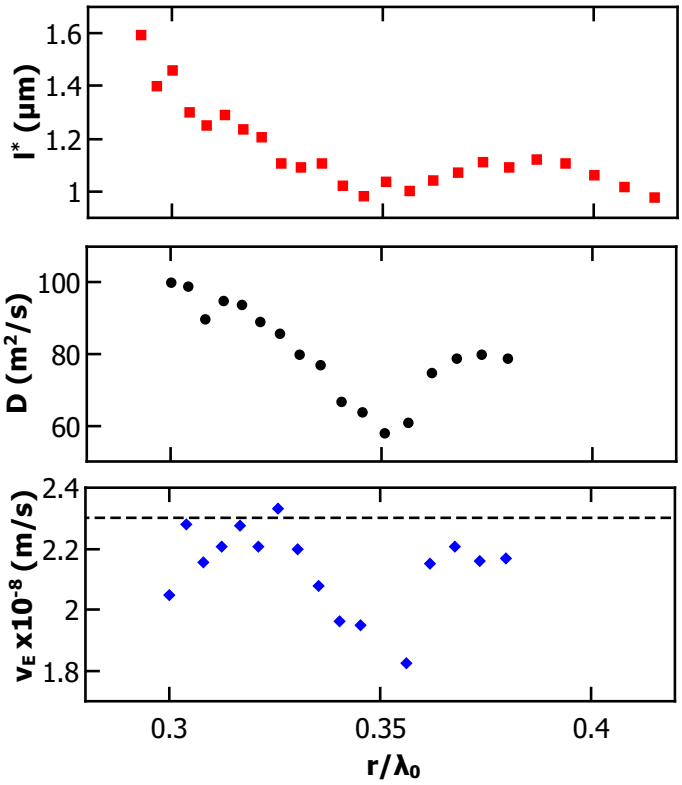


**Figure 3.36:** Spectral measurements of transport mean free path $\ell^\star$ (red squares) the diffusion constant $D$ (black circles) and respectively the calculated energy velocity $v_\mathrm{E}$ (blue diamonds) plotted against the size parameter $r/\lambda_0$. The sample is an amorphous $TiO_2$ photonic glass with particle radius $r = 228$ nm and sample thickness $L = 0.5$ mm (black circles). The dashed black line indicates the energy velocity calculated by the Maxwell Garnett effective refractive index.

quite noisy. Nevertheless, correlated transport behavior is observed for $\ell^\star$, $D$ and $v_\mathrm{E}$ in the experimental data.

Photonic glasses made of anatase $TiO_2$ were synthesized as explained in sec. 3.3.2 by heat treatment of amorphous $TiO_2$ colloids to increase the resonance amplitudes. The scattering strength of these anatase high index photonic glasses is plotted in fig. 3.37(a) (green circles) and compared to the results of amorphous $TiO_2$ photonic glass (blue triangles) and PS photonic glass (violet squares). For all three materials the corresponding prediction from the ECPA model is shown as solid line. Here one can see that also for anatase (green circles) the data follows quite well the predictions of the ECPA model with $n = 2.5$, $f = 0.3$ and 5% polydispersity (black solid line) as predicted for anatase phase $TiO_2$. Again the resonance amplitudes are lowered compared to the model, which might partially be caused by the spectral laser width. A high absorption (during sintering the particles color turned slightly yellowish) leads to a very fast decay of ToF curves such that no quantitative analysis of $D$ was possible for anatase. Nevertheless, a very good prediction of the resonant behavior of monodisperse photonic glasses is possible with the ECPA model for three materials shown in fig. 3.37(a). Moreover, the model describes surprisingly well the scattering behavior of the polydisperse photonic glasses (see fig. 3.37(b)) such as the commercial rutile phase $TiO_2$ (green diamonds) as well as the polydisperse amorphous PG (blue circles). Both materials follow the mean scattering behavior of the ECPA model as already shown earlier in fig. 3.35(a) and fig. 3.33 but here plotted in a logarithmic scale.

The dashed line in fig. 3.37(b) indicates the Ioffe-Regel criterion $k\ell^\star < 1$. Higher refractive index materials are needed to reach a scattering regime where Anderson localization of light should play a role. Sintering the particles at $T > 600$ °C allows the preparation of rutile phase $TiO_2$ as shown in sec. 3.3.2 fig. 3.22(b). Unfortunately the particles start to glue together and change their shape such that the overall scattering behavior cannot crucially be improved and resonances smear out.

Reference [105] shows transmission measurements of $TiO_2$ photonic glasses following the synthesis by Eiden-Assmann *et al.* [99]. They also see resonant behavior in their signal. In the article they claim to use rutile phase $TiO_2$, but no proof (e.g. PXRD measurement) is given. In the corresponding master thesis by M. Reufer [111] more details can be found and a SEM image of the used particles (named Ti28) is shown (Fig 2.21). The particles have a worse polydispersity of 7% than our particles (about $3\% - 5\%$). Moreover, the particle diameter given in the paper (845 nm) does not agree with the particle diameter given in the thesis ($800 \pm 50$ nm). The same discrepancy is given for the sample thickness which is stated in the article with $L = 26$ $\mu$m and

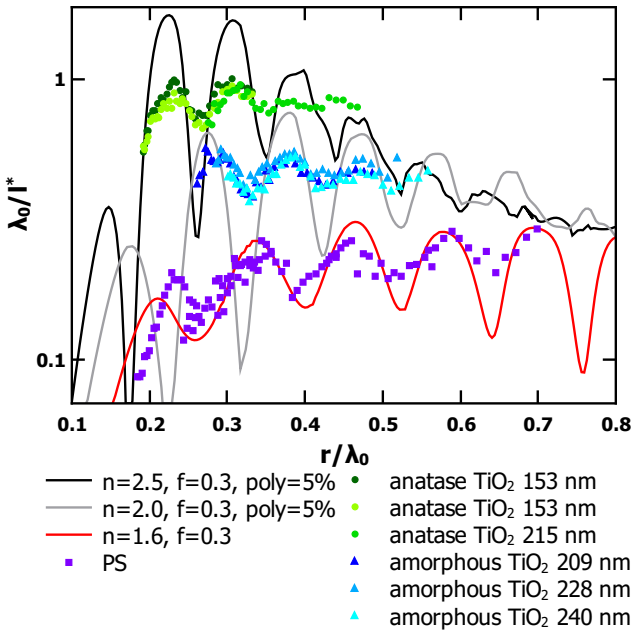


(a) monodisperse

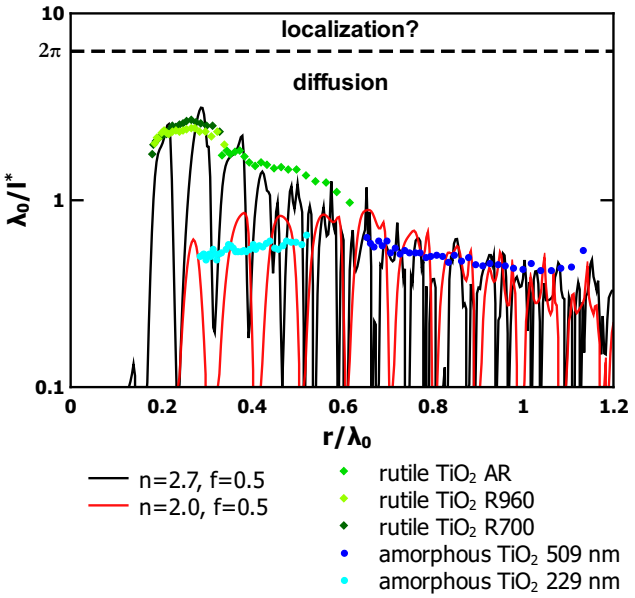


(b) polydisperse

**Figure 3.37:** (a) Comparison of the ECPA scattering model for three refractive indices (solid lines) with the experimental data of the corresponding monodisperse PG for anatase phase $TiO_2$ ($n = 2.5$), amorphous $TiO_2$ ($n = 2.0$) and PS ($n = 1.6$). (b) compares rutile phase $TiO_2$ ($n = 2.7$) and amorphous $TiO_2$ ($n = 2.0$) but with strongly polydisperse PG in the experiments. The dashed black line indicates the critical value $k\ell^\star = 1$ between diffusion and localization.

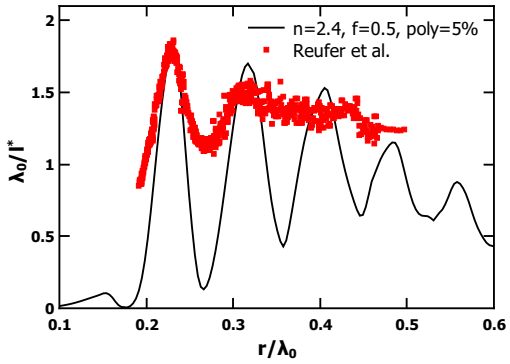


**Figure 3.38:** Scattering strength $\lambda_0/\ell^\star$ of $TiO_2$ photonic glasses recalculated from fig. 2 in ref. [105] for different size ratios $r \cdot n_{TiO_2}/\lambda_0$ is plotted (red squares) and compared to the ECPA scattering model with $f = 0.5$ and $n = 2.4$ and 5% polydispersity.

in the thesis with $L = 20$ $\mu$m. Given this inaccuracy it is hard to compare their data to our ECPA model accurately. Using all information stated in the thesis ($d = 800 \pm 50$ nm, $n_{\text{eff}} = 1.5$ and $f = 0.5$), their $k_{\text{eff}}\ell^\star$ data from FIG. 2 in ref. [105] was recalculated and compared to the ECPA model in fig. 3.38. The data and the ECPA model show very good agreement. The value for the refractive index of the particles found in ref. [111] was $n = 2.45$ lower than for pure rutile phase in contrast to the statement in ref. [105]. Thus, $n = 2.4$ was used here for comparison with the ECPA scattering model (black solid line in fig. 3.38).

The comparison of the ECPA scattering model (described in sec. 3.2) with light sctattering data of low index and high index photonic glasses as summarized in fig. 3.37 as well as the comparison of the model to literature data from Garcia *et al.* [23] for polysterene and Reufer *et al.* [105] for $TiO_2$ shows that the presented model predicts very well the scattering behavior of any type of photonic glasses and can even be applied to other "white paint" materials. The scattering model was tested experimentally for four different indices (polystyrene $n = 1.6$, amorphous $TiO_2$ $n = 2.0$, anatase $TiO_2$ $n = 2.5$ and rutile $TiO_2$, $n = 2.7$). Difficulties in the preparation of higher index photonic glasses as well as the lack of higher index materials with low absorption in this wavelength region hinders to reach a stronger scattering regime than in the earlier available commercial materials and thus hinders to reach a regime where Anderson localization plays a role. Further research in material science and further investigation of the role of the scatterers' shape and the material structure is nessecary to reach this regime eventually.

# Chapter 4

# Magneto-optical Faraday effect in multiple light scattering

Beside the need of a higher scattering strength and the connected quest for a more quantitative understanding of light transport in densely packed, highly scattering media as studied in the latter chapter, one can raise the question if the used characterization methods to look for localization of light (time and spatial resolved transmission measurements) are sufficient to observe this phenomenon. One contribution to Anderson localization arises from constructive interference of reciprocal multiple scattering paths [48] as discussed in sec. 2.2.3. If one can manipulate this interference, localization effects can directly be manipulated and thus be distinguished from other effects. This idea stimulated the following study on magnetic fields effects in strongly scattering samples.

In the first part of this chapter I will discuss how the magneto-optical Faraday effect might be used to influence Anderson localization of light. Therefore, one needs to understand how the Faraday effect changes the photons phase (polarization) in single scattering and how this effect survives in the multiple scattering regime. Further I will point out how it influences measurable multiple scattering quantities such as the CBC or transmission speckle. After introducing a CBC setup and a speckle interferometer setup in high magnetic fields, I will present experimental results on multiple light scattering in Faraday active materials. I will show measurements of the CBC and the speckles in transmission as in refs. [112, 25], but on samples scattering more strongly (although still in the weak localization regime) with $\ell^\star$ in the $\mu$m range. The experiments are all performed at low temperature since the Faraday rotation increases with deceasing $T$ in the used paramagnetic materials.

In particular, I discuss the manipulation of reciprocity in reflection and transmission geometry by comparing the effect of the magnetic field on the CBC with its effect on the transmitted speckle in multiple scattering, slab

shaped samples. This shows how the magneto-optical Faraday effect in light transport depends on the geometry of the experiment. In the experimental range studied (high $B = 18\,\mathrm{T}$ and low $T < 10\,\mathrm{K}$) the used Faraday active material (cerium fluoride, $CeF_3$) shows a saturation effect. Therefore, I perform a temperature and magnetic field study of the Faraday rotation of $CeF_3$ in multiple scattering samples by measuring transmission speckle and compare it to measurements of the Faraday rotation on bulk $CeF_3$. Finally, ToF measurements on mixtures of strongly scattering powders ($TiO_2$) and Faraday active powders ($CeF_3$) in high magnetic fields are presented to check the result from sec. 2.5 that no signs of localization are observed in the previously studied commercial "white paint" samples (see sec. 2.4).

## Contents

## 4.1 How the Faraday effect may influence Anderson localization

In the localized state the contribution of reciprocal paths to light transport becomes significant, which leads to a vanishing diffusion coefficient in an infinite medium as explained in sec. 2.2.3. Because Anderson localization is an interference effect, it should be affected if the relative phase between the reciprocal waves is perturbed. This idea was indeed supported by the observation of the destruction of the CBC (which is often seen as the precursor of Anderson localization) in Faraday active multiple scattering samples [112, 25]. The Faraday effect, which will be explained in more detail in the following sections, rotates the plane of polarization and thus changes the phase of the photons, depending on their way through the sample in respect to the magnetic field. Counter propagating photons will therefore collect opposite phases on their way through the sample. Thus, measuring the destruction of the CBC by a magnetic field, proves the origin of weak localization to be the constructive interference on reciprocal scattering paths. While optical waves still bear to show signs of localization in 3D samples (see sec. 2.5 and ref. [54, 71]), Faraday rotation is still a good candidate for a sensitive probe of the same origin for Anderson localization of light. Moreover, controlling the transition from localization to diffusion by a magnetic field using the magneto-optical Faraday effect would be an experiment that has not been done before. Such a method could also be used to avoid confusing localization effects with deviations from diffusion that originate from other effects such as the fluorescent signals in sec. 2.5.5. For such experiments the samples must show a strong magneto-optical Faraday effect to destroy time reversal symmetry for certain paths in these samples. A detailed characterization of such samples and a detailed explanation of the Faraday effect can be found in my master thesis [29].[1]

## 4.2 Faraday effect in homogeneous media

Magneto-optical Faraday rotation refers to the effect that linear polarized light rotates its plane of polarization when it propagates through a homogeneous, dielectric medium, in which a magnetic field is applied parallel to the propagation direction of the light [113] (see fig. 4.1(a)).

[1] This sections about the Faraday effect summarizes this description and is thus taken partly literally from that thesis and merged with the description from a publication of myself and coworkers [81].

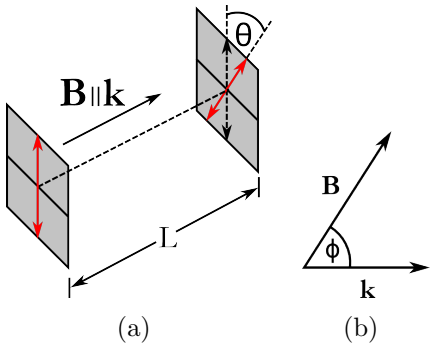


**Figure 4.1:** Faraday effect in homogeneous media: (a) the plane of polarization is rotated by an angle $\Theta$ when propagating along the magnetic field $\mathbf{B}$. $L$ is the sample length. (b) Angular dependency $\phi$ between the magnetic field $\mathbf{B}$ and the wave vector of the light $\mathbf{k}$.

The rotation angle $\theta$ of the plane of polarization is proportional to the length $L$ of the material, the projection of the magnetic field $\mathbf{B}$ on the wave vector $\mathbf{k}$ of the light ($\mathbf{B} \cdot \frac{\mathbf{k}}{|\mathbf{k}|}$, geometry sketched in 4.1(b)) and a material constant $V$ (called Verdet constant):

$$\theta(B) = VBL\cos(\phi) \ . \tag{4.1}$$

A simple explanation of the effect can be given by separating the incoming linear polarized light in two circular polarized beams (left and right circular polarization). The two circular polarized waves $\mathbf{E}_\pm$ (with $+$ positive and $-$ negative helicity) propagate with a different speed of light ($c/n_\pm$) through the medium. This difference is caused by the magnetic field induced difference in the real part of the refractive indices of the left $n_-$ and the right $n_+$ circular polarized light. Overlapping these two polarizations after propagating a certain length $L$ leads to a phase shift $\theta$ of the linear polarized light

$$\theta = \frac{\omega}{2c}(n_-(\omega) - n_+(\omega))L \ , \tag{4.2}$$

equal to the rotation angle of the Faraday effect in eq. (4.1). Due to the origin of the Faraday rotation in the difference of the real part of the refractive indices for left and right circular polarized waves, it is called magnetic circular birefringence. Magnetic circular dichroism refers to the same effect for the imaginary part of the refractive index and leads to elliptic polarized light in strongly absorbing media.

More precisely the origin of the Faraday effect is the Zeeman splitting of the atomic energy levels in an external magnetic field as described by Becquerel [114]. In a dielectric material the oscillation of the atomic electrons, caused by the external electric alternating field from the incoming light, can be separated by using three spare electrons. The oscillation parallel to the magnetic field is not influenced by the magnetic field. The oscillation vertical to the field can be separated in two opposite circular oscillations. These two circular atomic ring currents are disturbed by the Lorentz force of the magnetic field and thus get positive or negative accelerated depending on their direction of rotation. These spare electrons emit circular polarized light which is frequency shifted by $\pm\Delta\omega_{\text{Zeeman}} = \mu_B B/\hbar$, with the Bohr magneton $\mu_B = e\hbar/2m$. Thus, the resonant frequencies of the spare electrons are $\omega_\pm = \omega_0 \pm \omega_\text{L}$, with $\omega_0$ the resonance frequency of the system without magnetic field and $\omega_\text{L} = \frac{eB}{2m}$ the Lamor frequency. The rotation angle $\theta$ can be expressed for small $\omega_\text{L}$ as:

$$\theta = \frac{\omega_\text{L}}{c} L\omega \frac{dn}{d\omega} = \frac{e}{2mc}\omega\frac{dn}{d\omega}BL \ . \tag{4.3}$$

In this formula the linear relation of the Verdet constant to the dispersion relation of the medium $dn/d\omega$ is shown:

$$V = \frac{e}{2mc}\omega\frac{dn}{d\omega} \ . \tag{4.4}$$

A complete theoretical description of the magneto-optical Faraday rotation can be found for example in ref. [115]. A detailed summary of these descriptions can be found in [29]. Here I want to point out only the most important properties of Faraday rotation.

In a diamagnetic material with one dominating resonance $\omega_0$ in the dispersion of the material the frequency dependency of the Verdet constant is given by

$$V \propto \frac{\omega^2}{(\omega_0^2 - \omega^2)^2} \ . \tag{4.5}$$

A higher Faraday rotation angle is thus expected for a wavelength of the incoming light near a resonance. Moreover, in diamagnetic materials the Verdet constant is usually small, positive and temperature independent. In contrast to that, paramagnetic materials consist of a weak positive diamagnetic contribution and stronger negative paramagnetic one. For a typical paramagnetic material with one dominant transition at a wavelength $\lambda_0$, and an incident

wavelength $\lambda$ far away from resonance the Verdet constant shows the following proportionalities [116]:

$$V_0 \propto \frac{1}{T}\frac{1}{\lambda_0^2 - \lambda^2} \ . \tag{4.6}$$

At very low temperatures this expression is not valid anymore. $V$ is proportional to the magnetic susceptibility [117] which is the $B$-derivative of the magnetization. One can assume therefore that it can be written for low temperatures [118] as

$$V(B) = \frac{\kappa\alpha}{T}\left[1 - \tanh^2\left(\frac{\alpha}{T}B\right)\right], \tag{4.7}$$

where $\kappa$ and $\alpha$ are material specific constants. $V_0 = \kappa\alpha/T$ is the usual Verdet constant. Now one can replace the phase $VB$ in eq. (4.1) by

$$\int_0^B V(B')\mathrm{d}B' = \kappa \cdot \tanh\left(\frac{\alpha}{T}B\right). \tag{4.8}$$

$\alpha$ is the parameter describing the saturation of the Faraday rotation. Note the saturation of the Faraday rotation for low temperatures and high magnetic fields. In the experiments paramagnetic materials are used for the Faraday rotation to take advantage of the scaling of the Verdet constant with $1/T$.

Before explaining the magneto-optical Faraday effect in multiple scattering media, the relevance of this effect for our experiments should be outlined. Optical active materials (e.g. sucrose) also show a rotation of the plane of polarization if linear polarized light propagates through them. Here the origin is in the chiral structure of the molecules. By inverting the direction of propagation, the linear polarized light rotates back to its starting angle. This is different for magneto-optical materials. The magnetic field specifies one direction in the material. Changing the direction of propagation $\mathbf{k}$ of the light changes the rotation direction in the coordinate system of the light because the change of $\mathbf{k}$ is connected to a helicity change of the light. This means that the rotation direction stays the same in the laboratory coordinate system. After passing again through the medium in the different direction, the overall rotation is $2\theta$ while in the case of optical active materials this would be zero. A common technical application of this effect is the Faraday isolator.

A consequence of this property of the magneto-optical Faraday rotation is that it leads to the destruction of the time-reversal symmetry in a material, meaning that two photons propagating the same path in the opposite direction in a multiple scattering magneto-optical material do not necessary collect the same phase.

## 4.3 Faraday effect in multiple scattering media

In this section the concept of multiple light scattering as introduced in sec. 2.1 is matched with the Faraday effect explained in the last section to understand light transport in a multiple scattering, magneto-optical medium under the influence of an external magnetic field. Erbacher *et al.* [30, 112] derived a simple model of the magneto-optical Faraday effect in multiple scattering media in the diffusive regime ($L \gg l^*$). In this regime the random walk model of sec. 2.1.1 applies. A detailed summary of their model can be found in ref. [29].

Similar to the diffusion process of the light, where the information of the origin of the light is lost after a length $\ell^\star$, the memory of Faraday rotation is restricted to a correlation length of $\ell^\star_{\mathrm{FR}}$. In their model the correlation length of the Faraday rotation $\ell^\star_{\mathrm{FR}}$ is assumed to be of the same order of magnitude as the correlation length of the photon transport $\ell^\star$. Lenke *et al.* [119] showed a scatterer size dependency, where the ratio $E_V = \ell^\star_{\mathrm{FR}}/\ell^\star$ decreases from 2 for Rayleigh scatterers to 1 with increasing scatterer size. This gives a physical explanation of the underestimation of the Faraday rotation in such multiple scattering samples as observed by Erbacher *et al.* [112]. Still $\ell^\star$ and $\ell^\star_{\mathrm{FR}}$ are in the same order of magnitude, such that the assumption $\ell^\star \approx \ell^\star_{\mathrm{FR}}$ leads to a correct physical description of the Faraday effect in multiple scattering media.

For a photon propagating in a magneto-optical medium on a path $\mathbf{s}$, where the path length is smaller than the scattering mean free path ($|\mathbf{s}| < \ell_s$), the Faraday rotation follows eq. (4.1): $\theta = V\mathbf{B}\mathbf{s}$. For a much longer path length, the Faraday rotation on each path is correlated over the length $\ell^\star$. The first step of a certain path is called $\ell_1$. The contribution of this path to the overall Faraday rotation is given by the projection of a vector with length $\ell^\star$ in direction $\ell_1$ on the magnetic field $\mathbf{B}$. So, each scattering path $s$ can be separated in statistical independent parts $\ell^\star$, that contribute to the mean Faraday rotation of this path by

$$\theta = VB\ell^\star \cos(\phi) \ , \tag{4.9}$$

where $\phi$ is the angle between $\ell_1$ and $\mathbf{B}$. Since $\ell_1$ can be arbitrary oriented with respect to $\mathbf{B}$ (in an infinite medium) the mean rotation angle is zero $\langle\theta\rangle_\phi = 0$ (here $\langle\cdot\rangle_\phi$ is the average over the solid angle $4\pi$). For finite size media in transmission geometry the mean of the projection of each step on the propagation direction equals the sample size $\langle\cos(\phi)\rangle_\phi = L$. This would lead to a mean rotation angle $\langle\theta\rangle_\phi = VBL$. However, the depolarization occurring in each scattering event randomized this averaging process and leads to $\langle\theta\rangle_\phi = 0$ even for finite size systems in transmission. In contrast to that, the mean

squared phase shift is different from zero:

$$\langle\theta^2\rangle_\phi = (VBl^*)^2\langle\cos^2(\phi)\rangle_\phi \ . \tag{4.10}$$

The strength of the Faraday rotation in multiple scattering samples can be quantified by measuring the correlation decay of the transmission speckle with an applied magnetic field as outlined in the following section.

### 4.3.1 Speckle correlations in transmission

Shining coherent laser light through a multiple scattering sample, the radiation coming from the sample surface interfere and form a speckle pattern. Applying a magnetic field, the propagation of a photon along the magnetic field leads to an effective change of the photons phase, ending in a change of the speckle pattern for different applied fields, described in detail in ref. [30, 112]. Here a summary is given.[2]

A decay of the speckle intensity correlation function $C(B) = g_2(B) - 1$, with $g_2(B) = \langle I(0)I(B)\rangle/\langle I(0)\rangle^2$, can be used to quantitatively measure the strength of the Faraday rotation and thus the Verdet constant $V$. In our experiments this is done by multiplying two images at different field strengths $B$, and normalizing the average over all pixels of this product. In general, the field auto-correlation function is defined as follows [30]:

$$g_1(B) = \sqrt{C(B)} = \frac{\langle E(0)E^*(B)\rangle}{\langle E(0)\rangle^2} \ . \tag{4.11}$$

If the diffusion approximation is valid, the paths through the sample are statistically independent. Thus, equation (4.11) can be simplified since all cross terms $E_k(0)E_l^*(B)$ with $k \neq l$ drop out. Moreover, the independence of the photon paths allows to calculate $g_1(B, s)$ for every path with a specific path length $s$ separately. The overall correlation is then obtained by summing over all paths and weighting them with the path-length distribution function $P(s)$:

$$g_1(B) = \int_{\ell^\star}^{\infty} g_1(B, s)P(s)ds \tag{4.12}$$

Here the sum was replaced by an integral since the number of different path lengths $N$ with $s = N\ell^\star$ is a high number in the strong multiple scattering regime.

[2]Partly taken from my master thesis [29] and a publication of myself and coworkers [81].

The assumption $\ell^\star_{FR} \approx \ell^\star$ means that the phase change $\Delta\Phi$ on every step $\ell^\star$ is independent. In this limit $g_1(B,s)$ can be expressed as $s/\ell^\star$ individual terms

$$g_1(B,s) = \langle g_1(B,\ell^\star)\rangle^{s/\ell^\star} \ . \tag{4.13}$$

The contribution for one statistical independent step $\ell^\star$ to the overall correlation can be calculated to be [30]

$$g_1(B,\ell^\star) = \langle\cos(\theta)\rangle = \langle\cos(VB\ell^\star\cos(\phi))\rangle \ . \tag{4.14}$$

Since on a length scale $\ell^\star$ the Faraday rotation acts as in a homogeneous medium, this result equals the correlation decay of the normal Faraday effect for a sample of length $L$: $C(B) = g_1^2(B) = \cos^2(VBL)$. For small rotation angles along each step $\ell^\star$ ($VB\ell^\star \ll \pi/2$), eq. (4.14) can be further simplified to

$$g_1(B,\ell^\star) = \int_0^\pi \cos(VB\ell^\star\cos(\phi))\sin(\phi)d\phi = \frac{\sin(VB\ell^\star)}{VB\ell^\star} \tag{4.15}$$

$$\approx 1 - \frac{(VB\ell^\star)^2}{6} \approx \exp(-\frac{(VB\ell^\star)^2}{6}) \ . \tag{4.16}$$

Using the path length distribution function $P(s)$ for a slab in transmission in the diffusive regime including absorption (eq. (2.14)), the field auto-correlation function states:

$$g_1(B) = \sqrt{C(B)} = \frac{\sinh\left(\tilde\gamma\ell^\star\sqrt{\frac{(VB)^2}{2} + (\frac{1}{L_\mathrm{a}})^2}\right)\sinh\left(\frac{L}{L_\mathrm{a}}\right)}{\sinh\left(L\sqrt{\frac{(VB)^2}{2} + (\frac{1}{L_\mathrm{a}})^2}\right)\sinh\left(\tilde\gamma\frac{\ell^\star}{L_\mathrm{a}}\right)}. \tag{4.17}$$

$\tilde\gamma = 1+\gamma = 5/3$ is the boundary condition factor introduced in sec. 2.1.1 and $L_\mathrm{a}$ the macroscopic absorption length. In this formula the two addends under the square root $(VB)^2/2+1/L_a^2$ show the competition between the magnetic cutoff length and the absorption cutoff length, while the bigger addend dominates eq. (4.17). The material constant $V$, and thus, the strength of the Faraday effect, can be extracted from a measurement of the intensity correlation function in transmission for a slab if all other parameters are known.

The intensity correlation function $C(B)$ calculated from eq. (4.17) is plotted in fig. 4.2 for typical experimental parameters $V = -500$ rad/Tm, $L = 2.2$ mm, $L_\mathrm{a} = 750$ $\mu$m and $\ell^\star = 2$ $\mu$m (red solid line). It starts at $C(0) = 1$ and shows a Gaussian behavior for small fields. For larger fields it changes over to an

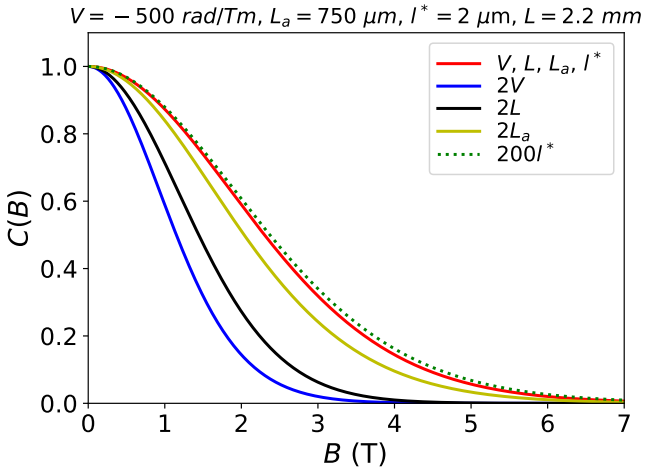


**Figure 4.2:** Plot of the intensity correlation function $C(B)$ calculated from eq. (4.17) for typical experimental parameters: $V = -500$ rad/Tm, $L = 2.2$ mm, $L_\mathrm{a} = 750$ $\mu$m and $l^* = 2$ $\mu$m (red solid line). The parameters $V$, $L$, $L_\mathrm{a}$ are varied (blue, black yellow solid lines) by a factor of 2. The green dashed line shows the correlation when varying $\ell^\star$ by a factor of 200.

exponential decay and goes down to zero for very large fields. The parameters $V$, $L$, $L_\mathrm{a}$ are varied by a factor of 2 (blue, black and yellow solid lines). These curves show that the decay of $C(B)$ strongly depends on the sample thickness $L$ and the Verdet constant $V$. Absorption cuts of scattering path, such that a smaller absorption (larger $L_\mathrm{a}$) yields stronger Faraday rotation and thus a faster decay of $C(B)$. The transport mean free path $\ell^\star$ only weakly affects $C(B)$ even when varying by a factor of 200 (green dashed line).

### 4.3.2 Coherent backscattering in magnetic fields

The concept of coherent backscattering was already introduced in sec. 2.2.1. As it is an interference phenomenon arising from reciprocal scattering paths, this effect will strongly be influenced by breaking reciprocity via Faraday rotation.[3]

In Faraday active multiple scattering samples, Lenke *et al.* [25] describe the field induced breaking of reciprocity of light transport by a simple model. Their model is based on the description of the CBC from Akkermans *et al.* [33]. The angular dependence of the coherent intensity $I(q)$ with the backscattering vector $q$ ($q = 4\pi \sin(\theta/2)/\lambda$ with $\theta$ the backscattering angle ($\theta = 0$ and therefore

[3]This paragraph is taken in parts from a publication of myself and coworkers [81].

$q = 0$ for backscattering) and $\lambda$ the wavelength) is a continuous sum over all scattering paths

$$I(q) = 1 + \frac{1}{I(0)} \int_{\ell^\star}^{\infty} P(s) \exp\left(-\frac{s}{3\ell^\star}(q\ell^\star)^2\right) \mathrm{d}s \ , \tag{4.18}$$

The path length distribution $P(s)$ for very thick slabs in reflection geometry decays as $P(s) \approx s^{-3/2}$ in the diffusive regime. This leads to a simple description of the angular dependency of the CBC [25]:

$$I(q) = 1 + \frac{1 - \exp\left[-2\tilde{\gamma} q \ell^\star\right]}{2\tilde{\gamma} q \ell^\star} \tag{4.19}$$

The difference in Faraday rotation angle between reciprocal paths on steps $\ell^\star$ is given by $2VB\ell^\star \cos(\phi)$ according to eq. (4.9). This leads to a magnetic field induced $\phi$ averaged contribution to $I(q)$ of paths of length $s$ by $\exp\left(-s/3\ell^\star \cdot 2(VB\ell^\star)^2\right)$. Since the phase shifts due to Faraday rotation are independent of phase shifts due to a variation of the scattering angle $\theta$, the CBC intensity $I(q, B)$ can be written as a function of the backscattering vector $q$ and the magnetic field $B$ as follows:

$$I(q, B) = 1 + \frac{1}{I(0, 0)} \int_{\ell^\star}^{\infty} P(s) \exp\left(-\frac{s}{3\ell^\star}\left[(q\ell^\star)^2 + 2(VB\ell^\star)^2\right]\right) \mathrm{d}s, \tag{4.20}$$

and thus

$$I(q, B) = 1 + \frac{1 - \exp\left[-2\tilde{\gamma}_R \, q_\mathrm{F}(q, B) \, \ell^\star\right]}{2\tilde{\gamma}_R \, q_\mathrm{F}(q, B) \, \ell^\star}. \tag{4.21}$$

Here $q_\mathrm{F}(q, B) = \sqrt{q^2 + 2(VB)^2}$, $V$ is the sample's Verdet constant and $\tilde{\gamma}_\mathrm{R} = \frac{1+R}{1-R}(1 + \gamma)$ is a factor related to the boundary condition, with $\gamma \approx 2/3$ the Milne parameter and $R$ the total reflectivity. The factor $\frac{1+R}{1-R}$ is the correction for internal reflections as calculated by Zhu *et al.* [37] and already introduced in sec. 2.2.2. It becomes relevant in our high refractive index samples.

The CBC intensity enhancement $I(0, B)$ calculated from eq. (4.21) is plotted in fig. 4.3 for typical experimental parameters $V = -1500$ rad/Tm, $l^* = 60$ $\mu$m and neglecting internal reflections ($R = 0$) as red solid line. Although more appropriate (but more complex) models for the CBC are known (e.g. described in sec. 2.2.2) this simple description shows that the destruction of the cone tip intensity $I(q = 0, B)$ with the field, and thus the breakdown of reciprocity, depends exponentially on the product of three parameters: the magnetic field $B$, the Verdet constant $V$ and the transport mean free path $\ell^\star$. In fig. 4.3 the parameters $V$ and $\ell^\star$ are varied by a factor of 2 (blue and yellow solid

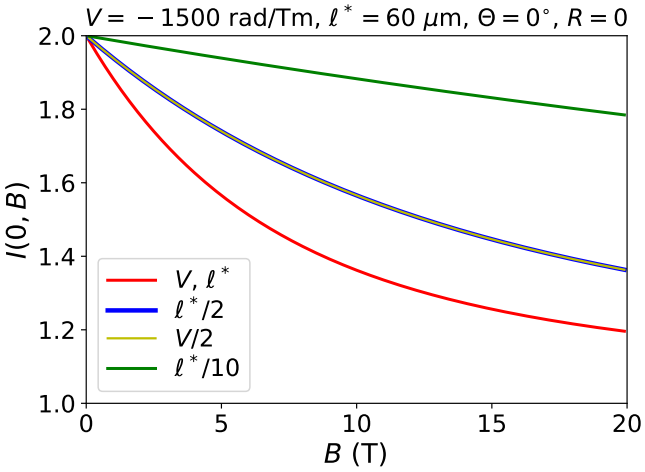


**Figure 4.3:** Plot of the CBC intensity enhancement $I(0, B)$ calculated from eq. (4.21) for typical experimental parameters: $V = -1500$ rad/Tm, $l^* = 60$ $\mu$m and neglecting internal reflections $R = 0$ (red solid line). The parameters $V$ and $\ell^\star$ are varied (yellow and blue solid lines) by a factor of 2. The green line shows the backscattering enhancement when lowering $\ell^\star$ by a factor of 10.

lines). These curves show that the decay of $I(q = 0, B)$ equally depends on these two parameters. Since $V$ is fixed for a chosen material, temperature and wavelength, and $B$ is limited by the experimental setup, the dependency on $\ell^\star$ sets the limits for the measurable range of the destruction of the CBC. For very strong scattering samples (small $\ell^\star$, green solid line), the cone tip will hardly be affected by Faraday rotation with the available magnetic fields.

In contrast to the decay of the CBC with the magnetic field, the decay of the transmission speckle only weakly depends on the scattering length $\ell^\star$, but is dominated by the sample thickness $L$: it is governed by $\exp(-VBL)$ for low absorbing samples (large $L_\mathrm{a}$). This difference between this technique and the CBC is a consequence of the different path length distributions in reflection and transmission geometry. The transmission speckle method can thus be used to quantify the Faraday rotation also in strongly scattering samples with relatively low $\ell^\star$ values, which are hard to measure in CBC experiments with the available magnetic fields and materials.

## 4.4 Faraday active samples

Highly scattering samples are required to observe localization effects. The strongest scattering "white paint" samples available in this thesis are commercial titanium dioxide powders from DuPont as was shown in sec. 3.4.3. Titanium dioxide is a diamagnetic material with a low Verdet constant even at low temperature ($V = 100\,\mathrm{rad/T \cdot m}$ at $\lambda = 457\,\mathrm{nm}$ and $T = 77\,\mathrm{K}$ [120]). Thus the idea was to mix this strongly scattering powder with a paramagnetic strongly Faraday active (at low temperatures) powder to obtain strong scattering behavior and strong Faraday rotation.

### 4.4.1 Cerium fluoride

The Faraday active material used is cerium fluoride (Sigma Aldrich $CeF_3$ powder). $CeF_3$ is a paramagnetic rare earth tri-fluoride that shows low absorption in the entire visible region where it has a refractive index of $n = 1.6$ [73]. Crystalline bulk $CeF_3$ has a high negative Verdet constant of $V_{CeF_3} = -1.1 \cdot 10^3\,\mathrm{rad/T \cdot m}$ at $\lambda = 457\,\mathrm{nm}$ and $T = 77\,\mathrm{K}$ [121]. This large material constant is caused by the electronic transitions between the electron configurations 4f and 5d of the trivalent rare earth ions ($Ce^{3+}$) [117]. The temperature and wavelength dependency is given by:

$$V_{CeF_3}(\lambda, T) = V_{CeF_3}(\lambda', T')\frac{\lambda'^2 - {\lambda_0}^2}{\lambda^2 - {\lambda_0}^2}\frac{T'}{T}\ , \tag{4.22}$$

where $\lambda_0 = 300\,\mathrm{nm}$ [121]. A SEM image of the used $CeF_3$ powder is shown in fig. 4.4(a). The particle diameter varies strongly between $0.2 - 5.0\ \mu$m with an average diameter of $d \approx 2.0\ \mu$m [116]. Note further that the particles are random shaped, meaning that they have no spherical or well defined appearance.

### 4.4.2 Powder mixtures

In general, paramagnetic materials such as $CeF_3$ show a higher absorption and have a lower refractive index in the visible than the titanium dioxide powders such that using a paramagnetic powder only ends in relatively weak scattering behavior. $CeF_3$ is thus mixed with $TiO_2$ (DuPont R700, see sec. 2.3.3 for specs) to reach a stronger scattering regime. Only small amounts of $CeF_3$ ($\sim 5$ vol%)) are necessary to obtain a full decay of the speckle correlation such that the scattering behavior is dominated by the $TiO_2$. The overall Verdet constant can

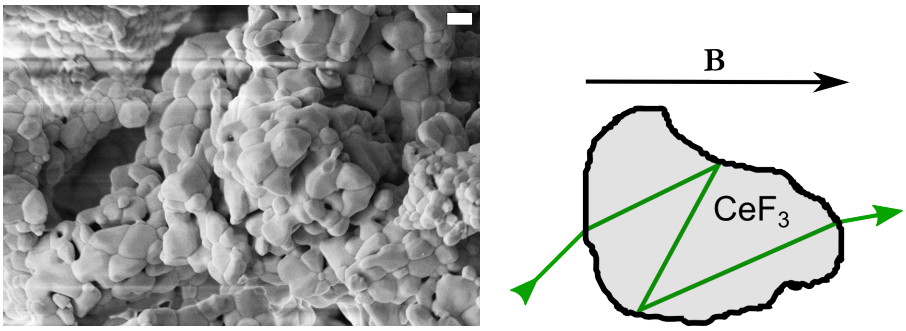


(a) $CeF_3$ (b) internal reflections

**Figure 4.4:** (a) SEM image of pure cerium fluoride powder used in the experiments. The particles' diameter varies strongly between $d = 0.2 - 5.0$ $\mu$m. Scale bar: 1 $\mu$m. (b) Sketch of the internal reflection process that might take place in the $CeF_3$ particles and might lead to an enhanced Faraday rotation in a magnetic field **B**.

be calculated as follows:

$$V_{\text{vol}} = f_{\text{CeF}_3} V_{\text{CeF}_3} + f_{\text{TiO}_2} V_{\text{TiO2}_2} \ , \tag{4.23}$$

with $f_x$ the volume fraction and $V_x$ the bulk Verdet constant. The error of $V_{\text{vol}}$ can be calculated from the error of the used powder masses.

In these mixtures the larger random shaped particles of $CeF_3$ are surrounded by many smaller $TiO_2$ particles. Thus the photons can shorten their way through the samples by passing through the $CeF_3$ leading to a smaller scattering strength. Moreover, one can imagine a process sketched in 4.4(b). The light can undergo internal reflections in the particles. This would lead to effective longer path lengths in the magneto-optical particles and thus an enhanced Faraday rotation than expected from the calculation of the Verdet constant $V_{\text{vol}}$. As mentioned in sec. 4.3 such an enhancement was already observed by Erbacher *et al.* [112]. The change of the scattering behavior and of the Faraday rotation in such powder mixtures compared to pure samples was a further stimulation for these experiments. It should be tested whether such mixtures are suitable for transport experiments in magnetic fields if localization is found.

The powders were embedded in a matrix of glycerol to overcome any change of the speckle by displacement of the paramagnetic particles in the applied field and to lower thermal motion of the small $TiO_2$ particles.[4] It freezes out

[4]Note that cooling the samples to liquid helium temperature in the experiment also lowers thermal motion and stabilizes the speckle correlation [29].

at $T_m = 18.2\,°C$ such that it forms a stable matrix at the temperatures used in the experiments. Glycerol is only weakly Faraday active ($V = 3.87\,\mathrm{rad/T \cdot m}$ at $\lambda = 589\,\mathrm{nm}$ and $T = 16\,°C$ [73]). A disadvantage is the relatively high refractive index $n = 1.47$ at $\lambda = 589$ nm [73] which lowers the refractive index contrast.

For the CBC measurements, where only weaker scattering samples are measurable due to the dependency of $\ell^\star$ on the decay of the cone with the magnetic field, embedding $CeF_3$ particles in glycerol can be used to lower the scattering strength. In the CBC experiments a variable amount of titanium dioxide powder (anatase $TiO_2$, Sigma-Aldrich, see [54]) was added to this mixture. This allows to change the scattering strength without changing the Faraday rotation strength. The mixtures were filled in slab shaped closed sample holders. A detailed description of the sample holder can be found in my master thesis [29].

## 4.5 Optical setups in high magnetic fields

A speckle interferometer setup is used for speckle transmission measurements to characterize the magneto-optical Faraday rotation in multiple scattering media for different field strength and at different temperature. Therefore, a superconducting 7 T Magnet is used and the samples are cooled in an optical flow cryostat. The setup was switched to a superconducting 18 T magnet with an optical cryostat (see ref. [36] for details), to possibly measure stronger scattering samples and/or characterize the saturation of Faraday rotation in high magnetic fields. For a measurement of similar samples in coherent backscattering geometry and to test the destruction of reciprocity in these samples, a similar setup as in sec. 3.3.1 was used but again in the 18 T magnet. All samples were measured in optical flow cryostats to cool the samples to liquid helium temperatures. This was done to obtain a high paramagnetic Faraday rotation and lower thermal movements of the particles in the samples. These setups are described first. Later a time of flight setup as described in sec. 2.3.1 was built but again with the sample placed in a flow cryostat and using the superconducting 18 T magnet to measure the effect of the Faraday rotation on transport behavior.

### 4.5.1 Speckle interferometer

The setup used to measure the transmission speckle of a multiple scattering sample is shown schematically in fig. 4.5. A cw laser at $\lambda = 532\,\mathrm{nm}$ illuminates the powder sample ($L = 2.2\,\mathrm{mm}$), which was placed in an optical flow cryostat

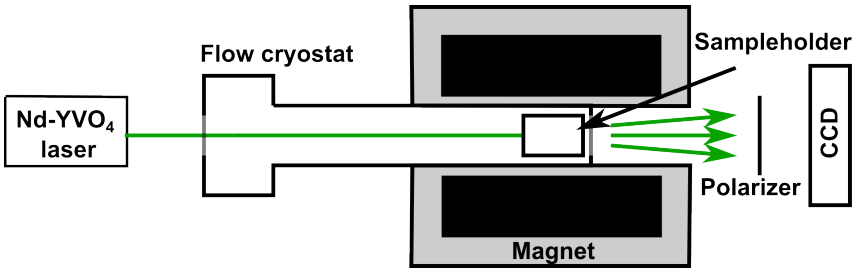


**Figure 4.5:** Speckle interferometer setup: a Nd:$YVO_4$ laser was used to illuminate a powder sample, which was placed in an optical flow cryostat to cool the samples to low temperatures ($T < 10$ K). The cryostat was fixed in a superconducting magnet, which was able to generate a magnetic field up to 7 T. The transmitted light was measured with a CCD camera after passing a linear polarizer.

(The cryostat is described in detail in ref. [29, 30]) to cool it to low temperatures ($T < 10\,\mathrm{K}$). The cryostat was fixed in a superconducting magnet which has a room temperature horizontal bore and generates magnetic fields up to $B = 7\,\mathrm{T}$. The transmitted light was measured with a CCD camera (Apogee Alta U4000, 2048x2048 pixel cooled at $-30$°C, same as in sec. 3.3.1) after passing a linear polarizer which selects one plane of polarization. A measured speckle pattern of a $TiO_2$ (DuPont, R700) sample measured at $T = 10$ K is shown in fig. 4.6. Typical exposure times used are $t_{\mathrm{exp}} = 20 - 60$ s. The exposure was chosen this long to find a balance between low transmission and low incident laser power (P=0.1-0.5 W) to avoid strong heating of the sample in relatively thick, strongly scattering samples.

The histogram in fig. 4.6(b) shows the probability density $P(I)$ of the intensity. Its exponential distribution $P(I) \propto \exp(-I/\langle I\rangle)$ indicates the speckle to originate from an uncorrelated multiple scattering random walk process [122]. Moreover, fig. 4.6(b) shows an offset in the intensity around $\sim 1800$, that is caused by the measurement noise (including observational noise).

On their way through the sample, the photons lose their memory of their incident polarization such that every speckle shows a random but well defined polarization. The shown speckle pattern is the pattern of one plane of polarization. Since light is a vector wave, both independent, perpendicular to each other polarized components of the polarization form this pattern. Both polarization directions can overlap incoherently and must be separated in an experiment by an analyzer to be described by the exponential statistics.

To obtain the correlation function $C(B)$ from the measured speckle image the relative intensity value of each pixel $a_i(t_0) - \langle a_i(t_0)\rangle$ of an image at time $t_0$ with the relative intensity value of each pixel $b_i(t_0 + t) - \langle b_i(t_0 + t)\rangle$ of

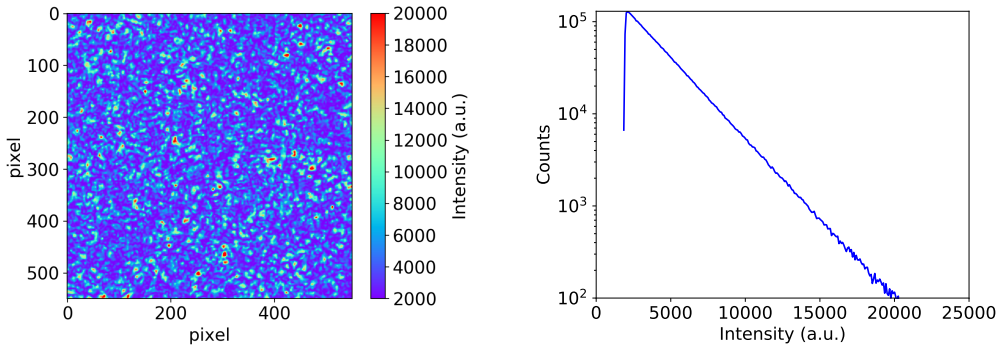


(a) Speckle pattern (b) Histogram

**Figure 4.6:** Illustration of a typical Gaussian speckle pattern: (a) Image section of the transmission speckle observed on a $TiO_2$ powder sample illuminated with a laser of $\lambda = 532$ nm. (b) Histogram of the observed speckle pattern intensity. An exponential decay as predicted for probability density $P(I)$ of uncorrelated photon paths is visible. The offset in intensity around $\sim 1800$ indicates the measurement noise.

an image at time $t_0 + t$ with $t \geq 0$ was multiplied. The sum over all $i$ pixel normalized by the standard deviations of the both images $\sigma_{a,b}$ leads to the intensity correlation function:

$$C(t) = \frac{\sum_i^N (a_i(t_0) - \langle a_i(t_0)\rangle)(b_i(t_0+t) - \langle b_i(t_0+t)\rangle)}{N^2 \sigma_a(t_0)\sigma_b(t_0+t)} \,. \tag{4.24}$$

Knowing the field rate of the magnet (0.23 T/min) allows to obtain the intensity cross-correlation function of the magnetic field $C(B)$.[5] If the speckle does not change, one expects the correlation $C$ to be unity ($C = 1$). For a changing speckle pattern the correlation is $C < 1$.

During my master thesis, the stability of the setup was intensively tested without and with magnetic field [29]. Before each magnetic field run the stability of the speckle was measured during a time as long as the field sweep duration and fitted by a quadratic polynomial. The correlation functions during the field sweeps were then divided by the polynomial to take into account the correlation decay due to the setup instability.

A different speckle interferometer setup is used to characterize the Faraday

[5]Since the magnet shows a hysteresis in $B(t)$ with increasing and decreasing the current, $B(t)$ was fitted and the fit was used to obtain $C(B)$ from $C(t)$.

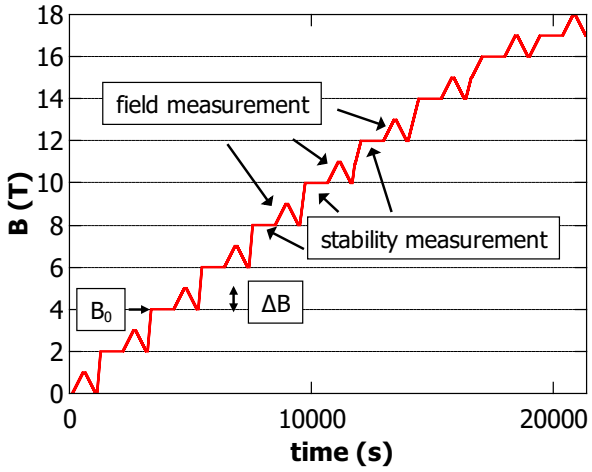


**Figure 4.7:** Scheme of a measurement protocol used to measure speckle correlations in magnetig fields up to $B = 18$ T. Correlations are measured in $\Delta B = 1\,\mathrm{T}$ field steps staring from a field $B_0$. In between each measurement the stability of the setup is checked.

rotation in multiple scattering samples made of $CeF_3$ and glycerol mixtures up to $B = 18\,\mathrm{T}$ and at low temperatures. The measurements are carried out in a superconducting magnet which generates fields up to 18 T (Oxford Instruments) and has a vertical bore (see ref. [36] for details). This increases the instabilities of the measurement. Furthermore, the higher fields require longer times to reach the full magnetic field (18 T) and thus a better stability is necessary. Moreover, larger fields lead to larger forces on the setup and thus to movements. A new measurement protocol is introduced as shown in fig. 4.7 to overcome these stability issues.

The correlations are measured in $\Delta B = 1\,\mathrm{T}$ field steps and not over the whole field range to shorten the measurement time. This also reduces the correlation decay due to movements of the setup in the field. Furthermore, the Faraday rotation of the cryostat windows[6] becomes negligible. For one specific sample and if no saturation of the Faraday rotation is present, the speckle correlation decay should only depend on $\Delta B = B - B_0$ and not on the starting field $B_0$. A saturation effect (as studied with this setup) leads to a weaker correlation decay for a given $\Delta B$ at higher fields $B_0$, and thus to lower $V$ as a result of the fit of eq. (4.17). Therefore, this measurement protocol is very sensitive to such a saturation process.

[6]The Faraday rotation of the cryostat windows was measured to be $V_\mathrm{w} \approx 3°/\mathrm{T}$.

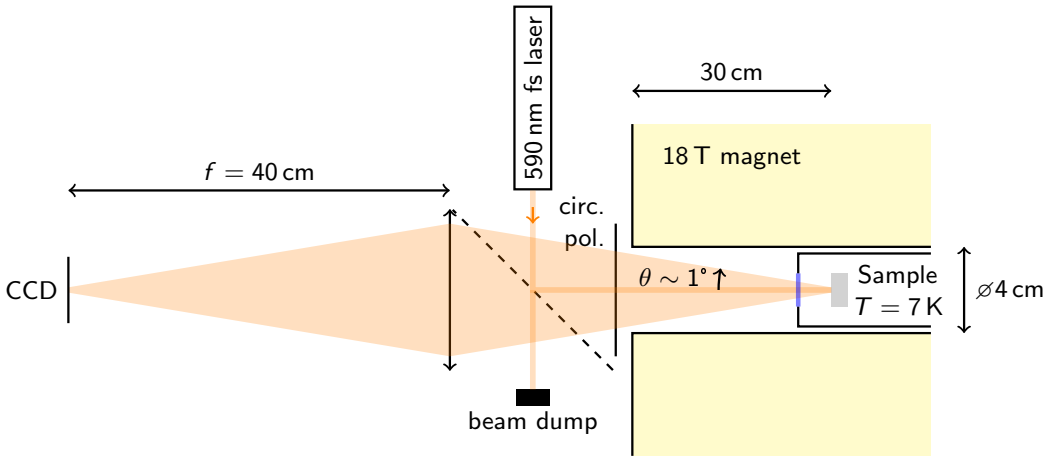


**Figure 4.8:** CBC setup: A laser beam ($\lambda \approx 590\,\mathrm{nm}$) illuminates via a 50:50 beamsplitter a powder sample, which is placed in a flow cryostat. The cryostat is located in a vertical bore 18 T magnet. A circular polarizer blocks single backscattered light. The reflected multiple scattered light is collected in k-space on a CCD via a lens ($f = 400\,\mathrm{mm}$) for scattering angles of up to $\theta \approx 1°$. Figure taken from [81].

### 4.5.2 Coherent backscattering

The principle of the coherent backscattering cone setup was already described in sec. 3.3.1. In the CBC setup used here the sample is placed in a cryostat and this cryostat is put in a high field magnet.[7] This setup is similar to the one in ref. [25]. This time the 18 T superconducting magnet with the vertical room temperature bore is used again. The slab shaped samples were placed with the sample holder inside an optical helium flow cryostat (Oxford instruments) to cool them down to $T \approx 7\,\mathrm{K}$. A beamsplitter underneath the magnet was used to send the light on the sample. A circular polarizer blocks single scattered light and allows for collection of multiple scattered photons in the helicity conserving channel. The reflected light was captured via a lens ($f = 400\,\mathrm{mm}$) and led on a 1900x1200 pixel camera (The Imaging Source, DMK 23UX174) placed in the focal plane of the lens. Figure 4.8 shows the CBC setup.

Since glycerol freezes out at low temperatures the scatterers are fixed in position leading to a static speckle pattern in backscattering. The backscattering cone is recovered by averaging over a large number of these different speckle patterns. This is done by turning the whole helium flow cryostat and tilting

[7] The description of the CBC setup is taken partly from a publication of myself and coworkers [88].

the sample inside the cryostat via piezo elements. The sample was illuminated with a fs-pulsed laser system at 590 nm (frequency doubled OPO pumped by a Ti:Sapphire laser, same as in sec. 2.3.1). The coherence length of this laser is so small that no static interference pattern coming from internal reflections in the cryostat windows and in the beamsplitter occur, and even the sample's speckles are already a little bit averaged.

### 4.5.3 Time of flight

Transport properties such as photon flight times as measured in time of flight distributions might be affected by a destruction of reciprocity via Faraday rotation in highly scattering samples as outlined in sec. 4.1. The setup described in sec. 2.3.1 was merged with the high field magnet ($B = 18$ T) setup to perform ToF measurements of highly scattering powder mixtures of $TiO_2$ and $CeF_3$ (without glycerol to increase the scattering strength). Again the samples were cooled to low temperatures ($T < 10$ K) in a flow cryostat (same as used in the CBC experiments). While in the speckle interferometer setup as well as in the CBC setup, the detectors were CCD cameras, which were not perturbed by the magnetic field when placing them underneath the vertical magnet bore in the experiment, the detector used for the ToF setup, namely the photomultiplier, needed to be shielded by $\mu$-metal foil and placed further away from the magnet. A lens system as sketched in fig. 4.9 is used to guide the light from the sample surface on the detector via a mirror.

## 4.6 Experiments on Faraday rotation in multiple light scattering

The following section is taken in large parts literally from a publication of myself and coworkers [81].

### 4.6.1 Coherent backscattering and reciprocity

A sample consisting of 26 vol% $CeF_3$ and 74 vol% glycerol was prepared to show the destruction of the CBC in a magnetic field. The transport mean free path measured outside the cryostat was $\ell^\star \approx 58.9\,\mu$m, obtained by fitting the CBC with eq. (4.21) with $B = 0$ T and accounting for internal reflections from the sapphire window in front of the sample in the calculation of $R$. The field was then increased in several steps to $B = 18$ T while measuring the cone at every field step. Some of the cones measured are shown in fig. 4.10 (a), where

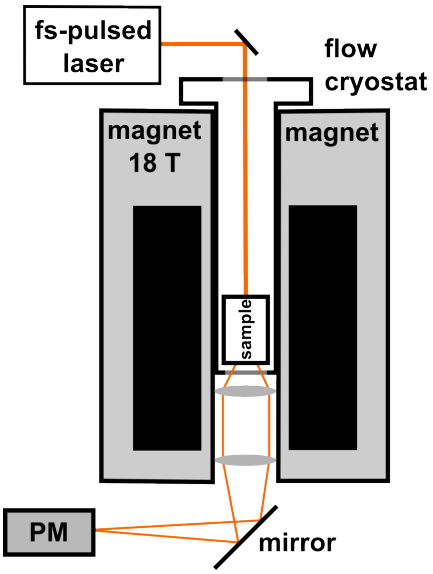


**Figure 4.9:** Time of flight setup in a magnetic field: A pulsed laser (590 nm) illuminates a sample that is placed in an otical flow cryostat. The transmitted light is led via two lenses and a mirror on a Photomultiplier (PM). The detector is shielded with $\mu$-foil and placed far away to avoid perturbations by the magnetic field.

a strong decrease of the enhancement of the CBC is observed with increasing field. For each cone, the enhancement factor was measured by dividing the intensity at $\theta = 0°$ by the mean intensity between 0.4° and 0.5° (where $I(q)$ is already flat, baseline). The measured enhancement at $B = 0\,\mathrm{T}$ is about 1.4, lower than 2 (the theoretical expected value) because of stray light and reflections from the windows of the cryostat. In fig. 4.11 these enhancement factors are plotted (violet curve) against the magnetic field for all measured cones. A parameter $\mathcal{N}$ is introduced to normalize the enhancement at $B = 0$ to 2. Equation (4.21) was used at $q = 0$ to fit the data. Due to the high fields and low temperatures, we are in a regime where the magnetization of $CeF_3$ saturates with increasing field (see fig. 4.14 and 4.15). As described earlier the phase $VB$ is replaced in eq. (4.21) by eq. (4.8) with $\alpha$ the parameter describing the saturation of the Faraday rotation. Because this saturation is only due to $CeF_3$, the bulk value measured in fig. 4.14 is used. Finally, $V_0$ (via $\kappa$) and $\mathcal{N}$ (the enhancement factor normalization parameter) are the two free parameters in eq. (4.21) which is used to fit the data in fig. 4.11 (solid violet line). For this sample a value of $V_0 = \kappa\alpha/T = -1.8 \cdot 10^3\,\mathrm{rad/T \cdot m}$ is obtained, whereas the value calculated from the volume fraction of the particles (using eq. 4.23) is $V_{\mathrm{vol}} = (-1.45 \pm 0.07) \cdot 10^3\,\mathrm{rad/T \cdot m}$.

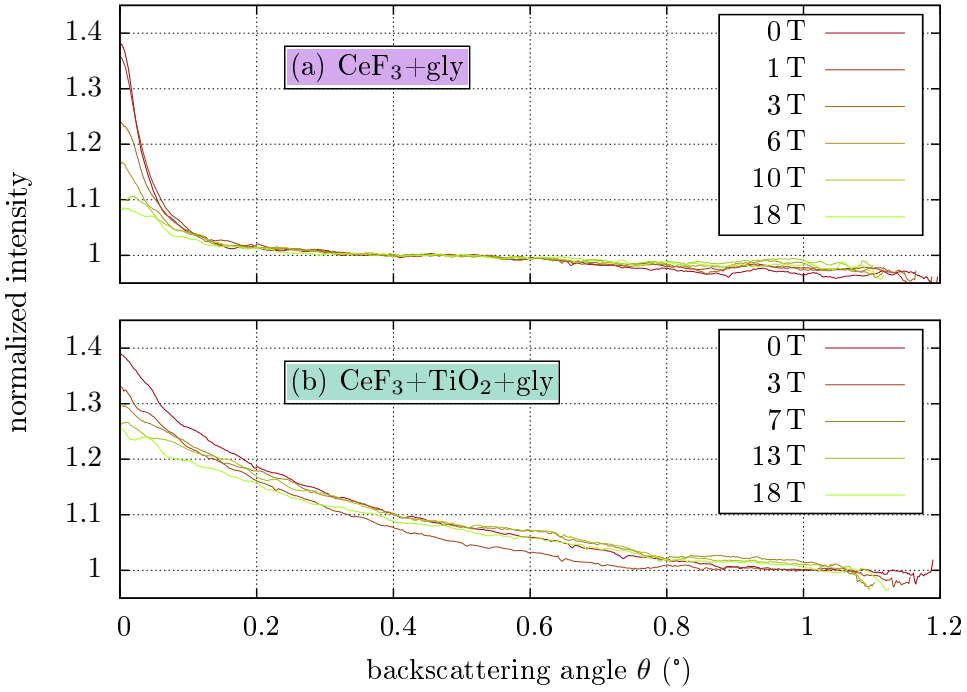


**Figure 4.10:** CBC experiments for different magnetic fields between 0 T and 18 T for a sample consisting of (a) 26 vol% $CeF_3$ powder mixed with glycerol and (b) 26 vol% $CeF_3$ powder mixed with 2 vol% $TiO_2$ powder and glycerol. Experiments were carried out at $T = 7$ K. Cones in (a) are normalized to a baseline between 0.4° and 0.5°. Cones in (b) are normalized to a baseline between 1.0° and 1.1°. Figure same as in [81].

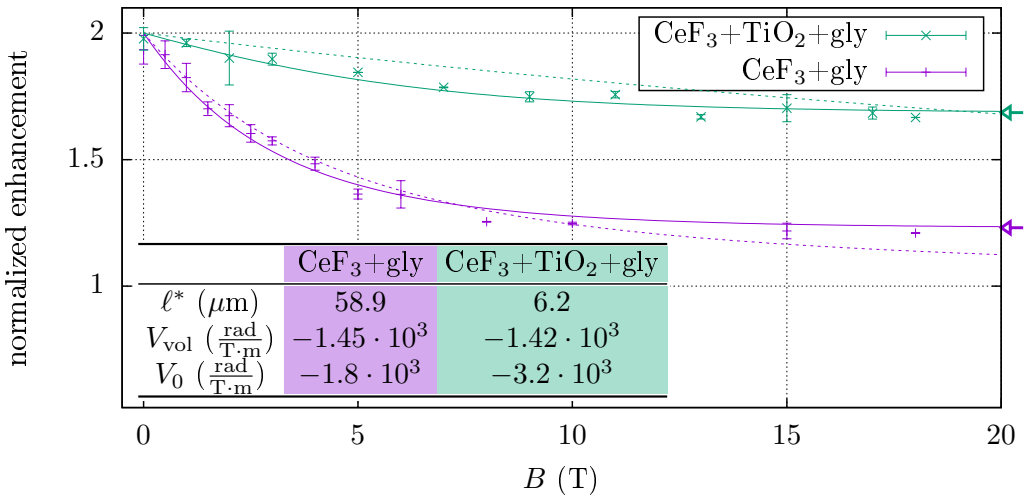


**Figure 4.11:** Destruction of the CBC by a magnetic field: the enhancement $I(q = 0)$ is shown for different field values for $CeF_3$ mixed with glycerol (purple) and $CeF_3$ mixed with $TiO_2$ and glycerol (green). A fit (solid lines) with eq. (4.21) and (4.8) is done to obtain the Verdet constant $V_0$. The data are then normalized by the second fit parameter $\mathcal{N}$ which takes into account that the experimental enhancement factor at $q = 0$ is lower than 2. The arrows on the right side indicate the lower bound of the enhancement factor due to $CeF_3$ saturation. The decays of the CBC tip $I(q = 0)$ expected from the volume fractions of the particles using eq. (4.21) only are plotted as dashed lines for both samples. In both cases $V_{\text{vol}}$ is calculated with 26 vol% $CeF_3$ at a temperature of $T = 7\,\text{K}$. Figure same as in [81].

Mixing about the same amount of $CeF_3$ and glycerol with 2 vol% $TiO_2$ (Aldrich Anatase) leads to lower $\ell^\star$ ($\ell^\star \approx 6.2\,\mu$m compared to the $58.9\,\mu$m of the sample without $TiO_2$). The CBC of this sample are shown in fig. 4.10(b) for different fields. These cones were normalized to a baseline between 1.0° and 1.1°. The destruction of the cone is weaker than for the low scattering sample (green curve of fig. 4.11).

The dashed lines in fig. 4.11 show the expected correlation decay with the respective $\ell^\star$ and $V_{\text{vol}}$ without taking saturation with magnetic field into account (eq. (4.21) only) for both samples. Erbacher *et al.* [112] observed a magnification $E_V = V_0/V_{\text{vol}} > 1$ of the Faraday rotation in multiple scattering samples, which they explain by internal reflections in the Faraday active particles as sketched in fig. 4.4(b). From this the data is expected to appear below the respective dashed curves from the volume fractions. This is the case for low magnetic field, whereas for higher magnetic fields the saturation of the Faraday rotation starts to play a role. Fitting the data of the stronger scattering sample gives a Verdet constant of $V_0 = -3.2 \cdot 10^3\,\text{rad/T} \cdot \text{m}$. For this sample, the value calculated from the volume fraction of the particles is $V_{\text{vol}} = (-1.42 \pm 0.07) \cdot 10^3\,\text{rad/T} \cdot \text{m}$.

The fitted values of $V_0$ (Verdet constant at $B = 0$) are higher than the volume fraction values $V_{\text{vol}}$, in agreement with Erbacher *et al.* [112]. Note that their experiments took place at higher temperatures and lower fields. This was the motivation in this thesis to fit the data with saturation (eq. (4.8)).

Without saturation, it is theoretically possible to destroy the CBC completely (the normalized enhancement factor decreases toward 1 for large magnetic fields if available). However, saturation of the Faraday rotation defines a lower bound to the enhancement factor. Even with arbitrary large magnetic field, the normalized enhancement factor is limited to a lower bound of 1.2 (resp. 1.7) for the weakly (resp. strongly) scattering sample (see arrows in fig. 4.11).

With the measurements shown in this section earlier findings [112, 25] are confirmed that the CBC can be destroyed in high magnetic fields in multiple scattering Faraday active samples. The range of experimental conditions is extended to higher Verdet constants and lower $\ell^\star$. Moreover, the effect of a saturation on the CBC destruction is shown.

### 4.6.2 Transmission speckle correlations

Erbacher *et al.* [112] showed the validity of their model described in sec. 4.3.1 in experiments on milled paramagnetic Faraday glass (FR5 Hoya), with relatively large $\ell^\star \approx 117\,\mu$m values. The powder of Faraday active material was suspended in glycerol or paraffin to overcome speckle stability problems. In

fact, one needs to stabilize the setup to ensure that the correlation decay only comes from the Faraday rotation and not from any vibration or particle displacement. They used a 23.5 T resistive magnet and cooled their samples to $T = 30\,\mathrm{K}$ and $T = 90\,\mathrm{K}$ in a flow cryostat.

In the experiments in this section I use $CeF_3$ and mix it with $TiO_2$ to reach a stronger scattering regime as described in sec. 4.4.2. To overcome any change of the speckle by displacement of the particles in the applied field the particles are embedded in a matrix of glycerol.

To show that $TiO_2$ and glycerol have a negligible Faraday rotation I measured $TiO_2$ in glycerol only (see violet curve in fig. 4.12). The observed decay can be completely accounted for by the Faraday rotation of the cryostat windows, which was measured separately to be $V_\mathrm{w} = (3.00 \pm 0.04)°/\mathrm{T}$. The decay of $C(B) = \cos^2(V_\mathrm{w} B)$ expected from the windows is plotted as a solid violet line in fig. 4.12 (no fit).

A series of measurements of the Verdet constant of Faraday active powder mixtures consisting of $CeF_3$ and $TiO_2$ solved in glycerol was carried out. The amount of $CeF_3$ was raised from 0 vol% to 6.6 vol% in the sample. The correlations of the transmission speckle as function of the magnetic field are plotted in fig. 4.12. The decay gets larger when increasing the amount of $CeF_3$. While the Faraday rotation is dominated by the added amount of $CeF_3$ (see table in fig. 4.12), the scattering behavior scales with the added amount of $TiO_2$ (which was varied between 0 vol% and 6 vol%), as observed in measurements of the diffusion constant via ToF experiments [29]. All fits of the intensity auto-correlation function are shown as solid lines in fig. 4.12. The shown data was reevaluated from [29] to fit increasing and decreasing field data together and account for a hysteresis in the magnetic field sweep behavior. Note further an offset for large fields in the sample with 5.3 vol% and 5.9 vol%. This offset can be explained by a small gradient in the image intensity which does not vanish in the calculation of $C(B)$. The fits were done using eq. (4.17) again replacing $VB$ by eq. (4.8) accounting for a saturation of the Faraday rotation using the bulk value for $\alpha$ (fig. 4.14). Thus, the $B = 0\,\mathrm{T}$ Verdet constant $V_0$ is the only free parameter.

As an example, the sample consisting of 1.9 vol% (16.5 wt%) $TiO_2$ and 6.6 vol% (83.5 wt%) $CeF_3$ solved in 91.5 vol% glycerol is shown as yellow diamonds in fig. 4.12. Its scattering strength ($\ell^\star \approx 6\ \mu\mathrm{m}$) was characterized in a CBC setup (see sec. 3.3.1) separately. The absorption length $L_\mathrm{a} \approx 750\ \mu\mathrm{m}$ was extracted from time of flight experiments (see ref. [29]). The same characterization was done for each sample.

The measured Verdet constants $V_0$ for the different samples (as shown in fig. 4.12) are higher than expected from the volume fractions of $CeF_3$ ($V_\mathrm{vol}$). In

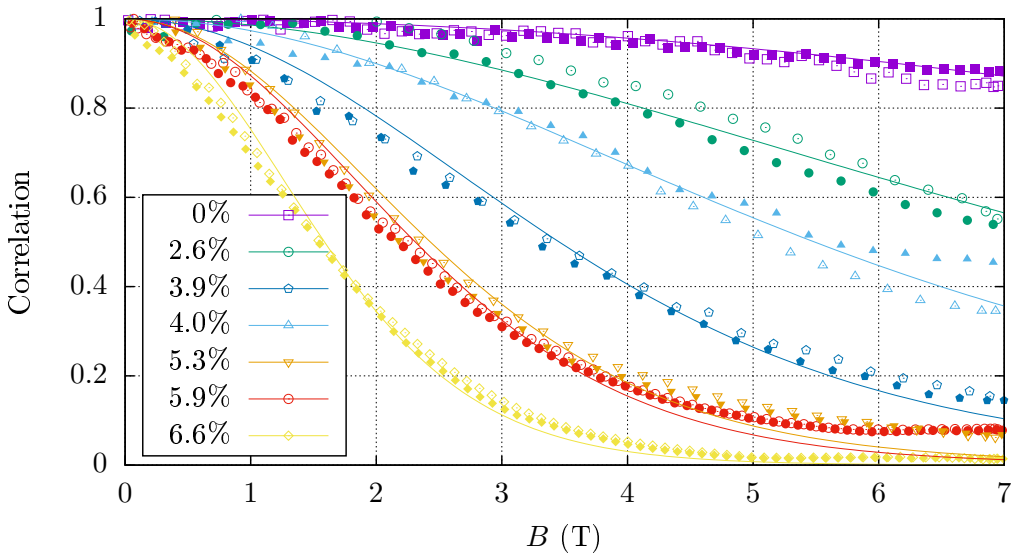


| vol% $CeF_3$ | 0 | 2.6 | 3.9 | 4.0 | 5.3 | 5.9 | 6.6 |
|---|---|---|---|---|---|---|---|
| $V_0$ ($\frac{\text{rad}}{\text{T}\cdot\text{m}}$) | 0 | $249 \pm 3$ | $403 \pm 4$ | $262 \pm 2$ | $496 \pm 5$ | $564 \pm 4$ | $727 \pm 4$ |
| $E_V$ | n/a | 1.8 | 1.8 | 1.2 | 1.6 | 1.7 | 1.9 |

**Figure 4.12:** Correlation decay of the transmission speckle pattern as a function of the magnetic field for different Faraday active powder mixtures solved in glycerol. The amount of $CeF_3$ was raised from 0 vol% to 6.6 vol%. Open symbols: increasing field, correlation with the first image; filled symbols: decreasing field, correlation with the last image. The corresponding fits (eq. (4.17) with eq. (4.8)) with $V_0$ as the only free parameter are plotted as solid lines. In the fits we accounted for the Faraday rotation of the windows, the instability of each measurement and the saturation of the Faraday rotation (see fig. 4.14). For each sample the increasing and decreasing field curves are fitted together. All measurements were carried out at $T = 9\,\text{K}$. Figure same as in [81].

the CBC experiments $V_0$ was also higher than $V_{\text{vol}}$. Both observations strengthen the possible explanation of internal reflections in the Faraday active particles as suggested by Erbacher *et al.* [112]. They obtained values around $E_V = 2.2-2.6$ in their experiments using milled Hoya FR5 ($n = 1.7$) embedded in glycerol. Here $CeF_3$ in glycerol is used, and thus the refractive index mismatch responsible for these internal reflections in the Faraday active particles is smaller. This might explain the smaller $E_V = 1.2 - 1.9$ values.

Nevertheless, with this series of experiments it was possible to show that the Erbacher model can be used to quantify the Faraday effect (via $V_0$) in multiple scattering samples measuring the transmission speckle correlation even for strongly scattering samples if the speckle stability is well controlled.

### 4.6.3 Characterization of the Faraday rotation of $CeF_3$

In this section the speckle correlation technique is used to characterize the Faraday rotation of $CeF_3$ in multiple scattering samples as a function of temperature and field.

#### Temperature dependency

A sample consisting of 3.8 vol% $TiO_2$ and 5.3 vol% $CeF_3$ solved in 90.9 vol% glycerol was measured at 6 K, 9 K, 15 K, 30 K and 72 K to measure the temperature dependency of the Verdet constant of $CeF_3$. This is shown in fig. 4.13. A scattering mean free path of $\ell^\star = 2.3\,\mu$m was measured in a CBC experiment. The correlation curves show an increasing Faraday rotation with lower temperatures as expected from a paramagnetic material. At $T = 72$ K the measurement was less stable due to the high temperature. At this temperature, the cryostat was cooled with liquid nitrogen instead of helium. From the fitted Verdet constant $V_0$ (fig. 4.13(b)) the bulk Verdet constant of $CeF_3$ $V_{CeF_3}$ was extracted by knowing the volume fractions and density of the different materials. $V_{CeF_3}$ is plotted as a function of inverse temperature in fig. 4.13(c). The values are normalized by the value of $E_V$ for the high temperature measurement ($T = 72$ K). For comparison the high temperature dependency of the Verdet constant (between 77 K and 300 K) measured by Leycuras *et al.* [117] is plotted (black crosses, zoom in).

A bulk c-oriented single crystal of $CeF_3$ ($L = 1$ mm from E-Crystal Co., Ltd., Osaka, Japan) was measured to obtain low temperature bulk values of the Faraday rotation of $CeF_3$. A 532 nm cw laser was passed through a polarizer and an analyzer with the bulk crystal plate in between inside the cryostat and the transmitted light was recorded with a photodiode. The magnetic field

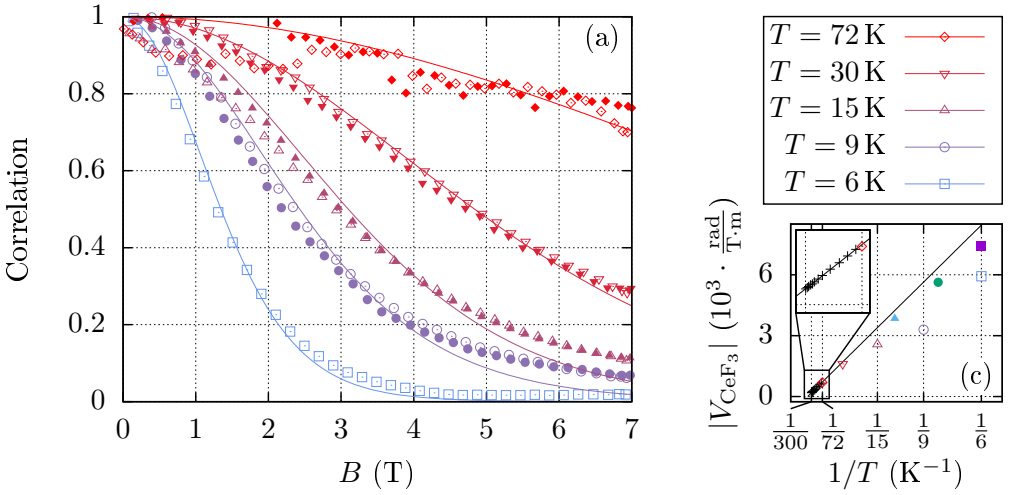


(b)

| $T$ (K) | 6 | 9 | 15 | 30 | 72 |
|---|---|---|---|---|---|
| $V_0$ ($\frac{\text{rad}}{\text{T·m}}$) | $-899 \pm 9$ | $-496 \pm 5$ | $-383 \pm 4$ | $-237 \pm 1$ | $-98 \pm 3$ |

**Figure 4.13:** (a) Correlations of the transmission speckle for a sample consisting of 3.8 vol% $TiO_2$ and 5.3 vol% $CeF_3$ solved in 90.9 vol% glycerol as a function of the magnetic field for different temperatures. Open symbols: increasing field, correlation with the first image; filled symbols: decreasing field, correlation with the last image. (For $T = 6\,\text{K}$, only the measurement with increasing field was evaluated since problems with the cryostat occurred during the decrease of the field.) The decorrelations are fitted (solid lines) as in fig. 4.12. (b) Measured Verdet constant $V_0$ for the different temperatures. (c) Recalculated bulk Verdet constant of $CeF_3$ $V_{CeF_3}$ (using the measured $E_V$ at 72 K for all temperatures) as a function of the inverse temperature (open symbols). For comparison the high temperature dependency of the Verdet constant (between 77 K and 300 K) measured in ref. [117] (black crosses) is plotted and fitted by $V \propto 1/T$ (solid black line) and the low temperature data measured in fig. 4.14 are shown (filled symbols). Figure same as in [81].

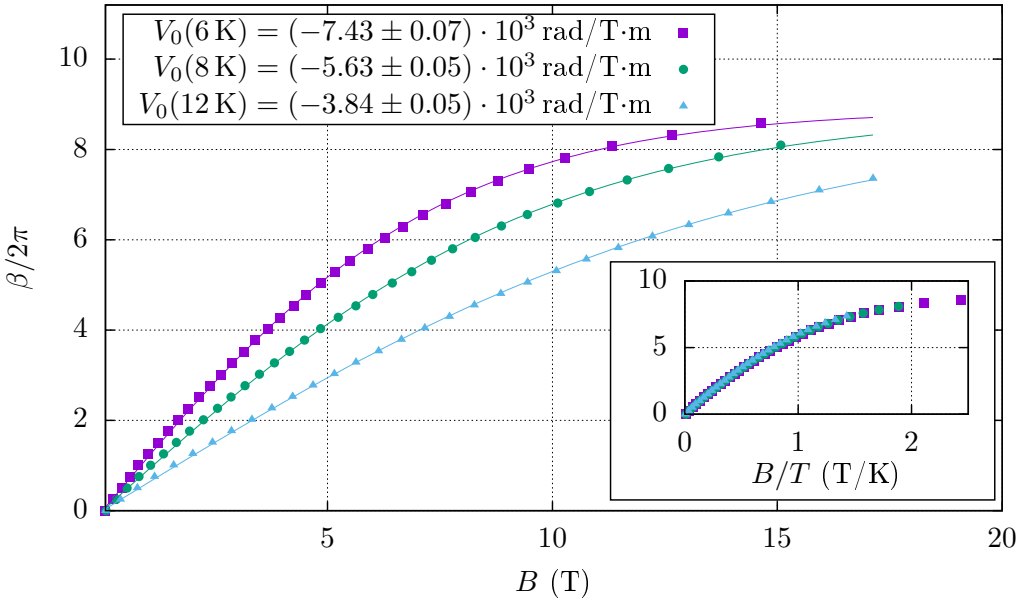


**Figure 4.14:** Faraday rotation angle $\beta$ of a bulk crystal slab shaped sample ($L = 1\,\mathrm{mm}$) as a function of magnetic field at 6, 8 and 12 K. A 532 nm cw laser was used for illumination. The data were fitted with eq. (4.8) to obtain the $B = 0$ bulk Verdet constant $V_0$ and the saturation parameter $\alpha$ (solid lines). For all three temperatures, $\alpha = (0.81 \pm 0.02)\,\mathrm{K/T}$ and $\kappa = (5.57 \pm 0.02) \cdot 10^4\,\mathrm{rad \cdot m^{-1}}$. The inset shows that all the data collapse on a single curve when plotted as a function of $B/T$. The Verdet constant is proportional to the derivative of the curve and shows a saturation for high $B/T$ ratios.

was raised from 0 T to 18 T for temperatures of 6 K, 8 K and 12 K. The rotation angle $\beta$ is plotted in fig. 4.14 versus the applied field. The data is fitted with eq. (4.8) to obtain the bulk Verdet constant $V_0$ for each temperature. The Verdet constant for the three temperatures are plotted in fig. 4.13(c) for comparison. They fall almost on the Leycuras *et al.* [117] data fit ($V_0 \propto \frac{1}{T}$) extrapolated for low temperatures.

### Field dependency

To characterize the Faraday rotation of $CeF_3$ in multiple scattering in high magnetic fields ($B = 18\,\mathrm{T}$) at low temperatures ($T = 8\,\mathrm{K}$ and 9 K) mixtures of $CeF_3$ and glycerol were measured in the high field speckle interferometer using the field step (1 T steps) method introduced at the end of sec. 4.5.1 (see fig. 4.7).

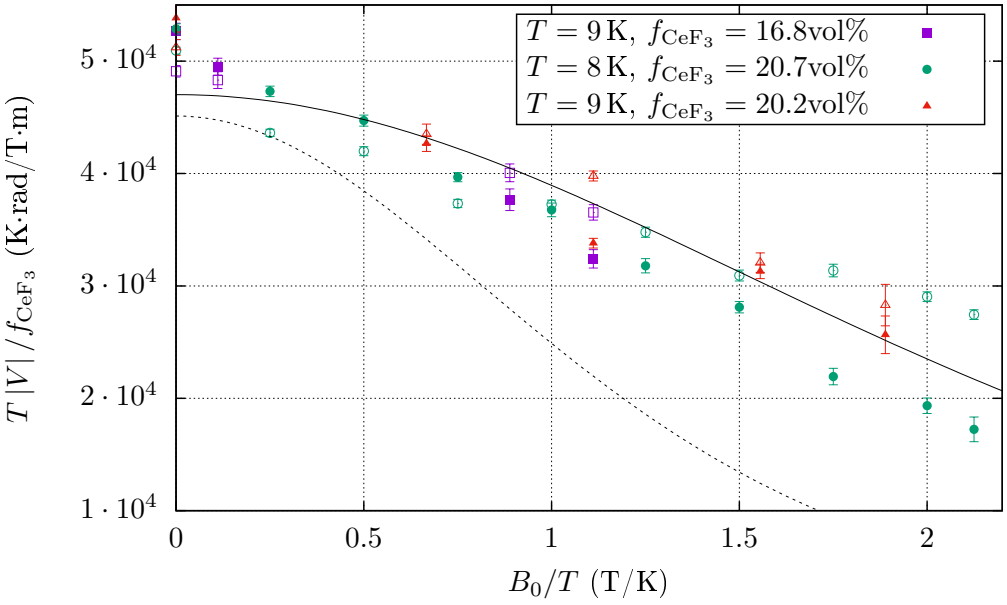


**Figure 4.15:** Measurement of the saturation of the Faraday rotation of $CeF_3$ for three different sample mixtures of $CeF_3$ and glycerol: From correlation measurements such as in fig. 4.12 the Verdet constant $V$ is obtained for different $\Delta B = 1\,\mathrm{T}$ field steps starting at $B_0$. Increasing field (open symbols) and decreasing field (closed symbols). $V$ is multiplied by $T/f_{\mathrm{CeF_3}}$ to fit all data together with eq. 4.7 (solid black line). From the fit we obtained $\kappa\alpha = (4.70 \pm 0.09) \cdot 10^4\,\mathrm{K \cdot rad \cdot T^{-1}m^{-1}}$ and $\alpha = (0.44 \pm 0.02)\,\mathrm{K/T}$. For comparison eq. 4.7 is plotted with the bulk $CeF_3$ values for $\kappa$ and $\alpha$ (dashed black line). Figure same as in [81].

The Verdet constant $V$ was measured via the correlation decay for three samples with different filling fraction of $CeF_3$ ($f_{\mathrm{CeF_3}} = 16.8\,\mathrm{vol\%}$ at $T = 9\,\mathrm{K}$, $f_{\mathrm{CeF_3}} = 20.7\,\mathrm{vol\%}$ at $T = 8\,\mathrm{K}$ and $f_{\mathrm{CeF_3}} = 20.2\,\mathrm{vol\%}$ at $T = 9\,\mathrm{K}$). The absolute value of $V$ was normalized with $f_{\mathrm{CeF_3}}$ and multiplied by the temperature $T$ to compare the different measurements. This value now equals $\kappa\alpha$ from eq. (4.7). The data are plotted in fig. 4.15 against the starting field $B_0$ of the field steps normalized by the temperature $T$. Note that the data overlay (within errors) although they were measured for somewhat different filling fractions and at different temperatures. The normalized Verdet coefficient clearly decreases for higher fields. First of all, this indicates a saturation process. But even for high fields ($B_0/T > 1.5\ \mathrm{T/K}$) a decay of the correlation is still visible. Thus higher fields still lead to an enhanced Faraday rotation and it is worth to raise the field to $B = 18\,\mathrm{T}$ to destroy reciprocity on even smaller paths in

the used setup. The data are fitted with eq. (4.7) (solid black line) to obtain the material dependent constant $\kappa\alpha = (4.70 \pm 0.09) \cdot 10^4\,\mathrm{K \cdot rad \cdot T^{-1}m^{-1}}$. Further eq. (4.7) is plotted using the bulk $CeF_3$ values for $\kappa$ and $\alpha$ measured in fig. 4.14 (black dashed line). Again, the experimental value is larger than the bulk value, consistent with Erbacher *et al.* [112]. Note that the material constant $\alpha = (0.44 \pm 0.02)\,\mathrm{K/T}$ responsible for the field saturation is smaller than the bulk value $(0.81 \pm 0.02)\,\mathrm{K/T}$. This discrepancy would need further investigation. Nevertheless, the bulk and multiple scattering data are still in qualitative agreement.

Figure 4.11, 4.14 and 4.15 show the first quantification of the Faraday rotation of $CeF_3$ up to 18 T at low temperature. A decrease of the Verdet constant for large magnetic field to temperature ratios, and thus a saturation of the Faraday rotation of $CeF_3$ is observed.

## 4.7 A method to manipulate Anderson localization in magnetic fields

In the latter section the Faraday rotation of $CeF_3$ down to $T = 6\,\mathrm{K}$ and up to $B = 18\,\mathrm{T}$ was characterized. Moreover, it was shown that $CeF_3$ can be used as a potential material to increase the Faraday effect in strongly scattering samples. By mixing it with higher refractive index materials (e.g. $TiO_2$) it might be a candidate to manipulate reciprocity in localizing samples if they are found.

Although the CBC is a direct measure of the coherent part of the light in multiple scattering samples and reciprocity can be easily accessed, destruction of the cone cannot be realized in strongly scattering samples $kl^* < 10$ with $CeF_3$ using the available setup. Close to the mobility edge of Anderson localization, the samples have an even higher scattering strength. This means that in order to quantify the strength of Faraday rotation and to reach the breakdown of reciprocity in such samples in backscattering geometry, materials with a higher Verdet constant or a setup in stronger fields would be necessary.

Thus an alternative method, the correlation measurement of the transmission speckle, which allows a characterization of the Faraday rotation also in stronger scattering powders was presented. The question whether a breakdown of reciprocity (as an interesting application for manipulation of Anderson localization) can be associated with the destruction of the speckle correlation in transmission remains open. One could argue that only photons traveling on reciprocal paths which fit inside the sample of size $L$ may localize (if the

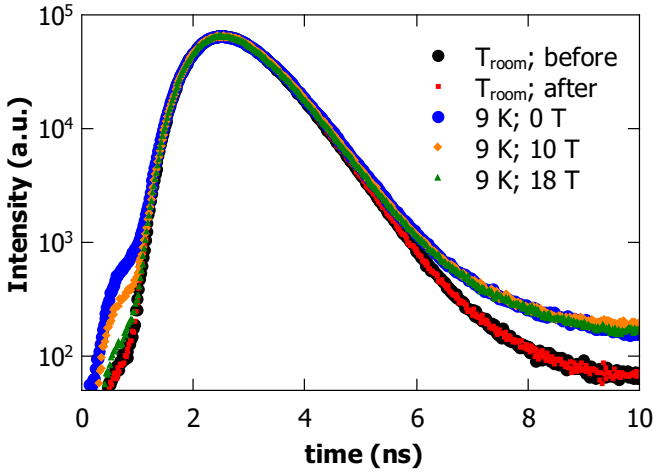


**Figure 4.16:** Time of flight measurements of a sample ($L$ = 1.02 mm, $L_a$ = 86.6 $\mu$m, $\ell^\star$ = 307 nm) made of a powder mixture of R700 and 5.6 vol% $CeF_3$. The same sample was measured at room temperature before (black circles) and after (red squares) cooling the sample to $T$ = 9 K and measuring the ToF at $B$ = 0 T (blue circles), $B$ = 10 T (orange diamonds) and $B$ = 18 T (green up triangles).

localization length is smaller than or comparable to $L$). Transmission speckle patterns are governed by similar path lenghts (of order $L^2/\ell^*$). Thus, a breakdown of reciprocity in the helicity conserving channel might be expected to occur when the speckle correlation in transmission geometry has decayed. If potentially localizing samples are found, time of flight experiments in high magnetic fields can be used to distinguish between Anderson localization and other effects such as absorption and fluorescence.

ToF measurements in high magnetic fields in the setup described in sec. 4.5.3 are performed to check the strongest scattering available samples in this thesis (namely $TiO_2$ powder R700 from DuPont) for signs of localization and show a proof of principle experiment. A complete destruction of the speckle correlation in transmission can be achieved in powder mixtures of $TiO_2$ with $\sim$ 5 vol% $CeF_3$ for samples of $L \approx 1$ mm at $B$ = 18 T (see ref. [29]). This should also effect reciprocity and thus Anderson localization on long scattering paths. Here a R700 powder sample with 5.6 vol% $CeF_3$ ($L$ = 1.02 mm, $L_a$ = 86 $\mu$m, $\ell^\star$ = 307 nm) is prepared to test this idea in relatively strong scattering samples of $TiO_2$. Figure 4.16 shows different ToF measurements of this sample. The ToF is measured at room temperature before (black circles) and after (red squares) the magnetic field experiment. These curves overlap very

well. The same sample is measured at $T \approx 9$ K for three different field strength $B = 0$ T, 10 T and 18 T. Here the long-time tail increases in respect to the room temperature measurement. This might come from a temperature dependency of the absorption/fluorescent process. Note further the optical shortcut that occurred when cooling the sample at short times. This can occur when a crack/hole in the sample is present. Such a crack/hole might open up during cooling. It disappears after heating the sample back to room temperature. No effect of the magnetic field is observed in the three low temperature curves. This observation strengthens the results of sec. 2.5 that no localization effects are observed in the commercial $TiO_2$ powders, also confirmed by a similar experiment on the same materials by ref. [36]. Both experiments question an earlier observation by M. Störzer [27] where a change of the ToF curve with magnetic field in powder mixtures of $TiO_2$ and $CeF_3$ was seen.

Let me conclude here that the same experiments should be repeated if signs of localization are found in highly scattering and also Faraday active samples. As mentioned in sec. 2.2.3 localization inherently exists in lower dimensional systems. In the following chapter I use this idea to test the effect of magneto-optical Faraday rotation on Anderson localization of light.

# Chapter 5

# Lower dimensional light transport

A certain amount of disorder, as stated by the *Ioffe-Regel* criterion, is required to achieve light localization in 3D random media while in lower dimensions localization can (theoretically) always be realized for large enough system size $L \gg \xi$ (see sec. 2.2.3). A detailed summary of Anderson localization in different dimensional systems can be found in ref. [123]. In two dimensions experimental studies are still challenging and difficult to realize, partly due to the exponential scaling of the localization length with the disorder parameter $k\ell^\star$. Nevertheless, such experiments were realized for different kinds of waves (e.g. for light [124] or ultracold atoms [125]). One dimensional light localization can easier be realized (here the localization length scales linear with the disorder) either in confined geometry (microwaves in a waveguide [126] or optical fibers [127]) or open systems such as in a stack of glass slides [128]. Here the geometry becomes quasi 1D (Q1D) as a propagation in the transverse dimensions is present [129].

In this chapter such a stack of glass slides will be studied further. A stack of $N \gg 1$ transparent plates of varying thickness can act as a mirror due to the strongly suppressed transmission for coherent waves. A correct analytic treatment of coherent waves, which will be discussed at first, leads to an exponential decay of transmission with increasing number of slides (averaged over different configurations of disorder) and can be connected to localization. A suppression of transmission in the localized regime is also connected to a narrowing of the modes of oscillation of the waves. This leads to enhanced fluctuations of the transmission. Chabanov *et al.* [130] noted that the exponential decay of the transmission with sample thickness is not clearly distinguishable from absorption (similar to the 3D case) and that absorption may even suppress localization. Moreover, it is difficult to realize a sufficiently large set of configurations when averaging over them to obtain the mean transmission quantity. Thus, Genack *et al.* [131] show measurements of the variance of the relative transmitted intensity as a quantity for transmission fluctuations to observe localization in their samples even in the presence of absorption. In their

experiments they send microwaves through a Q1D sample made of randomly arranged aluminum spheres in a long copper tube and measure the frequency resolved transmission. Park *et al.* [129] study localization via transmitted intensity statistics in the presence of a crossover from a 1D to a Q1D system sending visible light through a stack of glass slides. Their system is experimentally simple to realize but the Q1D geometry might lower/suppress localization. In their study they introduce a localization threshold in the variance of the relative transmitted intensity that can be used to distinguish between localization and diffusion via photon statistics. Their theory will be introduced after explaining the propagation of coherent light in a stack of glass slides.

The importance of the interference of multiple reflections that lead the observation of an exponential decay in transmission can be studied if the phases of the waves are manipulated e.g. via the Faraday effect, as shown in the latter chapter for a 3D system. Bromberg *et al.* [132] showed the manipulation of reciprocity in a CBC experiment (weak localization) in a 1D system using an optical fiber setup. In this chapter I will use strong Faraday active glass slides as a Q1D multiple scattering sample similar to ref. [129] to study the manipulation of localization via magnetic fields in measurements of the transmission and its fluctuations. In transfer matrix simulations a perfect 1D glass stack with the same experimental parameters will be investigated including Faraday rotation and compared to the experimental Q1D data.

## Contents

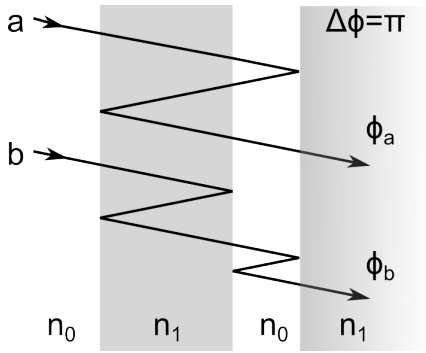


**Figure 5.1:** Multiple scattering through a stack of glass slides: Two different photons a and b on paths of the same length collect a phase shift of $\Delta\phi = \phi_b - \phi_a = \pi$ on their way through the sample.

## 5.1 Transport through a stack of glass slides

Berry and Klein [128] treat the transmission of light waves trough a stack of $N$ glass slides theoretically and confirm their results by a simple experimental study. In their publication they start with an incoherent treatment of the waves and find a $1/N$ dependency for the transmission scaling. For a coherent (and thus correct) calculation which multiplies amplitudes and not intensities and accounts for the waves' phases, the result is an exponential decay of transmission with $N$. In their result the transmission through $N$ plates only depends on the transmission $\tau$ of a single interface. In this calculation an averaging over random phases is done since the plates and air gaps vary in thickness (which gives the system its randomness). This averaging is different from assuming the waves as incoherent since in this averaging process there can be different paths of the same length involved which take different ways through the sample as shown in fig. 5.1. They contribute coherently to the wave amplitude. The two shown paths a and b will collect a phase difference of $\Delta\phi = \pi$ due to the difference in number of reflections at an air-glass interface and thus cancel out in transmission by destructive interference. In fact, the dependency of the coherent transmission through a stack on $N$ glass slides on the transmission of one single air-glass surface $\tau$ only, reflects the cancellation of all multiple reflections by destructive interference.

### 5.1.1 Static transmission

More explicitly the transmission amplitude through a surface between index $n_0$ and $n_1$ was calculated in eq. (3.3) via Fresnel's equations. Reference [128] calculates the transmission amplitude of one glass slide $T_{12}$ via the transmission amplitude $T_1$ of the first surface and $T_2$ of the second surface by the coherent sum of all multiple reflected and transmitted waves:

$$T_{12} = T_1 T_2 + T_1 R_1 R_2 T_2 + ... \tag{5.1}$$

$$= \frac{T_1 T_2}{1 - R_1 R_2} \tag{5.2}$$

The naive ray theory considers all waves as incoherent, such that all amplitudes can be replaced by intensities:

$$\tau_{12} = \frac{\tau_1 \tau_2}{1 - \rho_1 \rho_2} \tag{5.3}$$

For a stack of $2N$ faces this formula can now be applied iteratively and one yields a transmission:

$$\tau_{\text{incoherent}} = \frac{\tau}{\tau + 2N(1 - \tau)} \tag{5.4}$$

Here transparent plates with no loss were assumed such that $\tau + \rho = 1$. In the coherent wave theory the transmission amplitudes in eq. (5.2) need to be replaced by the wave expression in a medium with index $n_j$ as $T_\text{j}/\sqrt{n_\text{j}} \exp(ikn_\text{j}x)$ and similarly for $R_\text{j}$. Because the plates have varying thickness and the distance between the plates can vary randomly, the quantities have random phases and one needs to average over them.[1] The average of any function $f$ of the transmitted intensity over the random phases can then be expressed as follows:

$$\langle f(|T_{12}|^2) \rangle = \frac{1}{2\pi} \int_0^{2\pi} d\phi f \left( \frac{|T_1|^2 |T_2|^2}{|1 - |R_1 R_2| \exp(i\phi)|^2 |^2} \right) \tag{5.5}$$

Choosing $f(u) = \ln(u)$ [133] to decouple the second from the first face [134] and by assuming $|R_1 R_2| < 1$ the integral in the denominator vanishes and one obtains:

$$\langle \ln(|T_{12}|^2) \rangle = \ln(|T_1|^2) + \ln(|T_2|^2) \tag{5.6}$$

[1] The condition for the phases to be uniformly distributed modulo $2\pi$ is that the variation of the gap thickness is $\Delta d \gg \lambda / 2n_0$.

For 2N faces an iterative calculation yields

$$\tau_{\text{coherent}} = \exp\left(\langle \ln(|T_{12}|^2)\rangle\right) = \exp\left(\sum_{s=1}^{2N} \ln \tau_s\right) \tag{5.7}$$

$$= \exp\left(-2N \ln(\frac{1}{\tau})\right) \ . \tag{5.8}$$

This result for the exact effective transmission is the same as expected when all multiple reflections are ignored and only the transmissions of each interface are multiplied $\tau_{\text{coherent}} = \tau^{2N}$, which can be understood as an exact cancellation of all the other terms via interference. From eq. (5.8) a localization length of $\xi = (\ln(1/\tau))^{-1}$ in number of surfaces can be obtained.

### 5.1.2 Transmission fluctuations and photon statistics

Transmission fluctuations have been studied via measurements of the probability density of intensity relative to its average value $P(I/\langle I\rangle)$ in a random ensemble of sample configurations in Q1D samples [135, 136, 130, 129]. For a large number of statistically uncorrelated contributions to the field the probability distribution for one plane of polarization can be expressed as [136]

$$P(I/\langle I\rangle) = \exp(-I/\langle I\rangle) \ , \tag{5.9}$$

in the diffusive 1D limit $L \ll \xi, L_{\text{a}}$. In Q1D geometry this expression holds for a single sample configuration where the average intensity over the output surface relative to the ensemble average is $\bar{I}/\langle I\rangle$, also named relative total transmission. With this the probability distribution in Q1D can be expressed as [129]

$$P(I/\langle I\rangle) = \int_0^\infty \exp(-I/\bar{I}) P(\bar{I}/\langle I\rangle) \mathrm{d}\bar{I}/\bar{I} \ . \tag{5.10}$$

In Q1D the mesoscopic function $P(\bar{I}/\langle I\rangle$ depends on the variance of $\bar{I}/\langle I\rangle$ only. Chabanov *et al.* [130] show a relation between the variance of the normalized transmission $\text{var}(\bar{I}/\langle I\rangle)$ to the variance of the normalized intensity $\text{var}(I/\langle I\rangle)$

$$\text{var}(I/\langle I\rangle) = 2\text{var}(\bar{I}/\langle I\rangle) + 1 \ . \tag{5.11}$$

Note that $P(I/\langle I\rangle)$ becomes a function of $\text{var}(I/\langle I\rangle)$. In the diffusive limit for low absorbing samples they relate the average transport (here the di-

mensionless conductance $\langle g \rangle$ which is equivalent to the optical transmittance $\langle \tau \rangle = \langle I \rangle / I_0$ with $I_0$ the incident intensity) to its fluctuations via $\mathrm{var}(\bar{I}/\langle I \rangle) = 2/(3\langle g \rangle)$. In a localized regime the narrow modes of oscillation and corresponding sharp, widely spaced peaks in transmission as observed by Park *et al.* [129], would lead to large values of $\mathrm{var}(\bar{I}/\langle I \rangle)$. Knowing that the localization threshold for the dimensionless conductance is $\langle g \rangle = 1$, Park *et al.* [129] find a threshold parameter for the intensity fluctuations to distinguish between diffusion and localization:

$$\mathrm{var}(I/\langle I \rangle) = \frac{4}{3\langle g \rangle} + 1 = \frac{7}{3} \; . \tag{5.12}$$

This universal threshold can now be used to look for localization in the variation of $P(I/\langle I \rangle)$ with increasing system size $L$. In a stack on $N$ glass slides the crossover from 1D to Q1D counteracts localization in the sense that the saturation value of the fluctuations in Q1D (and thus the corresponding length $\ell_{1D \to Q1D}$) can be lower than this threshold (the localization length $\xi$) which would lead to a suppression of localization.

In the last sections it was shown that the mean transmission as well as its fluctuations can be used to search for signs of localization. Similar to the 3D case the magneto-optical Faraday effect can be used to test such signs of localization for its origin in magnetic fields using Faraday active scattering materials. This idea should be emphasized in the following section.

### 5.1.3 Transfer matrix and Faraday rotation

Using the magneto-optical Faraday effect, the phase of a wave can be changed and destructive interference on multiple scattering paths leading to suppressed transmission in the localized regime can be effected. Here this idea should be tested on a 1D system. More concrete, this effect can be used to test for the origin of signs of localization such as the exponential transmission scaling with sample size as well as enhanced fluctuations of this quantity in a potentially localized regime. Therefore, 1D light transport is studied using transfer matrix calculations including Faraday rotation. The formalism presented in the following section was developed and used by my colleague G. J. Aubry to numerically calculate the propagation of an electromagnetic wave through a stack of $2N$ interfaces with and without Faraday rotation (unpublished). Here the formalism and the results of these calculations are introduced to compare them to the performed experiments.

The propagation of an electromagnetic wave through a stack of $2N$ interfaces

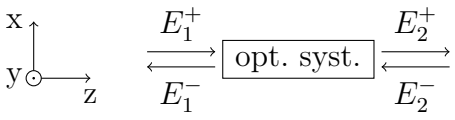


**Figure 5.2:** Geometry of the electromagnetic fields $E$ before (1) and after (2) any optical system (dielectrics, interface, ...).

can be described using a transfer matrix approach. Given any optical system (see figure 5.2 for the geometry), the transfer matrix formalism decomposes the field in plane waves propagating in the $+z$ and $-z$ directions, and relates the field after the system to the field before the system through the transfer matrix $\mathcal{M}$

$$\begin{pmatrix} E_2^+ \\ E_2^- \end{pmatrix} = \mathcal{M} \begin{pmatrix} E_1^+ \\ E_1^- \end{pmatrix}. \tag{5.13}$$

Let us recall that a plane wave in a homogeneous medium of index $n$ can be written as:

$$E(z,t) = E \exp[i\,(\omega t - kz)]\ , \tag{5.14}$$

with $k > 0$ for a wave propagating in the $+z$ direction, and $k < 0$ for a wave propagation in the $-z$ direction. For instance, if light (wavelength in vacuum $\lambda_0$) propagates on a distance $d$ in a dielectric having a refractive index $n$, the transfer matrix is

$$M_d = \begin{pmatrix} \exp -\frac{2\mathrm{i}\pi n d}{\lambda_0} & 0 \\ 0 & \exp \frac{2\mathrm{i}\pi n d}{\lambda_0} \end{pmatrix}. \tag{5.15}$$

If the system is an interface between two dielectrics $n_1$ and $n_2$ perpendicular to the wave vector, the Fresnel formula allow to write the transfer matrix of the interface

$$N_{n_1 \to n_2} = \frac{1}{2n_2} \begin{pmatrix} n_2 + n_1 & n_2 - n_1 \\ n_2 - n_1 & n_2 + n_1 \end{pmatrix}. \tag{5.16}$$

The transfer matrix of a dielectric slab of refractive index $n$ and thickness $d$ placed in air ($n_0$) is then written as the matrix product $N_{n \to n_0} \times M_d \times N_{n_0 \to n}$.

Faraday rotation, which is a kind of circular dichroism, imposes to split the field in the two circular polarization components $E^{+/-} = \left(E^{\mathrm{R}+/-}, E^{\mathrm{L}+/-}\right)$. In a Faraday active material, these components are related to each other by a

$4 \times 4$ matrix $M_{\mathrm{FR}}$

$$\begin{pmatrix} E_d^{\mathrm{R}+} \\ E_d^{\mathrm{L}+} \\ E_d^{\mathrm{R}-} \\ E_d^{\mathrm{L}-} \end{pmatrix} = M_{\mathrm{FR}}(d, \Delta n) \begin{pmatrix} E_0^{\mathrm{R}+} \\ E_0^{\mathrm{L}+} \\ E_0^{\mathrm{R}-} \\ E_0^{\mathrm{L}-} \end{pmatrix}, \tag{5.17}$$

$$M_{\mathrm{FR}} = \begin{pmatrix} \exp -\mathrm{i}n_+\varphi & 0 & 0 & 0 \\ 0 & \exp -\mathrm{i}n_-\varphi & 0 & 0 \\ 0 & 0 & \exp \mathrm{i}n_+\varphi & 0 \\ 0 & 0 & 0 & \exp \mathrm{i}n_-\varphi \end{pmatrix}, \tag{5.18}$$

with $n_\pm = n \pm \Delta n$ and $\varphi = \frac{2\pi d}{\lambda_0}$. Here $2\Delta n$ is the refractive index difference for right and left circular polarized waves, and is related to the Verdet constant $V$ of the Faraday active material and to the applied magnetic field $B$ via $\Delta n = \frac{\lambda_0 B V}{2\pi}$. Note that a very similar matrix $M_{\mathrm{OA}}$ can be written for optical activity (which does not break reciprocity),

$$M_{\mathrm{OA}} = \begin{pmatrix} \exp -\mathrm{i}n_+\varphi & 0 & 0 & 0 \\ 0 & \exp -\mathrm{i}n_-\varphi & 0 & 0 \\ 0 & 0 & \exp \mathrm{i}n_-\varphi & 0 \\ 0 & 0 & 0 & \exp \mathrm{i}n_+\varphi \end{pmatrix}. \tag{5.19}$$

In this (circular) basis, the transfer matrix of an interface between air ($n_0$) and a Faraday active material is written

$$N_{n_0 \to n_+, n_-} = \frac{1}{2} \begin{pmatrix} \frac{n_0+n_+}{n_+} & 0 & 0 & \frac{n_+-n_0}{n_+} \\ 0 & \frac{n_0+n_-}{n_-} & \frac{n_--n_0}{n_-} & 0 \\ 0 & \frac{n_--n_0}{n_-} & \frac{n_0+n_-}{n_-} & 0 \\ \frac{n_+-n_0}{n_+} & 0 & 0 & \frac{n_0+n_+}{n_+} \end{pmatrix} \tag{5.20}$$

and the transfer matrix of an interface between a Faraday active material and air is written

$$N_{n_+, n_- \to n_0} = \frac{1}{2n_0} \begin{pmatrix} n_0+n_+ & 0 & 0 & n_0-n_+ \\ 0 & n_0+n_- & n_0-n_- & 0 \\ 0 & n_0-n_- & n_0+n_- & 0 \\ n_0-n_+ & 0 & 0 & n_0+n_+ \end{pmatrix} \tag{5.21}$$

In the experiments I worked with a linear polarized incoming field $E_0^+ =$

$\begin{pmatrix} E_0^{x+} \\ E_0^{y+} \end{pmatrix}$ such that we start the calculations in the linear basis. Changing from the circular to the linear basis (and vice versa) can be done using the matrices for the basis change $P_{\text{circ}\to\text{lin}}$ and $P_{\text{lin}\to\text{circ}}$ as calculated in the following. For propagation in $+z$ direction and respectively for $-z$ direction the fields in the circular basis can be expressed as

$$\begin{cases} E^{\text{R}+} = \frac{1}{\sqrt{2}} \left(E^{x+} + iE^{y+}\right) \\ E^{\text{L}+} = \frac{1}{\sqrt{2}} \left(E^{x+} - iE^{y+}\right) \\ E^{\text{R}-} = \frac{1}{\sqrt{2}} \left(E^{x-} - iE^{y-}\right) \\ E^{\text{L}-} = \frac{1}{\sqrt{2}} \left(E^{x-} + iE^{y-}\right) \end{cases} .$$

With this, the matrix for the basis change between linear $\begin{pmatrix} E^{x+} \\ E^{y+} \\ E^{x-} \\ E^{y-} \end{pmatrix}$ and circular $\begin{pmatrix} E^{\text{R}+} \\ E^{\text{L}+} \\ E^{\text{R}-} \\ E^{\text{L}-} \end{pmatrix}$ polarized fields can be calculated:

$$P_{\text{circ}\to\text{lin}} = \frac{1}{\sqrt{2}} \begin{pmatrix} 1 & 1 & 0 & 0 \\ i & -i & 0 & 0 \\ 0 & 0 & 1 & 1 \\ 0 & 0 & -i & i \end{pmatrix}$$

$$P_{\text{lin}\to\text{circ}} = \frac{1}{\sqrt{2}} \begin{pmatrix} 1 & -i & 0 & 0 \\ 1 & i & 0 & 0 \\ 0 & 0 & 1 & i \\ 0 & 0 & 1 & -i \end{pmatrix}$$

Without any loss of generality let us consider a $x$-polarized incident wave. This implies $E_0^{y+} = 0$. Having just a light source before the system, the field after the system is connected via the transfer matrix $\mathcal{M}$ to the field before the system

$$\begin{pmatrix} E_N^{x+} \\ E_N^{y+} \\ 0 \\ 0 \end{pmatrix} = \mathcal{M} \begin{pmatrix} E_0^{x+} \\ 0 \\ E_0^{x-} \\ E_0^{y-} \end{pmatrix} \tag{5.22}$$

with $E_0^- = \begin{pmatrix} E_0^{x-} \\ E_0^{y-} \end{pmatrix}$ the field reflected by the system. Note that there is no field in $-z$ direction after the system and therefore $E_N^{x-} = E_N^{y-} = 0$. The overall transfer matrix $\mathcal{M}$ that connects the incoming and the outgoing fields through a stack of $N$ Faraday active slides of thicknesses $\{d_i\}$ separated by $N-1$ air gaps of thicknesses $\{e_i\}$ in the linear basis is then expressed by

$$\begin{aligned}\mathcal{M} =& P_{\text{circ}\to\text{lin}} \times \\ & \prod_{i=N}^{2} [N_{n_R,n_L\to n_0} M_{\text{FR}}(d_i, \Delta n) N_{n_0\to n_R,n_L} M_0(e_i)] \\ & \times N_{n_R,n_L\to n_0} M_{\text{FR}}(d_1, \Delta n) N_{n_0\to n_R,n_L} \\ & \times P_{\text{lin}\to\text{circ}}, \end{aligned} \tag{5.23}$$

$M_0(e_i)$ being the transfer matrix of an air gap.

Knowing $\mathcal{M}$, the system (5.22) has four equations and four unknown ($E_0^{x-}$, $E_0^{y-}$, $E_N^{x+}$ and $E_N^{y+}$) and can therefore be solved analytically. Writing $\mathcal{M} = (m_{ij})_{0\le i,j<4}$ using its matrix elements, the solution is:

$$\begin{cases} E_0^{x-} &= E_0^{x+} \cdot \frac{-m_{20}m_{33}+m_{23}m_{30}}{m_{22}m_{33}-m_{23}m_{32}} \\ E_0^{y-} &= E_0^{x+} \cdot \frac{m_{20}m_{32}-m_{22}m_{30}}{m_{22}m_{33}-m_{23}m_{32}} \\ E_N^{x+} &= E_0^{x+} \cdot \left( m_{00} + \frac{-m_{20}(m_{02}m_{33}-m_{03}m_{32})+m_{30}(m_{02}m_{23}-m_{03}m_{22})}{m_{22}m_{33}-m_{23}m_{32}} \right) \\ E_N^{y+} &= E_0^{x+} \cdot \left( m_{10} + \frac{-m_{20}(m_{12}m_{33}-m_{13}m_{32})+m_{30}(m_{12}m_{23}-m_{13}m_{22})}{m_{22}m_{33}-m_{23}m_{32}} \right) \end{cases} \tag{5.24}$$

This transfer matrix method was used to calculate the transmission through $N$ slides with and without Faraday rotation by my colleague G. J. Aubry. The results will directly be compared to Q1D experimental data in section 5.3. Different realizations of disorder were realized by varying the thicknesses $d_i$ and $e_i$ of both the plates and the spaces between the plates uniformly over $\Delta d$ and $\Delta e \gg \lambda_0$.

## 5.2 Experimental samples and setups

Special requirements regarding the sample and a specialized setup are requested to look for localization of light in a quasi 1D system of $N$ glass plates via magnetic field manipulation.

### 5.2.1 Quasi 1D sample

The setup was designed to turn the linear incoming polarization via Faraday rotation (eq. (4.1): $\theta = VBL$) by $\sim 45°$ for the propagation through one plate under full available magnetic field to randomize the phase of the waves on their way through a stack of glass plates using Faraday rotation. More precisely, round glass plates ($d = 2.5$ cm, $L = 1.5$ mm) of a Schott glass SF57 were used. The Verdet constant was measured to be $V \approx 31.0 \pm 0.1$ rad/T (in good agreement with literature [73]) which corresponds to a rotation angle of $\theta \approx 48°$ for one plate at the used wavelength ($\lambda = 532$ nm) and the available magnetic field ($B = 18$ T). Since it is difficult to find stronger Faraday active transparent materials that are easily available, these plates were chosen even if they needed to be relatively thick, which is a disadvantage compared to Park *et al.* [129] who uses a stack of thin (150 $\mu$m on average) microscope glass plates as their Q1D sample. Thick plates lead to a quicker crossover from 1D to Q1D and thus extend $\ell_{1D\to Q1D}$. On the other hand the high refractive index of SF57 ($n = 1.84$ at $\lambda = 633$ nm [73]) lowers the competing localization length $\xi$ by increasing the scattering/reflection.

Putting the plates randomly on top of each other leads to random spacings between the plates. Since the plates were not specially requested to be optically flat, they have a relatively large surface roughness (larger than the wavelength of the incident light). This leads to varying spacings and thickness at different transverse spacial positions of the stack, such that at different spacial positions in transmission the light wave has encountered different sample configurations. The idea is to send a relatively wide ($\approx 0.5$ cm) parallel coherent light beam through this stack of $N$ (varying from 0-50) glass plates and measure the transmission at different spacial positions (using a CCD camera with 1900x1200 pixel and 12 bit from The Imaging Source, DMK 23UX174). Averaging over the different pixels is then equivalent to a configuration averaging. Note that the surface roughness and small tilts of the plates can lead to a mode mixing and thus to a crossover from 1D to quasi 1D. To minimize this the plates were cleaned before putting them on top of each other such that they were not tilted too much by impurities.

### 5.2.2 Quasi 1D speckles in high magnetic fields

The sample was put in a cylindrical sample holder (see fig. 5.3(b)) that is inside a hollow cylinder which can be turned via a rubber hose by a motor to guarantee for a more complete set of configurations in the averaging. Rotating the sample changes the configurations slightly due to the non-perfect sample

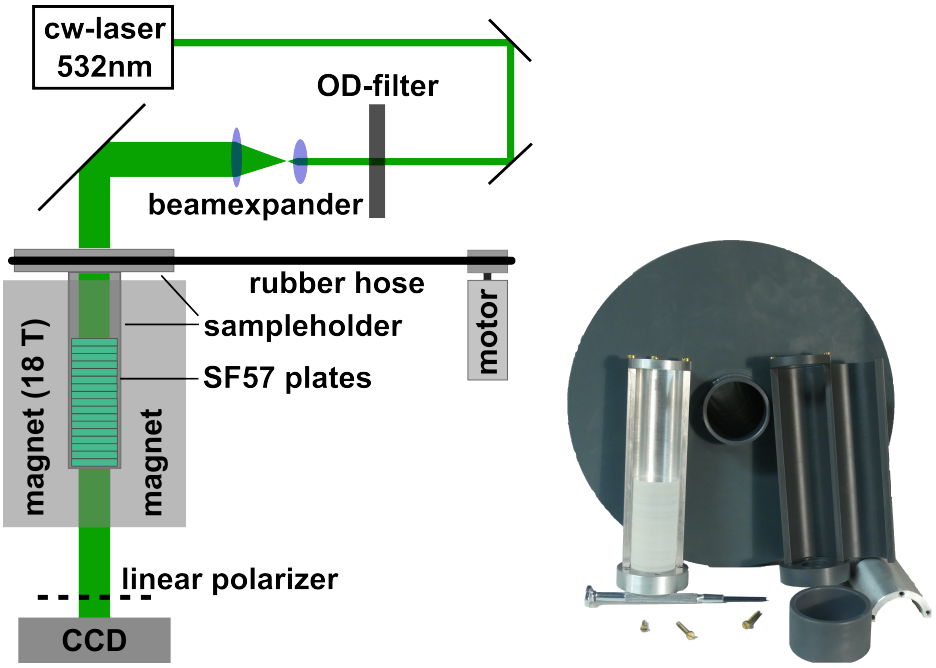


(a) (b)

**Figure 5.3:** (a) Quasi 1D light transport setup: A cw laser beam is sent through an OD filter to control the incident intensity before being expanded to $\approx$ 0.5 cm. This expanded beam illuminates the sample made of SF57 plates (varying from 0 to 50). The transmitted light passes a polarizer to select one plane of polarization before beeing captured by a CCD camera. The sample is placed inside a sampleholder which is rotated constantly via a rubber hose by a motor. The sample inside the holder as shown in (b) is placed in a superconducting magnet bore. Figure taken from [137] and modified.

alignment and the non-centered beam position. The motor turns the sample once per minute which corresponds to the measurement time for each sample. In this time the camera took 300 images (5 per second). The exposure was chosen to be as small as possible ($10^{-4}$ s) to minimize the averaging which occurs by turning the sample. More advanced configuration averaging was tried out by putting two ring piezos between the plates to vary spaces between the plates. Better averaging results were achieved with turning the sample than by the piezos such that the turning setup was used.[2]

The setup is shown schematically in fig. 5.3(a). The linear polarized coherent

[2]More details about the setup and earlier versions can be found in the bachelor thesis of O. Irtenkauf [137].

laser beam ($\lambda = 532$ nm) comes from a cw laser (Torus, Laser Quantum). It can be tuned between $P = 0.5 - 0.75$ W. An OD filter is used to further control the incident intensity such that the camera is not saturated. Afterwards the beam is expanded using two lenses with $f_1 = 200$ mm and $f_2 = 1000$ mm. The beam is then led through the sample that is placed inside the same superconducting magnet (with maximum field $B = 18$ T) as used in sec. 4.5.1. The beam was adjusted by passing parallel through the relatively long (1174 mm) bore and aligning the backreflection of the first plate into the incident beam. A linear polarizer can be put in front of the CCD to capture only the photons with the same polarization as the incident light and thus measure only one independent speckle pattern.

### 5.2.3 Data analysis

The measured speckle images were further processed to obtain the mean transmission $\tau$ (and/or the mean of the logarithm of the transmission $\langle \ln \tau \rangle$) and the variance of the relative transmitted intensity which are defined as follows:

$$\langle x \rangle = \frac{1}{N} \sum_{i=1}^{N} x_i \ , \qquad \mathrm{var}(\frac{x}{\langle x \rangle}) = \frac{\langle x^2 \rangle}{\langle x \rangle^2} - 1 \ . \tag{5.25}$$

Figure 5.4 shows the different steps of the image processing for one measured image of a transmission speckle. The intensity variations caused by the incident Gaussian beam need to be removed to obtain the correct intensity statistics. A 3D plot of an original image is shown in the upper left. A speckle pattern overlaying the Gaussian beam can be observed. The intensity data was fitted by a 2D Gaussian with widths $\sigma_\mathrm{x}$ and $\sigma_\mathrm{y}$ and an offset $b$. The offset is necessary to account for noise and was subtracted from the images (lower left). Moreover, an elliptical region of interest (ROI) was chosen with widths $2\sigma_\mathrm{x}$ and $2\sigma_\mathrm{y}$ respectively (see cutoff in the upper right image). The elliptical form is necessary since for a large number of plates the transmitted beam becomes elliptical due to non-perfect alignment of the sample regarding the beam direction (see lower right (20 plates) in fig. 5.5). This ellipse rotates with the rotating sample such that the ROI was further narrowed by taking into account only the overlap of the ellipses of all 300 images. The ROI was divided by the Gaussian fit to obtain the final images as shown in the lower right in fig. 5.4. The speckle are exponentially distributed with some high peaks as expected for localized modes. For an increasing number of glass slides increasing laser powers were used as the transmission decreases with the number of plates. Therefore, the transmitted images were normalized by the incident laser power. All details

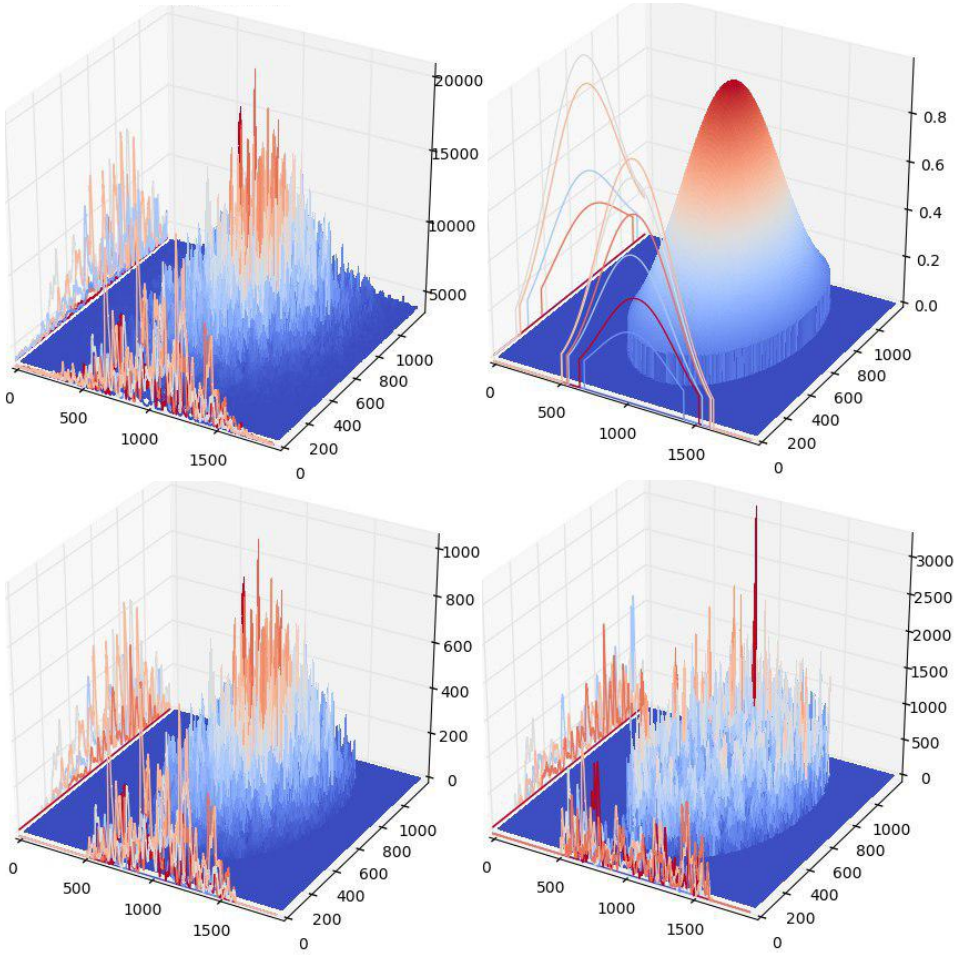


**Figure 5.4:** 3D image of a measured speckle patter before image processing (upper left). The intensity is plotted on the z axis while x and y are the camera pixel values. A Gaussian was fitted with an offset and a region of interest was defined via a radius $r = 2\sigma$ (upper right). Then the offset was subtracted from the image (lower left) and the image was weighted by the Gaussian to remove the intensity differences caused by the incident Gaussian laser beam. Image taken from ref. [137].

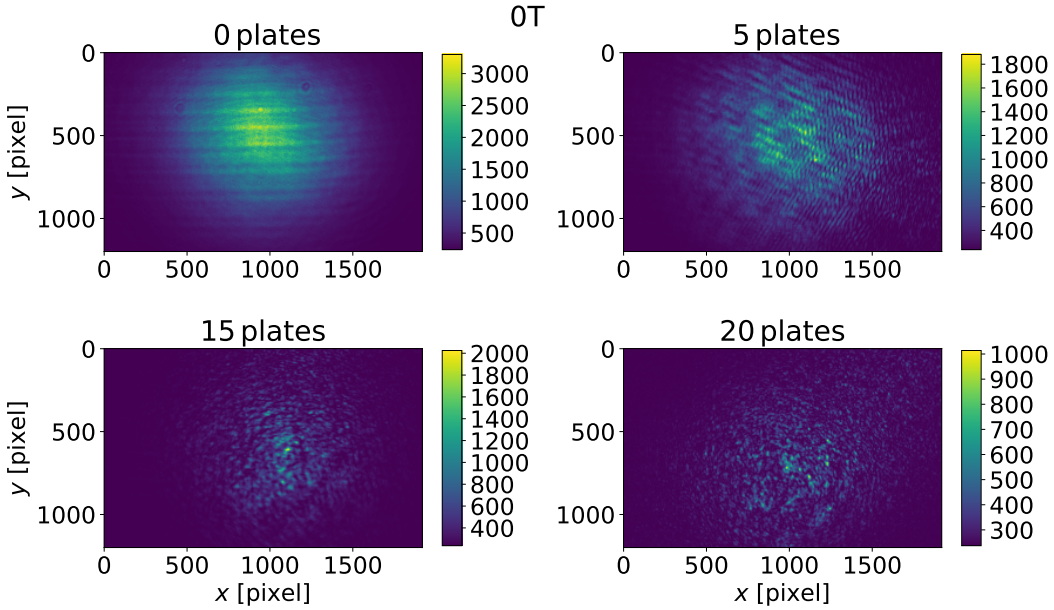


**Figure 5.5:** Four measured images for increasing number of plates (0, 5, 15, 20) are shown. The measurement was performed at B=0 T with polarizer in front of the camera. The colorbar shows the measured intensities.

about the analysis can be found in the bachelor thesis of O. Irtenkauf [137].

Figure 5.5 shows how the observed transmission changes with the number of plates $N$. Images for $N = 0, 5, 15, 20$ plates are shown for $B = 0$ T with a polarizer in front of the CCD. For 0 plates already a fringe pattern is observed arising from the glass plate protecting the camera sensor, but still the Gaussian beam can be observed. For 5 plates some larger but still regular speckles are observed. The image with 15 plates shows random speckles overlapping the Gaussian shaped beam. For 20 plates some high intensity speckle can be seen with larger regions of very low intensity in between, but the beam shows a very elliptical tail arising from scattering out of the incident direction. Here the quasi 1D sample geometry is observed.

The same can be observed when looking at the histogram of intensity of the same measurement. These histograms are shown in fig. 5.6. For 0 plates a Gaussian distribution is observed. This crosses over to an exponential distribution for $\sim$ 20 plates. For 30 plates deviations at high intensity values are observed in form of a tail decaying slower than exponentially as would be expected for localized light [129].

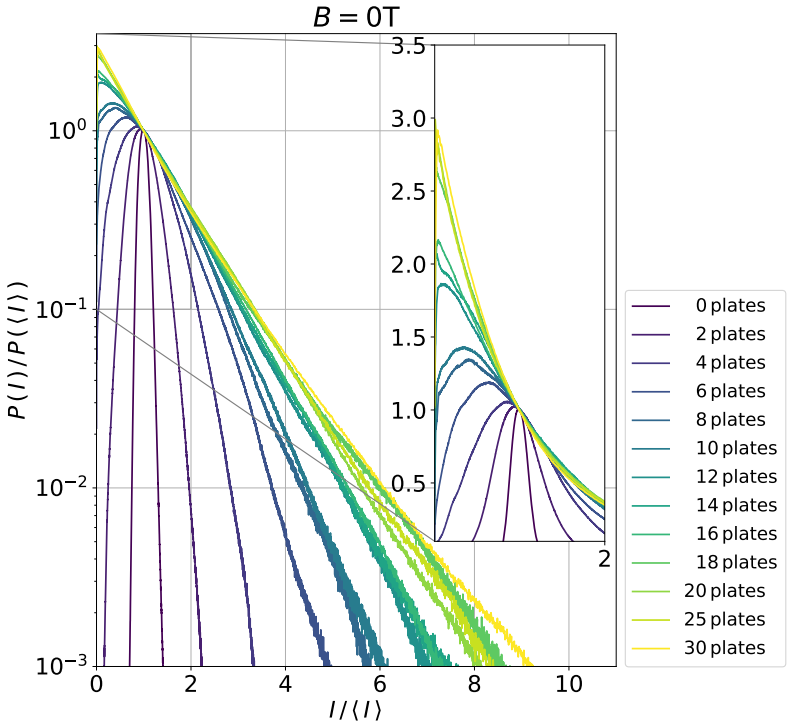


**Figure 5.6:** Histogram of the normalized intensity $I/\langle I\rangle$ for different number of plates $N$ at $B = 0$ T with polarizer in front of the CCD. The inset shows a zoom with linear scale for $0 \leq I/\langle I\rangle \leq 2$.

## 5.3 1D light transport in high magnetic fields

In this section I show transfer matrix simulations[3] (perfect 1D case) of the mean logarithmic relative transmission $\langle \ln \tau \rangle$ over various configurations of disorder and the normalized transmitted intensity $\mathrm{var}\,(I/\langle I \rangle)$ and compare them to experimental data obtained with the setup described in the latter section, to test how the Faraday effect can influence light localization and to study the difference between 1D and Q1D (as present in experiments). The sample is a stack of $N$ Faraday active glass slides with the same Verdet constant and of the same thickness $L$ in the simulations as in the experiments.

### 5.3.1 Static transmission

As was explained in sec. 5.1.1 the static transmission through a stack of glass slides is expected to decay exponentially with number of slides $N$. This is observed in the transfer matrix simulations (blue dots in fig. 5.7(a)) as well as in the experiments (blue dots in fig. 5.7(b)). The result of the simulation equals the theoretical prediction for the perfect 1D case without absorption (see eq. (5.8)). The decay is seen to be slower (and more noisy) for the experimental data which might be caused by the non-perfect alignment of the plates. Such a deviation from the perfect 1D case was also studied by Zhang *et al.* [138]. Moreover, the decay of $\langle \ln \tau \rangle$ is plotted in presence of a magnetic field $B = 18$ T (orange squares). In both, the transfer matrix calculations as well as the experiments, oscillations with increasing number of plates are observed. These oscillations come from the fact that for small number of plates, most photons of the transmitted beam leave the sample without being scattered, such that the mean polarization state is governed by the Faraday rotation of the photons through the plates in one direction. Using an analyzer in front of the camera, as in fig. 5.7, this leads to a suppression of the transmitted beam for 2, 6, ... plates where the polarization is tilted by $\sim 90°$ against the incident polarization. For increasing number of plates more multiple scattered photons govern the mean transmission, such that the polarization gets randomized and the oscillations disappear. In the transfer matrix calculations the slope of the decay with $N$ is smaller for the measurement with magnetic field than without. Thus a crossover around 25 plates is observed. This effect might be caused by an increasing localization length under the influence of the magnetic field. In the experiments no such effect was observed.

The inset of fig. 5.7(a) and (b) shows the mean logarithmic relative trans-

[3]The simulations were performed by G. J. Aubry.

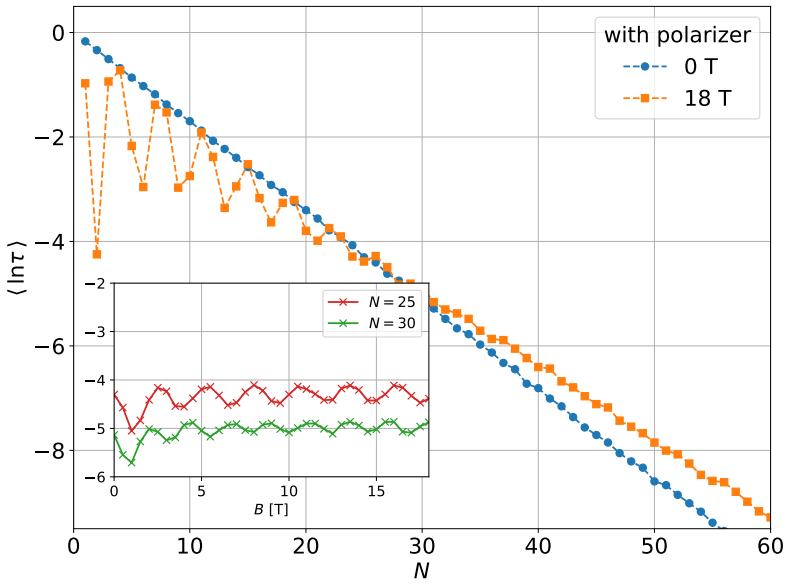


(a) 1D simulation: $L$, $V$ and $\lambda$ same as in experiment.

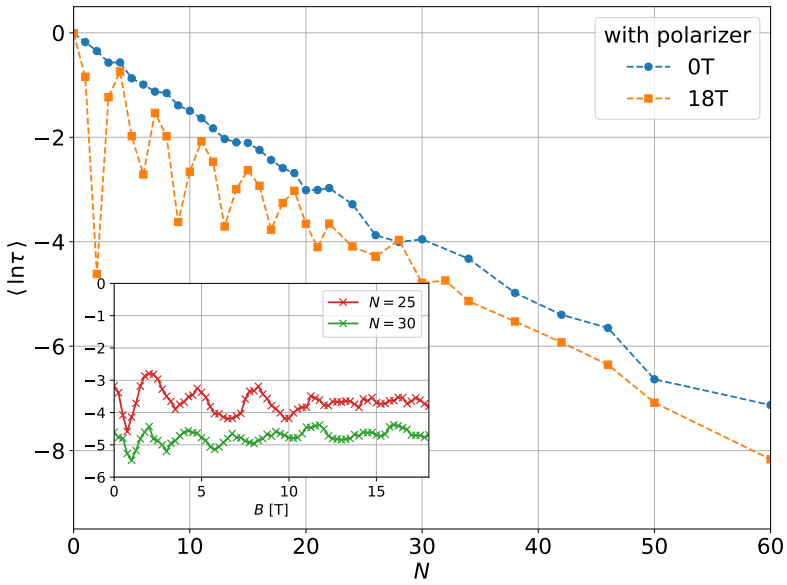


(b) Q1D experiment

**Figure 5.7:** (a) Transfer matrix simulations and (b) experimental data of the mean logarithmic relative transmission $\langle \ln \tau \rangle$ over various configurations of disorder trough a stack of $N$ Faraday active glass slides with (orange squares) and without (blue dots) magnetic field up to $B = 18$ T. The inset shows the same quantity with varying field for $N = 25$ (red) and $N = 30$ (green) plates. A polarizer was put in front of the CCD camera.

mission $\langle \ln \tau \rangle$ plotted for different field values $B$ for $N = 25$ (red) and $N = 30$ (green) plates. Again oscillations are observed, explained by the Faraday rotation (FR) of the plates and the used analyzer. For large fields the oscillations smear out, especially in the experiment. As expected the period of the oscillations becomes smaller for a larger number of plates as there is more FR. In both plots the mean value stays roughly constant as with $N = 25$ and $N = 30$ we are in the crossover region from the $B = 0$ T and the $B = 18$ T measurement.

In the above described experiments, only one plane of polarization was studied using a polarizer in front of the CCD. To measure all transmitted photons and get rid of the mentioned oscillations in the mean transmission this polarizer was removed and the same experiments were performed (see fig. 5.8). For the transfer matrix simulations as shown in fig. 5.8(a) again the same exponential decay without field is observed. This time no oscillations occur with magnetic field, but again a slower decay can be seen with $B = 18$ T starting from $N = 0$. As we see in the inset the increase of the mean logarithmic transmission with increasing field saturates for small fields $B < 5$ T. The increase of $\langle \ln \tau \rangle$ might be interpreted as a destruction of localization using FR, but the saturation (and the existence of an exponential decay) shows that the magnetic field only disturbs some localized modes, which could be connected to an increasing localization length $\xi$.

Similar observations are made for the experimental data as shown in fig. 5.8(b). Again with (blue circles) and without (orange squares) magnetic field an exponential decay is observed. In run 1 (open symbols) a deviation from the exponential is observed with magnetic field for $N \approx 15$. To exclude experimental problems[4] and to obtain more reliable data another run was performed. This time no such deviation was observed, but in both runs the measurement with field lies slightly above the measurement without field, but much less than in the transfer matrix calculations. In the inset two field runs for $N = 30$ (green) and one for $N = 0$ plates are shown. The $N = 0$ run is very stable and used as reference. The measurements with $N = 30$ are more noisy. No clear increase of the transmission is observed for small fields, consistent with the measurement in the main plot.

While both transfer matrix simulations with and without polarizer show clear magnetic field effects, no such conclusion can be done for the experimental data. The variance of the normalized transmitted intensity $\mathrm{var}\,(I/\langle I \rangle)$ is analyzed in the following section to check whether such effects might be

[4]The plates were put in manually such that the holder has to be removed from the setup for each plate and the relatively low temperature inside the magnet bore led to fogged windows when the experiments were performed too slowly.

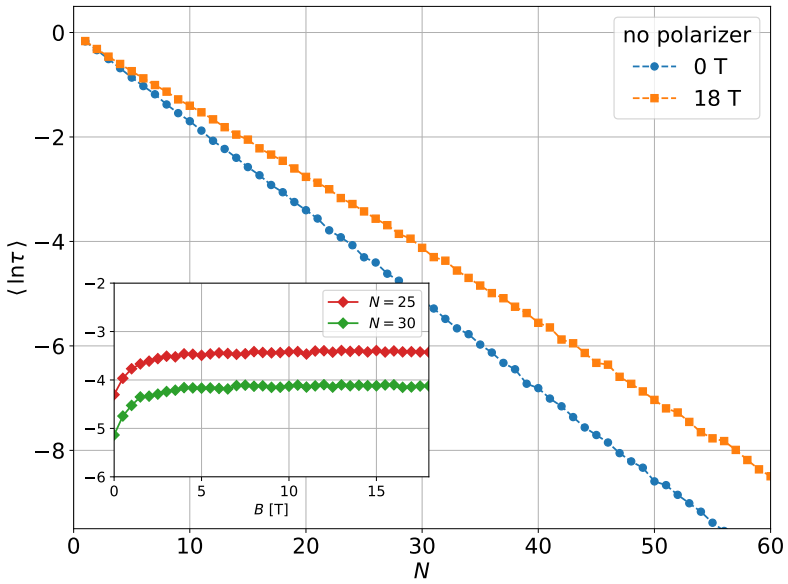


(a) 1D simulation: $L$, $V$ and $\lambda$ same as in experiment.

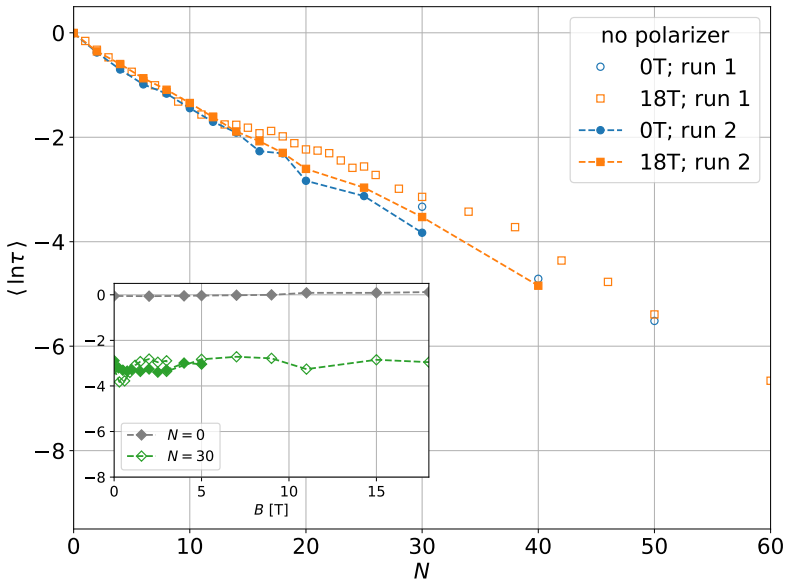


(b) Q1D experiment

**Figure 5.8:** (a) Transfer matrix simulations and (b) experimental data of the mean logarithmic relative transmission $\langle \ln \tau \rangle$ over various configurations of disorder trough a stack of $N$ Faraday active glass slides with (orange squares) and without (blue dots) magnetic field. In the experiments two runs were performed to obtain more reliable data. The inset shows the same quantity with varying field for $N = 25$ (red) and $N = 30$ (green) plates for the simulations and $N = 0$ (grey) and $N = 30$ (green, two runs) for the experiments. No polarizer was put in front of the CCD camera.

suppressed by absorption or the quasi 1D geometry.

### 5.3.2 Transmission fluctuations

For the perfect 1D case as in the transfer matrix simulations the variance of the normalized transmitted intensity $\mathrm{var}\,(I/\langle I\rangle)$ is expected to increase exponentially with number of plates $N$ indicating a strong increase of the fluctuations in transmission in the localized regime. Figure 5.9(a) shows $\mathrm{var}\,(I/\langle I\rangle)$ measured for one polarization state (with polarizer) at the output. The localization threshold $\mathrm{var}\,(I/\langle I\rangle) = 7/3$ (eq. (5.12)) is reached around $N = 20$ for the simulation without field (blue dots). For the simulation with magnetic field ($B = 18$ T) still an exponential increase is observed, but the threshold is at a larger number of plates $N \approx 25$ which is connected to an increase of the localization length. Note further that for small number of plates again oscillations are observed in the magnetic field measurement. The inset shows $\mathrm{var}\,(I/\langle I\rangle)$ for $N = 25$ and $N = 30$ for increasing field. Consistent with earlier observations a decrease for fields $B < 5$ T is observed as well as oscillations for small fields.

Figure 5.9(b) shows the experimental data for $\mathrm{var}\,(I/\langle I\rangle)$ versus $N$ without (blue dots) and with (orange squares) magnetic field. For a small number of plates $N < 20$ a similar exponential increase as in the simulations can be observed but with a smaller exponent. Also the oscillations with magnetic field are recovered, but at $N > 20$ plates a saturation occurs. The occurrence of such a plateau in the variance of the transmitted intensity was interpreted by Park *et al.* [129] as a crossover from 1D to Q1D and can be connected to the crossover length $\ell_{1D\to Q1D}$. High intensity fluctuations are suppressed by mode coupling. Unfortunately in our case, this length is in the same regime as the localization length $\xi$, such that no difference in the plateau value is observed without and with magnetic field $B$. Note further that the value of the localization threshold could not be reached in the experiments.

Figure 5.10 shows the same simulations and experiments without a selection of polarization at the output. Again in the simulation an exponential increase with increasing sample size is observed. Moreover, the simulation with magnetic field shows a smaller exponent. In the experiments one can see such an increase for small number of plates and again for all measurements with and without magnetic field a plateau occurs. This time the plateau value with magnetic field ($B = 18$ T) is lowered. The same decrease with field can be observed in the inset for the measurement of $\mathrm{var}\,(I/\langle I\rangle)$ versus $B$ for $N = 30$. As in this measurement no polarizer was in front of the CCD the measured image with $B = 18$ T is the average over two vertical to each other polarized speckle

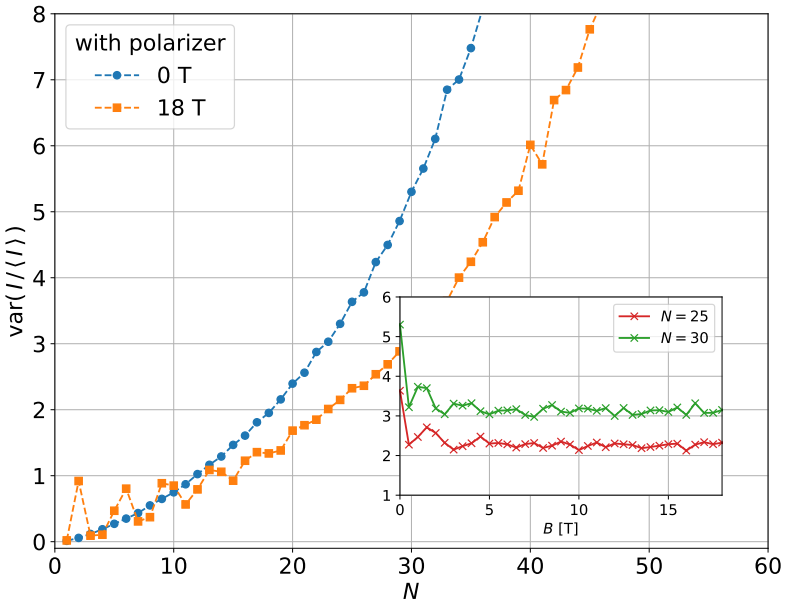


(a) 1D simulation: $L$, $V$ and $\lambda$ same as in experiment.

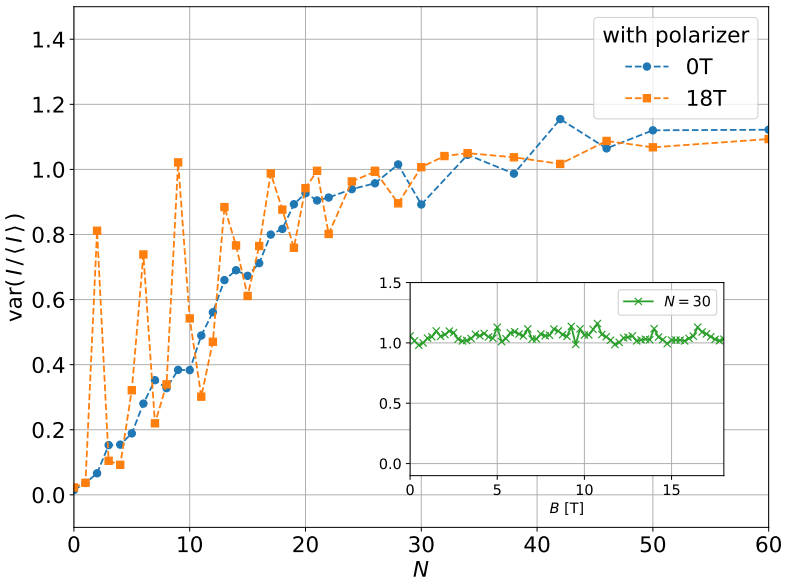


(b) Q1D experiment

**Figure 5.9:** (a) Transfer matrix simulations and (b) experimental data of the variance of the normalized transmitted intensity var $(I/\langle I\rangle)$ trough a stack of $N$ Faraday active glass slides with (orange squares) and without (blue dots) magnetic field. The inset shows the same quantity with varying field for $N = 25$ (red, in (a) only) and $N = 30$ (green) plates. A polarizer was put in front of the CCD camera.

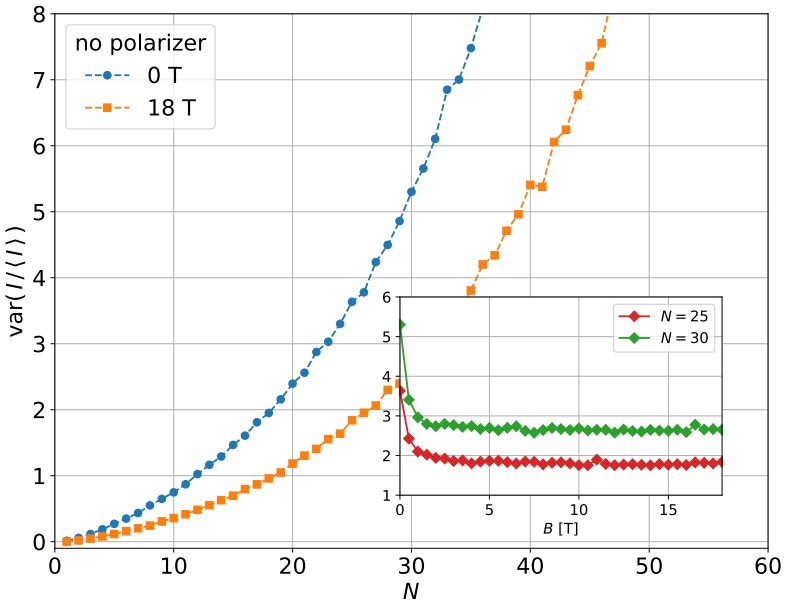


(a) 1D simulation: $L$, $V$ and $\lambda$ same as in experiment.

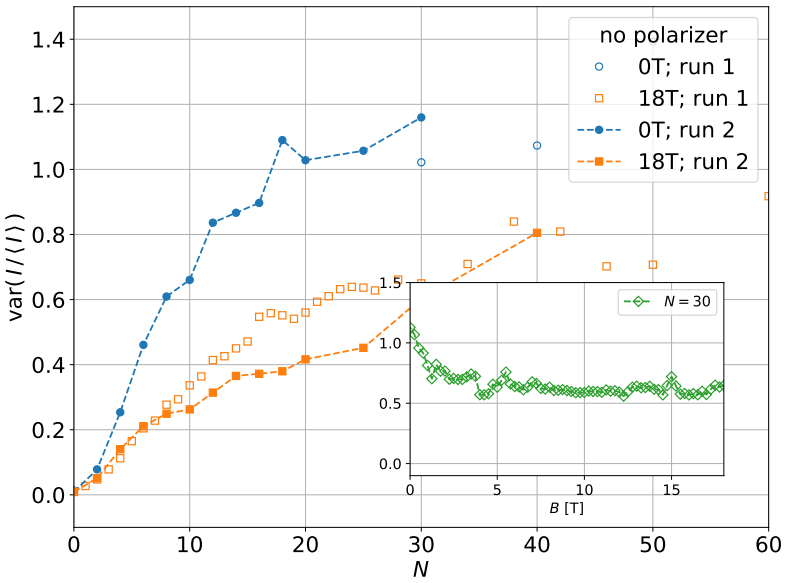


(b) Q1D experiment

**Figure 5.10:** (a) Transfer matrix simulations and (b) experimental data of the variance of the normalized transmitted intensity var $(I/\langle I\rangle)$ trough a stack of $N$ Faraday active glass slides with (orange squares) and without (blue dots) magnetic field up to $B = 18$ T. In the experiments two runs were performed to obtain more reliable data. The inset shows the same quantity with varying field for $N = 25$ (red, in (a) only) and $N = 30$ (green) plates. No polarizer was put in front of the CCD camera.

patterns as the field randomized the polarization. This leads to a lowering of the fluctuations in the image and arbitrarily lowers var $(I/\langle I\rangle)$ and respectively the plateau value. Thus, no clear signs of magnetic field effects on localization are observed here.

To be able to observe localization in 1D experiments and study the influence of FR on localization experimentally the crossover length $\ell_{1D\to Q1D}$ would need to be increased such that the localization threshold $\ell_{1D\to Q1D} > \xi$ is reached. This might be achieved by a better sample alignment e.g. with piezo elements between each plate to align each plate in a controlled manner and separately or by thinner glass plates keeping the FR high enough to randomize the polarization state. The first solution leads to a very sophisticated experimental sample, which might be hard to realize. The second solution might be easier to realize as the simulations versus the magnetic field (inset) showed a saturation of the magnetic field effect for small field values, such that thinner plates could still have a strong enough FR.

# Chapter 6

# Conclusion

Wave transport can become very complex in disordered photonic media. Especially transport properties in densely packed, highly scattering media are difficult to predict and very careful interpretation of data is required. In this thesis experiments on light transport in commercial "white paint" materials were performed first. They questioned earlier claims of Anderson localization of light in 3D in the same samples. Earlier observed deviations from diffusion were explained by weak fluorescent signals, consistent with an adapted diffusion model. A transport model was developed using the ECPA effective refractive index approach to optimize the scattering strength in "white paint" materials and study resonant light transport in densely packed, random assembled, highly multiple scattering media. This model was tested on low (polysterene) and high index (titanium dioxide) photonic glasses via spectral measurements of the scattering strength $\lambda/\ell^\star$. The model predicts very well resonant transport behavior in high and low index (monodisperse) photonic glasses. Moreover, the general scattering behavior even of the commercial "white paints" as well as of polydisperse photonic glasses is explained reasonably well by the presented model. No signs of localization are observed in the fabricated materials consistent with the model predictions. A proof of principle experiment, in which the magneto-optical Faraday effect is used to manipulate reciprocity in highly scattering samples, is performed to learn about the origin of light localization. Transmission speckle correlations and coherent backscattering experiments in high magnetic fields and at low temperatures show that this method can be used to look for light localization in powder mixtures of highly scattering and highly Faraday active materials. A common way to study light localization is to go to lower dimensional systems (1D or 2D) where scaling theory predicts the existence of localization for large enough system size. Therefore, a quasi 1D sample made of Faraday active glass slides was studied to test the aforementioned magnetic field effect on light transport. No clear influence of the magnetic field on localization is observed in the experiments in contrast to

the results of the transfer matrix simulations. This might be explained by the relatively small crossover length from 1D to quasi 1D geometry in the studied sample.

All performed experiments show that the observation of Anderson localization of light, for 3D and even lower dimensions, is experimentally very challenging. In this thesis the details of the experimental observation methods (e.g. ToF, TP, magnetic field manipulation) and their data interpretation were further developed and a deeper understanding of wave transport in densely packed, random assembled media is gained. The shown ECPA scattering model combined with the performed experiments allow us to understand very well the light transport in photonic glasses and commercial "white paints".

## 6.1 Perspective

Coherent light transport in highly multiple scattering media has been studied for years [11], but optical experiments still bear to show signs of Anderson localization of light in 3D as explained in this thesis. Although light localization could not be reached in the here performed experiments, they led to a better quantitative understanding of transport in "white paint" materials. This let us predict that further tuning in the sample preparation and/or structure is needed to observe Anderson localization of light in 3D. Higher index photonic glasses are expected by the ECPA scattering model to reach the localization threshold $k\ell^\star < 1$ for certain size ratios, but are a challenge for material scientists to synthesize. In lower dimensional systems localization can be studied experimentally if a crossover to quasi 1D geometry can be avoided. This could be achieved using thinner glass plates while keeping the Faraday rotation large enough or by a more controlled sample alignment e.g. with piezo elements between each glass plate.

The experiments and simulations performed in this thesis explain why scientists have failed to observe 3D localization for years. The developed methods and the gained understanding of coherent light transport in randomly assembled highly multiple scattering media bring us closer to a possible observation of this supposedly universal phenomenon, but also show the long way to go and how careful experimental data needs to be treated in the search for signs of localization.

# Bibliography


[1] E. Akkermans and G. Montambaux. *Mesoscopic Physics of Electrons and Photons*. Cambridge University Press, (2007).

[2] A. Lagendijk, B. v. Tiggelen, and D. S. Wiersma. "Fifty years of Anderson localization". *Physics Today* **62**, 24 (2009). DOI: 10.1063/1.3206091.

[3] E. Abrahams, P. W. Anderson, D. C. Licciardello, and T. V. Ramakrishnan. "Scaling Theory of Localization: Absence of Quantum Diffusion in Two Dimensions". *Phys. Rev. Lett.* **42**, 673 (1979). DOI: 10.1103/PhysRevLett.42.673.

[4] G. Bayer and T. Niederdränk. "Weak localization of acoustic waves in strongly scattering media". *Phys. Rev. Lett.* **70**, 3884 (1993). DOI: 10.1103/PhysRevLett.70.3884.

[5] B. Tallon, T. Brunet, and J. H. Page. "Impact of Strong Scattering Resonances on Ballistic and Diffusive Wave Transport". *Phys. Rev. Lett.* **119**, 164301 (2017). DOI: 10.1103/PhysRevLett.119.164301.

[6] E. Larose, L. Margerin, B. A. van Tiggelen, and M. Campillo. "Weak Localization of Seismic Waves". *Phys. Rev. Lett.* **93**, 048501 (2004). DOI: 10.1103/PhysRevLett.93.048501.

[7] F. Jendrzejewski, K. Müller, J. Richard, A. Date, T. Plisson, P. Bouyer, A. Aspect, and V. Josse. "Coherent Backscattering of Ultracold Atoms". *Phys. Rev. Lett.* **109**, 195302 (2012). DOI: 10.1103/PhysRevLett.109.195302.

[8] P. E. Wolf and G. Maret. "Weak Localization and Coherent Backscattering of Photons in Disordered Media". *Phys. Rev. Lett.* **55**, 2696 (1985). DOI: 10.1103/PhysRevLett.55.2696.

[9] M. P. V. Albada and A. Lagendijk. "Observation of Weak Localization of Light in a Random Medium". *Phys. Rev. Lett.* **55**, 2692 (1985). DOI: 10.1103/PhysRevLett.55.2692.

[10] R. Sapienza, P. D. García, J. Bertolotti, M. D. Martín, Á. Blanco, L. Viña, C. López, and D. S. Wiersma. "Observation of Resonant Behavior in the Energy Velocity of Diffused Light". *Phys. Rev. Lett.* **99**, 233902 (2007). DOI: 10.1103/PhysRevLett.99.233902.

[11] D. S. Wiersma. "Disordered photonics". *Nat. Photon.* **7**, 188 (2013). DOI: 10.1038/nphoton.2013.29.

[12] F. Scheffold. "Speckle-Korrelationen und universelle Leitwertfluktuationen von Licht". PhD thesis. Konstanz: Universität Konstanz (1998).

[13] P. W. Anderson. "The question of classical localization: a theory of white paint?" *Philos. Mag. B* **52**, 505 (1985). DOI: 10.1080/13642818508240619.

[14] P. W. Anderson. "Absence of Diffusion in Certain Random Lattices". *Phys. Rev.* **109**, 1492 (1958). DOI: 10.1103/PhysRev.109.1492.

[15] H. Hu, A. Strybulevych, J. H. Page, S. Skipetrov, and B. van Tiggelen. "Localization of Ultrasound in a Three-Dimensional Elastic Network". *Nat. Phys.* **4**, 945 (2008). DOI: 10.1038/nphys1101.

[16] S. S. Kondov, W. R. McGehee, J. J. Zirbel, and D. B. "Three-Dimensional Anderson Localization of Ultracold Matter". *Science* **334**, 66 (2011). DOI: 10.1126/science.1209019.

[17] F. Jendrzejewski, A. Bernard, K. Müller, P. Cheinet, V. Josse, M. Piraud, L. Pezzé, L. Sanchez-Palencia, A. Aspect, and P. Bouyer. "Three-dimensional localization of ultracold atoms in an optical disordered potential". *Nat. Phys.* **8**, 398 (2012). DOI: 10.1038/nphys2256.

[18] M. Störzer, P. Gross, C. M. Aegerter, and G. Maret. "Observation of the Critical Regime Near Anderson Localization of Light". *Phys. Rev. Lett.* **96**, 063904 (2006). DOI: 10.1103/PhysRevLett.96.063904.

[19] T. Sperling, W. Bührer, C. M. Aegerter, and G. Maret. "Direct determination of the transition to localization of light in three dimensions". *Nat. Photon.* **7**, 48 (2013). DOI: 10.1038/nphoton.2012.313.

[20] S. Fraden and G. Maret. "Multiple light scattering from concentrated, interacting suspensions". *Phys. Rev. Lett.* **65**, 512 (1990). DOI: 10.1103/PhysRevLett.65.512.

[21] H. van de Hulst. *Light Scattering by Small Particles*. Vol. 10. Dover Books on Physics Series 12. New York: Dover Publications, (1957), 28. DOI: 10.1063/1.3060205.

[22] K. Busch and C. M. Soukoulis. "Transport properties of random media: An energy-density CPA approach". *Phys. Rev. B* **54**, 893 (1996). DOI: 10.1103/PhysRevB.54.893.

[23] P. D. García, R. Sapienza, J. Bertolotti, M. D. Martín, Á. Blanco, A. Altube, L. Viña, D. S. Wiersma, and C. López. "Resonant light transport through Mie modes in photonic glasses". *Phys. Rev. A* **78**, 023823 (2008). DOI: 10.1103/PhysRevA.78.023823.

[24] R. Rezvani Naraghi, S. Sukhov, J. J. Sáenz, and A. Dogariu. "Near-Field Effects in Mesoscopic Light Transport". *Phys. Rev. Lett.* **115**, 203903 (2015). DOI: 10.1103/PhysRevLett.115.203903.

[25] R. Lenke and G. Maret. "Affecting weak light localization by strong magnetic fields". *Physica Scripta* **1993**, 605 (1993). DOI: 10.1088/0031-8949/1993/T49B/039.

[26] R. Lenke and G. Maret. "Multiple Scattering of Light : Coherent Backscattering and Transmission". In: *Scattering in polymeric and colloidal systems*. Ed. by W. Brown, 1. Amsterdam: Gordon & Breach, (2000).

[27] M. Störzer. "Anderson Localization of Light". PhD thesis. Konstanz: Universität Konstanz (2006). URL: http://nbn-resolving.de/urn:nbn:de:bsz:352-opus-22027.

[28] W. Bührer. "Anderson Localization of Light in the Presence of Nonlinear Effects". PhD thesis. Konstanz: Universität Konstanz (2012). URL: http://nbn-resolving.de/urn:nbn:de:bsz:352-207872.

[29] L. Schertel. "Magneto-optical Faraday effect in multiple-scattering media". MA thesis. Universität Konstanz (2014). URL: http://nbn-resolving.de/urn:nbn:de:bsz:352-2--594xcs5wq80q3.

[30] F. A. Erbacher. "Licht-Vielfachstreuung in magneto-optisch aktiven Medien". PhD thesis. Konstanz: Universität Konstanz (1992).

[31] M. Fink. "Time reversal in acoustics". *Contemporary Physics* **37**, 95 (1996). DOI: 10.1080/00107519608230338.

[32] G. Modugno. "Anderson localization in Bose–Einstein condensates". *Reports on Progress in Physics* **73**, 102401 (2010). DOI: 10.1088/0034-4885/73/10/102401.

[33] E. Akkermans, P. E. Wolf, and R. Maynard. "Coherent Backscattering of Light by Disordered Media: Analysis of the Peak Line Shape". *Phys. Rev. Lett.* **56**, 1471 (1986). DOI: 10.1103/PhysRevLett.56.1471.

[34] C. M. Aegerter and G. Maret. "Coherent Backscattering and Anderson Localization of Light". In: *Progress in Optics*. Ed. by E. Wolf. Vol. 52, 1. Progress in Optics. Elsevier, (2009). DOI: 10.1016/S0079-6638(08)00003-6.

[35] S. Fiebig. "Coherent Backscattering from Multiple Scattering Systems". PhD thesis. Konstanz: Universität Konstanz (2010). URL: http://nbn-resolving.de/urn:nbn:de:bsz:352-opus-123390.

[36] T. Sperling. "The Experimental Search for Anderson Localisation of Light in Three Dimensions". PhD thesis. Universität Konstanz (2015). URL: http://nbn-resolving.de/urn:nbn:de:bsz:352-0-300030.

[37] J. X. Zhu, D. J. Pine, and D. A. Weitz. "Internal reflection of diffusive light in random media". *Phys. Rev. A* **44**, 3948 (1991). DOI: 10.1103/PhysRevA.44.3948.

[38] S. Fiebig, C. M. Aegerter, W. Bührer, M. Störzer, E. Akkermans, G. Montambaux, and G. Maret. "Conservation of energy in coherent backscattering of light". **81**, 64004 (2008). DOI: 10.1209/0295-5075/81/64004.

[39] S. N. Mott. "Metal-insulator transitions." *Physics Today* **31**, 42 (1978). DOI: 10.1063/1.2994815.

[40] P. W. Anderson. "More Is Different". *Science* **177**, 393 (1972). DOI: 10.1126/science.177.4047.393.

[41] W. R. McGehee, S. S. Kondov, W. Xu, J. J. Zirbel, and B. DeMarco. "Three-Dimensional Anderson Localization in Variable Scale Disorder". *Phys. Rev. Lett.* **111**, 145303 (2013). DOI: 10.1103/PhysRevLett.111.145303.

[42] G. Semeghini, M. Landini, P. Castilho, S. Roy, G. Spagnolli, A. Trenkwalder, M. Fattori, M. Inguscio, and G. Modugno. "Measurement of the mobility edge for 3D Anderson localization". *Nat. Phys.* **11**, 554 (2015). DOI: 10.1038/nphys3339.

[43] A. F. Ioffe and A. R. Regel. "Non-crystalline, amorphous, and liquid electronic semiconductors". In: *Progress in Semiconductors*. Ed. by A. F. Gibson, F. A. Kroger, and R. E. Burgess. Vol. 4, 237. London: Heywood, (1960).

[44] G. Pólya. "Über eine Aufgabe der Wahrscheinlichkeitsrechnung betreffend die Irrfahrt im Strassennetz". *Mathematische Annalen* **84**, 149 (1921). DOI: 10.1007/BF01458701.

[45] C. Domb. "On multiple returns in the random-walk problem". *Mathematical Proceedings of the Cambridge Philosophical Society* **50**, 586 (1954). DOI: 10.1017/S0305004100029716.

[46] D. J. Thouless. "Electrons in disordered systems and the theory of localization". *Phys. Rep.* **13**, 93 (1974). DOI: 10.1016/0370-1573(74)90029-5.

[47] D. Vollhardt and P. Wölfle. "Diagrammatic, self-consistent treatment of the Anderson localization problem in $d \leq 2$ dimensions". *Phys. Rev. B* **22**, 4666 (1980). DOI: 10.1103/PhysRevB.22.4666.

[48] D. Vollhardt and P. Wölfle. "Self-Consistent Theory of Anderson Localization". In: *Electronic Phase Transitions*. Ed. by W. Hanke and Y. Kopaev. Vol. 32. Chap. 1, 1. Modern Problems in Condensed Matter Sciences. Amsterdam: Elsevier, (1992). DOI: 10.1016/B978-0-444-88885-3.50006-8.

[49] B. A. van Tiggelen, A. Lagendijk, and D. S. Wiersma. "Reflection and Transmission of Waves near the Localization Threshold". *Phys. Rev. Lett.* **84**, 4333 (2000). DOI: 10.1103/PhysRevLett.84.4333.

[50] S. E. Skipetrov and B. A. van Tiggelen. "Dynamics of Anderson Localization in Open 3D Media". *Phys. Rev. Lett.* **96**, 043902 (2006). DOI: 10.1103/PhysRevLett.96.043902.

[51] R. Berkovits and M. Kaveh. "Propagation of waves through a slab near the Anderson transition: a local scaling approach". *Journal of Physics: Condensed Matter* **2**, 307 (1990). DOI: 10.1088/0953-8984/2/2/007.

[52] N. Cherroret, S. E. Skipetrov, and B. A. van Tiggelen. "Transverse confinement of waves in three-dimensional random media". *Phys. Rev. E* **82**, 056603 (2010). DOI: 10.1103/PhysRevE.82.056603.

[53] N. Cherroret. "Coherent transport in random media: from mesoscopic correlations to Anderson localization". PhD thesis. Grenoble: Université Joseph Fourier (2009). URL: https://tel.archives-ouvertes.fr/tel-00424792.

[54] T. Sperling, L. Schertel, M. Ackermann, G. J. Aubry, C. M. Aegerter, and G. Maret. "Can 3D light localization be reached in 'white paint'?" *New Journal of Physics* **18**, 013039 (2016). DOI: 10.1088/1367-2630/18/1/013039.

[55] P. Gross, M. Störzer, S. Fiebig, M. Clausen, G. Maret, and C. M. Aegerter. "A precise method to determine the angular distribution of backscattered light to high angles". *Review of Scientific Instruments* **78**, 033105 (2007). DOI: 10.1063/1.2712943.

[56] J. Pascual, J. Camassel, and H. Mathieu. "Resolved Quadrupolar Transition in $TiO_2$". *Phys. Rev. Lett.* **39**, 1490 (1977). DOI: 10.1103/PhysRevLett.39.1490.

[57] R. D. Shannon, R. C. Shannon, O. Medenbach, and R. X. Fischer. "Refractive Index and Dispersion of Fluorides and Oxides". *Journal of Physical and Chemical Reference Data* **31**, 931 (2002). DOI: 10.1063/1.1497384.

[58] P. Löbl, M. Huppertz, and D. Mergel. "Nucleation and growth in TiO2 films prepared by sputtering and evaporation". *Thin Solid Films* **251**, 72 (1994). DOI: 10.1016/0040-6090(94)90843-5.

[59] C. M. Aegerter, M. Störzer, and G. Maret. "Experimental determination of critical exponents in Anderson localisation of light". *EPL (Europhysics Letters)* **75**, 562 (2006). DOI: 10.1209/epl/i2006-10144-3.

[60] D. S. Wiersma, P. Bartolini, A. Lagendijk, and R. Righini. "Localization of light in a disordered medium". *Nature* **390**, 671 (1997). DOI: 10.1038/37757.

[61] F. J. P. Schuurmans, M. Megens, D. Vanmaekelbergh, and A. Lagendijk. "Light Scattering near the Localization Transition in Macroporous GaP Networks". *Phys. Rev. Lett.* **83**, 2183 (1999). DOI: 10.1103/PhysRevLett.83.2183.

[62] F. Scheffold, R. Lenke, R. Tweer, and G. Maret. "Localization or classical diffusion of light?" *Nature* **398**, 206 (1999). DOI: 10.1038/18347.

[63] D. Wiersma, J. G. Rivas, P. Bartolini, A. Lagendijk, and R. Righini. "Localization or classical diffusion of light? (Reply to comment)". *Nature* **398**, 207 (1999). DOI: 10.1038/18350.

[64] T. van der Beek, P. Barthelemy, P. M. Johnson, D. S. Wiersma, and A. Lagendijk. "Light transport through disordered layers of dense gallium arsenide submicron particles". *Phys. Rev. B* **85**, 115401 (2012). DOI: 10.1103/PhysRevB.85.115401.

[65] F. Scheffold and D. Wiersma. "Inelastic scattering puts in question recent claims of Anderson localization of light". *Nat. Photon.* **7**, 934 (2013). DOI: 10.1038/nphoton.2013.210.

[66] G. Maret, T. Sperling, W. Bührer, A. Lubatsch, R. Frank, and C. Aegerter. "Inelastic scattering puts in question recent claims of Anderson localization of light". *Nat. Photon.* **7**, 934 (2013). DOI: 10.1038/nphoton.2013.281.

[67] C. A. Müller and B. Shapiro. "Comment on "Three-Dimensional Anderson Localization in Variable Scale Disorder"". *Phys. Rev. Lett.* **113**, 099601 (2014). DOI: 10.1103/PhysRevLett.113.099601.

[68] W. R. McGehee, S. S. Kondov, W. Xu, J. J. Zirbel, and B. DeMarco. "McGehee *et al.* Reply". *Phys. Rev. Lett.* **113**, 099602 (2014). DOI: 10.1103/PhysRevLett.113.099602.

[69] C. M. Aegerter, M. Störzer, S. Fiebig, W. Bührer, and G. Maret. "Observation of Anderson localization of light in three dimensions". *J. Opt. Soc. Am. A* **24**, A23 (2007). DOI: 10.1364/JOSAA.24.000A23.

[70] C. M. Aegerter, M. Störzer, W. Bührer, S. Fiebig, and G. Maret. "Experimental signatures of Anderson localization of light in three dimensions". *Journal of Modern Optics* **54**, 2667 (2007). DOI: 10.1080/09500340701627206.

[71] S. E. Skipetrov and J. H. Page. "Red light for Anderson localization". *New Journal of Physics* **18**, 021001 (2016). DOI: 10.1088/1367-2630/18/2/021001.

[72] T. Sperling, W. Bührer, M. Ackermann, C. M. Aegerter, and G. Maret. "Probing Anderson localization of light by weak non-linear effects". *New Journal of Physics* **16**, 112001 (2014). DOI: 10.1088/1367-2630/16/11/112001.

[73] M. J. Weber. *Handbook of Optical Materials*. Laser & Optical Science & Technology. Boca Raton: CRC Press, (2003).

[74] K. Beha, A. Batalov, N. B. Manson, R. Bratschitsch, and A. Leitenstorfer. "Optimum Photoluminescence Excitation and Recharging Cycle of Single Nitrogen-Vacancy Centers in Ultrapure Diamond". *Phys. Rev. Lett.* **109**, 097404 (2012). DOI: 10.1103/PhysRevLett.109.097404.

[75] J. Gómez Rivas, R. Sprik, A. Lagendijk, L. D. Noordam, and C. W. Rella. "Static and dynamic transport of light close to the Anderson localization transition". *Phys. Rev. E* **63**, 046613 (2001). DOI: 10.1103/PhysRevE.63.046613.

[76] S. E. Skipetrov. "Optical devices: Localizing light with electrons". *Nat. Nano.* **9**, 335 (2014). DOI: 10.1038/nnano.2014.86.

[77] R. Rezvani Naraghi and A. Dogariu. "Phase Transitions in Diffusion of Light". *Phys. Rev. Lett.* **117**, 263901 (2016). DOI: 10.1103/PhysRevLett.117.263901.

[78] J. M. Escalante and S. E. Skipetrov. "Longitudinal Optical Fields in Light Scattering from Dielectric Spheres and Anderson Localization of Light". *Annalen der Physik* **529**, 1700039 (2017). DOI: 10.1002/andp.201700039. 1700039.

[79] E. Jimenez-Villar, I. F. da Silva, V. Mestre, P. C. de Oliveira, W. M. Faustino, and G. F. de Sa. "Anderson localization of light in a colloidal suspension (TiO2@silica)". *Nanoscale* **8**, 10938 (2016). DOI: 10.1039/C5NR07540H.

[80] L. S. Froufe-Pérez, M. Engel, J. J. Sáenz, and F. Scheffold. "Band gap formation and Anderson localization in disordered photonic materials with structural correlations". *Proceedings of the National Academy of Sciences* **114**, 9570 (2017). DOI: 10.1073/pnas.1705130114.

[81] L. Schertel, G. J. Aubry, C. M. Aegerter, and G. Maret. "Coherent multiple light scattering in Faraday active materials". *The European Physical Journal Special Topics* **226**, 1409 (2017). DOI: 10.1140/epjst/e2016-60239-5.

[82] E. Hecht. *Optics*. Addison-Wesley, (2002). URL: https://books.google.de/books?id=7aG6QgAACAAJ.

[83] R. Feynman, R. Leighton, and M. Sands. *The Feynman Lectures on Physics, Vol. I: The New Millennium Edition: Mainly Mechanics, Radiation, and Heat*. The Feynman Lectures on Physics. Basic Books, (2011). URL: https://books.google.de/books?id=bDF-uoUmttUC.

[84] W. Zinth and U. Zinth. *Optik: Lichtstrahlen - Wellen - Photonen*. Oldenbourg Wissenschaftsverlag, (2013). URL: https://books.google.de/books?id=FDb179jp31QC.

[85] C. F. Bohren and D. R. Huffman. *Absorption and Scattering of Light by Small Particles*. New York: Wiley, (1998). DOI: 10.1002/9783527618156.

[86] G. Mie. "Beiträge zur Optik trüber Medien, speziell kolloidaler Metallösungen". *Annalen der Physik* **330**, 377 (1908). DOI: 10.1002/andp.19083300302.

[87] J. Strutt. "On the scattering of light by small particles". *Philosophical Magazine* **41**, (1871).

[88] G. J. Aubry, L. Schertel, M. Chen, H. Weyer, C. M. Aegerter, S. Polarz, H. Cölfen, and G. Maret. "Resonant transport and near-field effects in photonic glasses". *Phys. Rev. A* **96**, 043871 (2017). DOI: 10.1103/PhysRevA.96.043871.

[89] J. K. Percus and G. J. Yevick. "Analysis of Classical Statistical Mechanics by Means of Collective Coordinates". *Phys. Rev.* **110**, 1 (1958). DOI: 10.1103/PhysRev.110.1.

[90] J. C. M. Garnett. "Colours in Metal Glasses and in Metallic Films". *Philosophical Transactions of the Royal Society of London A: Mathematical, Physical and Engineering Sciences* **203**, 385 (1904). DOI: 10.1098/rsta.1904.0024.

[91] M. P. van Albada, B. A. van Tiggelen, A. Lagendijk, and A. Tip. "Speed of propagation of classical waves in strongly scattering media". *Phys. Rev. Lett.* **66**, 3132 (1991). DOI: 10.1103/PhysRevLett.66.3132.

[92] C. M. Soukoulis, S. Datta, and E. N. Economou. "Propagation of classical waves in random media". *Phys. Rev. B* **49**, 3800 (1994). DOI: 10.1103/PhysRevB.49.3800.

[93] C. M. Soukoulis, E. N. Economou, G. S. Grest, and M. H. Cohen. "Existence of Anderson Localization of Classical Waves in a Random Two-Component Medium". *Phys. Rev. Lett.* **62**, 575 (1989). DOI: 10.1103/PhysRevLett.62.575.

[94] E. N. Economou and C. M. Soukoulis. "Calculation of optical transport and localization quantities". *Phys. Rev. B* **40**, 7977 (1989). DOI: 10.1103/PhysRevB.40.7977.

[95] K. Busch and C. M. Soukoulis. "Transport Properties of Random Media: A New Effective Medium Theory". *Phys. Rev. Lett.* **75**, 3442 (1995). DOI: 10.1103/PhysRevLett.75.3442.

[96] M. Chen, D. Fischli, L. Schertel, G. J. Aubry, B. Häusele, S. Polarz, G. Maret, and H. Cölfen. "Free-Standing Photonic Glasses Fabricated in a Centrifugal Field". *Small* **13**, 1701392 (2017). DOI: 10.1002/smll.201701392.

[97] P. D. García, R. Sapienza, Á. Blanco, and C. López. "Photonic Glass: A Novel Random Material for Light". *Advanced Materials* **19**, 2597 (2007). DOI: 10.1002/adma.200602426.

[98] P. D. García, R. Sapienza, and C. López. "Photonic Glasses: A Step Beyond White Paint". *Advanced Materials* **22**, 12 (2010). DOI: 10.1002/adma.200900827.

[99] S. Eiden-Assmann, J. Widoniak, and G. Maret. "Synthesis and Characterization of Porous and Nonporous Monodisperse Colloidal TiO2 Particles". *Chemistry of Materials* **16**, 6 (2004). DOI: 10.1021/cm0348949.

[100] S. Tanaka, D. Nogami, N. Tsuda, and Y. Miyake. "Synthesis of highly-monodisperse spherical titania particles with diameters in the submicron range". *Journal of Colloid and Interface Science* **334**, 188 (2009). DOI: 10.1016/j.jcis.2009.02.060.

[101] S. K. N. Sultanova and I. Nikolov. "Dispersion properties of optical polymers". *Acta Physica Polonica A* **116**, 585 (2009).

[102] I. Wimmer. "Particles from materials with high refractive index, their superstructures and optical properties". MA thesis. Universität Konstanz (2017).

[103] R. Lenke, R. Tweer, and G. Maret. "Coherent backscattering of turbid samples containing large Mie spheres". *Journal of Optics A: Pure and Applied Optics* **4**, 293 (2002). DOI: 10.1088/1464-4258/4/3/313.

[104] R. Lenke, U. Mack, and G. Maret. "Comparison of the 'glory' with coherent backscattering of light in turbid media". *Journal of Optics A: Pure and Applied Optics* **4**, 309 (2002). DOI: 10.1088/1464-4258/4/3/316.

[105] M. Reufer, L. F. Rojas-Ochoa, S. Eiden, J. J. Sáenz, and F. Scheffold. "Transport of light in amorphous photonic materials". *Applied Physics Letters* **91**, 171904 (2007). DOI: 10.1063/1.2800372.

[106] D. Montesdeoca, F. Bayat, A. Espinha, Á. Blanco, C. Pecharromán, and C. López. "Monodisperse Silica Spheres Ensembles with Tailored Optical Resonances in the Visible". *Particle & Particle Systems Characterization* **33**, 871 (2016). DOI: 10.1002/ppsc.201600194.

[107] S. Torquato. "Mean Nearest-Neighbor Distance in Random Packings of Hard *D*-Dimensional Spheres". *Phys. Rev. Lett.* **74**, 2156 (1995). DOI: 10.1103/PhysRevLett.74.2156.

[108] D. Mackowski and M. Mishchenko. "A multiple sphere T-matrix Fortran code for use on parallel computer clusters". *Journal of Quantitative Spectroscopy and Radiative Transfer* **112**, 2182 (2011). DOI: 10.1016/j.jqsrt.2011.02.019.

[109] V. Baranau and U. Tallarek. "Random-close packing limits for monodisperse and polydisperse hard spheres". *Soft Matter* **10**, 3826 (2014). DOI: 10.1039/C3SM52959B. Code available at https://doi.org/10.5281/zenodo.580324.

[110] J. R. Devore. "Refractive Indices of Rutile and Sphalerite". *J. Opt. Soc. Am.* **41**, 416 (1951). DOI: 10.1364/JOSA.41.000416.

[111] M. Reufer. "Amorphous photonic materials". MA thesis. University Freiburg (Switzerland) (2005).

[112] F. A. Erbacher, R. Lenke, and G. Maret. "Multiple Light Scattering in Magneto-optically Active Media". *EPL (Europhysics Letters)* **21**, 551 (1993). DOI: 10.1209/0295-5075/21/5/008.

[113] M. Faraday. "XLIX. Experimental researches in electricity. –Nineteenth series". *Philosophical Magazine Series 3* **28**, 294 (1846). DOI: 10.1080/14786444608645086.

[114] H. Becquerel. "The Faraday and Zeeman Effects". *Comptes Rendus* **125**, 679 (1897).

[115] P. R. Berman. "Optical Faraday rotation". *American Journal of Physics* **78**, 270 (2010). DOI: 10.1119/1.3266970.

[116] A. Sparenberg. "Photonic Magneto-Transport". PhD thesis. Konstanz: Universität Konstanz (2001).

[117] C. Leycuras, H. Le Gall, M. Guillot, and A. Marchand. "Magnetic susceptibility and Verdet constant in rare earth trifluorides". *Journal of Applied Physics* **55**, 2161 (1984). DOI: 10.1063/1.333596.

[118] A. Buckingham and P. Stephens. "Magnetic optical activity". *Annual Review of Physical Chemistry* **17**, 399 (1966). DOI: 10.1146/annurev.pc.17.100166.002151.

[119] R. Lenke, R. Lehner, and G. Maret. "Magnetic-field effects on coherent backscattering of light in case of Mie spheres". *EPL (Europhysics Letters)* **52**, 620 (2000). DOI: 10.1209/epl/i2000-00483-y.

[120] D. Lacoste. "Diffusion de la lumiere dans les milieux magneto-optiques et chiraux". PhD thesis. Grenoble: Université Joseph Fourier (1999), 211 p. URL: http://www.theses.fr/1999GRE10234.

[121] M. J. Weber. "Faraday Rotator Materials". *Lawrence Livermore National Laboratory Report* **M-103**, (1982).

[122] J. Dainty. *Laser speckle and related phenomena*. Topics in applied physics. Springer-Verlag, (1984). URL: http://books.google.de/books?id=--NRAAAAMAAJ.

[123] C. A. Müller and D. Delande. "Disorder and interference: localization phenomena". In: *Ultracold Gases and Quantum Information*, 441. Oxford University Press, (2011). DOI: 10.1093/acprof:oso/9780199603657.003.0009.

[124] T. Schwartz, S. Bartal G.and Fishman, and M. Segev. "Transport and Anderson localization in disordered two-dimensional photonic lattices". *Nature* **446**, 52 (2007). DOI: 10.1038/nature05623.

[125] I. Manai, J. Clément, R. Chicireanu, C. Hainaut, J. C. Garreau, P. Szriftgiser, and D. Delande. "Experimental Observation of Two-Dimensional Anderson Localization with the Atomic Kicked Rotor". *Phys. Rev. Lett.* **115**, 240603 (2015). DOI: 10.1103/PhysRevLett.115.240603.

[126] U. Kuhl, F. M. Izrailev, and A. A. Krokhin. "Enhancement of Localization in One-Dimensional Random Potentials with Long-Range Correlations". *Phys. Rev. Lett.* **100**, 126402 (2008). DOI: 10.1103/PhysRevLett.100.126402.

[127] S. Karbasi, T. Hawkins, J. B., K. W. Koch, and A. Mafi. "Transverse Anderson localization in a disordered glass optical fiber". *Opt. Mater. Express* **2**, 1496 (2012). DOI: 10.1364/OME.2.001496.

[128] M. V. Berry and S. Klein. "Transparent mirrors: rays, waves and localization". *European Journal of Physics* **18**, 222 (1997). DOI: 10.1088/0143-0807/18/3/017.

[129] J. Park, S. Zhang, and A. Z. Genack. "Intensity statistics and photon localization beyond one dimension". *Phys. Rev. E* **82**, 045101 (2010). DOI: 10.1103/PhysRevE.82.045101.

[130] A. Chabanov, M. Stoytchev, and A. Genack. "Statistical signatures of photon localization". *Nature* **404**, 850 (2000). DOI: 10.1038/35009055.

[131] A. Z. Genack and A. A. Chabanov. "Signatures of photon localization". *Journal of Physics A: Mathematical and General* **38**, 10465 (2005). DOI: 10.1088/0305-4470/38/49/002.

[132] Y. Bromberg, B. Redding, S. M. Popoff, and H. Cao. "Control of coherent backscattering by breaking optical reciprocity". *Phys. Rev. A* **93**, 023826 (2016). DOI: 10.1103/PhysRevA.93.023826.

[133] P. W. Anderson, D. J. Thouless, E. Abrahams, and D. S. Fisher. "New method for a scaling theory of localization". *Phys. Rev. B* **22**, 3519 (1980). DOI: 10.1103/PhysRevB.22.3519.

[134] V. Baluni and J. Willemsen. "Transmission of acoustic waves in a random layered medium". *Phys. Rev. A* **31**, 3358 (1985). DOI: 10.1103/PhysRevA.31.3358.

[135] M. Stoytchev and A. Z. Genack. "Measurement of the Probability Distribution of Total Transmission in Random Waveguides". *Phys. Rev. Lett.* **79**, 309 (1997). DOI: 10.1103/PhysRevLett.79.309.

[136] M. Stoytchev and A. Z. Genack. "Observations of non-Rayleigh statistics in the approach to photon localization". *Opt. Lett.* **24**, 262 (1999). DOI: 10.1364/OL.24.000262.

[137] O. Irtenkauf. *Einfluss der Reziprozität auf die eindimensionale Anderson Lokalisierung von Licht*. Bachelor's Thesis. (2017).

[138] S. Zhang, J. Park, V. Milner, and A. Z. Genack. "Photon Delocalization Transition in Dimensional Crossover in Layered Media". *Phys. Rev. Lett.* **101**, 183901 (2008). DOI: 10.1103/PhysRevLett.101.183901.